Research and development of CuInSe[2]-based photovoltaic solar cells.

DELSOL, Thomas.

Fines are charged at 50| oer hour

nf:- I

REFERENCE

Research and Development of $CuInSe_2$-based Photovoltaic Solar Cells

Thomas DELSOL

A thesis in partial fulfilment of the requirements of Sheffield Hallam University for the degree of Doctor in Philosophy

September 2001

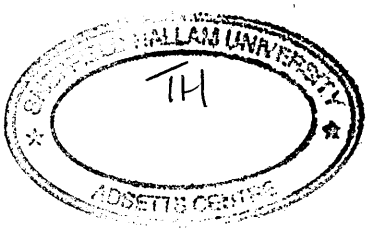
SHEFFIELD HALLAM UNIVERSITY
TH
ADSETTS CENTRE

Acknowledgements

I would like to thank Dr. Dharmadasa, my director of studies, for his continuous guidance and encouragements throughout the course of the project and also for reading the draft version of this text. My thanks also go to Prof. Young, my second supervisor, for his fast reading of the present thesis. This thesis would not have been completed in time without his help.

I would like to extend my gratitude towards all the technical and academic staff members of the School of Science and the Materials Research Institute of Sheffield Hallam University who contributed to this work. They know who they are.

I would like to acknowledge the following persons for their direct contribution to this work: Nandu Chaure, Robert Burton, Mike Simmonds, Katsumi Kushiya and the research group at Warsaw University of Technology.

Special thanks to kind-hearted Anura for his invaluable support and interesting discussions during the tenure of my research. I wish also to thank Tiang Fan for useful discussions concerning the project bringing light to where there was sometimes darkness. Thanks also to Nandu for his nice AFM pictures.

The friends I met in Sheffield are greatly acknowledged for all the good times I enjoyed during the course of my stay in Sheffield. These, in particular, being Sonia, Eppie, Thierry, Ann, Pierre, Theresa, Jane, Charlotte, Maria, Nicolas, Caroline,...

I wish to thank all my family and my friends in France for making so enjoyable my student life. I owe a lot to my parents for supporting me financially and motivating me throughout my studies. Finally, I wish to thank Marie Laure, her support has kept me going to the end. She has never faltered in her persuasion and encouragements and for that I can never thank her enough.

I wish all the best to the new generation...

Abstract

The work reported in this thesis includes the growth and characterisation of $CuInSe_2$-based materials as well as the assessment and development of $CuInSe_2$-based solar cells by the technique of electrodeposition.
$Cu(InGa)(SeS)_2$ layers grown on glass/molybdenum by the two-stage method at Showa Shell have been used for comparison.
Electrodeposition of window materials (ZnSe and CdS) on glass/TCO substrates following the conditions prior-established at Sheffield Hallam University has been achieved.
$CuInSe_2$ films have been successfully grown on glass/TCO by electrodeposition. The semi-conducting layers were characterised to investigate their crystallinity, morphology, composition, optical and electrical properties. The structure of the films was characterised by XRD and Raman spectroscopy. The morphology was studied by SEM and AFM. The elemental bulk analysis was performed using XRF and ICPMS. The elemental surface analysis was performed using XPS and the depth profile analysis was studied by GDOES. The optical properties were characterised by optical absorption and the conductivity type was determined by PEC measurements. The conditions of electrodeposition and post deposition treatments were found to influence strongly the properties of the electrodeposited films. Near-stoichiometric films grown by electrodeposition are polycrystalline with a (112) preferential orientation of the chalcopyrite structure. CIS films appear dense with a good mechanical adhesion to the conducting oxide substrates and show crack-free surfaces with spherical grains electrically well connected to each other with a size up to 1 μm. Cu, In and Se atoms are not uniformly distributed within the CIS films and In-rich phases, such as $CuIn_3Se_5$, cover the surface of the films. Testing of electrical conductivity shows that the films are generally p-type.
I-V and C-V measurements were used to characterise the solar cells based on electrodeposited $CuInSe_2$. Early stage $CuInSe_2$-based solar cells showed encouraging results with efficiencies up to 15.9 % for the best devices. The maximum values of the V_{OC}, J_{SC} and FF observed for the glass/FTO/ZnSe/$CuInSe_2$/Au devices were 0.3 V, 105.0 mA/cm^2, and 50 %, respectively.

Table of contents

Chapter 1: Introduction

1.1 Context

With nuclear power discredited on environmental grounds as a long-term solution to the world's energy requirements, the direct use of sunlight energy offers a conceivable alternative. Photovoltaic semiconductor solar cells are able to convert solar radiation directly into electricity with high conversion efficiency. When a semiconductor is exposed to light, photons with energy, hv, greater than the semiconductor band gap energy, E_g, create electron-hole pairs and, in a suitable semiconductor device, internal electric fields exist and allow the separation of these photogenerated carriers and the production of an electric current.

Silicon based photovoltaic (PV) solar cells are available for terrestrial solar energy conversion but their high production cost limits the possible applications at present. Research efforts are not only concentrated on the improvement of silicon based solar cells but also on the development of new photovoltaic materials and devices. However, no photovoltaic semiconductor has a band gap, which matches the entire spectral distribution of sunlight and the strategy to overcome this problem is to use materials with different band gap energies, selected to better cover the full wavelength range of the solar spectrum. This concept is realised in heterojunction devices, which are formed between wide band gap semiconductors, also called window materials, and lower band gap semiconductors, called absorber materials. II-VI binary compounds and three component materials of the type I-III-VI_2, which have high absorption coefficient and good photovoltaic properties, are of special interest. Thus, CdS and ZnSe, which have wide band gaps (2.42 eV and 2.67 eV, respectively [1]), are currently used as window materials in heterojunction solar cells and copper indium diselenide ($CuInSe_2$ or CIS) is an attractive candidate in the fabrication of thin film solar cells due to its unique

properties as an optical absorber material. $CuInSe_2$ has a direct energy band gap of 1.04 eV [2] and the highest optical absorption coefficient (103 cm^{-1}) at band gap energy for known semiconducting materials [3]. The band gap of $CuInSe_2$ can be engineered to obtain the optimum band gap of 1.5 eV [4] by addition of gallium into the material. Its structure can be maintained over a wide range of composition by the incorporation of intrinsic defects in the crystal lattice. These defects are responsible for polycrystalline $CuInSe_2$ having electronic properties comparable to those of single crystals and allow the material to be manufactured as either p- or n-type by changing the stoichiometry [5]. The material has also a good lattice and electron affinity match with (ZnSe, CdS) window materials [6] and the radiation resistance and stability of $CuInSe_2$-based solar cells are reported to be superior to crystalline Si and GaAs solar cells [7].

For these reasons, $CuInSe_2$ has been the focus of increased research efforts, especially since the beginning of the nineteen nineties (see Figure 1.1).

Years

Figure 1.1: Increased number of publications related to $CuInSe_2$ during the last 20 years.

Copper indium gallium diselenide (CIGS)-based solar cells are now achieving conversion efficiencies of 18.8% [8] on the laboratory scale, indicating the value of continuing development to improve knowledge of the materials and processing steps.

Thin films of $CuInSe_2$ have been produced using a wide variety of deposition techniques including thermal evaporation [9, 10, 11], molecular beam epitaxy (MBE) [12], chemical

vapour deposition (CVD) [13, 14, 15], sputtering [16, 17, 18, 19], pulsed laser deposition (PLD) [20], flash evaporation [21], spray pyrolysis [22], ionised cluster beam deposition [23], chemical bath deposition [24], thermal processing of stacked precursor layers [25, 26, 27, 28] and electrodeposition [29, 30, 31]. Among the various methods for depositing $CuInSe_2$, electrochemical deposition from aqueous solutions is of particular interest because it is economical, technologically simple and it allows the possibility of deposition over large surface areas. However, the reported efficiency of thin film PV devices using one-step electrodeposition remains low compared to those obtained from physical vapour deposition (PVD). To date, the highest efficiency is 5.2% [32] but is has reached 7.9% after a selenisation step [33]. A $CuIn_xGa_{1-x}Se_2$-based solar cell fabricated using electrodeposited precursors subjected to post deposition treatments has achieved 14.1% efficiency [34].

1.2 Aims and objectives

The work reported in this thesis includes the growth and characterisation of $CuInSe_2$-based materials as well as the assessment and development of $CuInSe_2$-based solar cells by the technique of electrodeposition.

The project included the following main areas of work.

- Electrodeposition of window materials (ZnSe and CdS) on glass/FTO (fluorine tin oxide) or glass/ITO (indium tin oxide) substrates following the conditions prior-established at Sheffield Hallam University [35, 36, 37, 38] and characterisation to investigate their structural, morphological, optical and electrical properties. The structure of the layers was characterised by x-ray diffraction (XRD) and Raman spectroscopy. The morphology was studied by atomic force microscopy (AFM). The optical properties were studied by optical absorption spectroscopy. Finally, the conductivity type was determined by photoelectrochemical (PEC) measurements.
- Electrodeposition of the absorber material $CuInSe_2$ on glass/FTO and glass/ITO substrates and characterisation to investigate and improve its crystallinity, morphology, composition, optical and electrical properties. The

structure of the layers was characterised by XRD and Raman spectroscopy. The morphology was studied by scanning electron microscopy (SEM) and AFM. The elemental analysis was performed using x-ray fluorescence (XRF), inductively coupled plasma mass spectroscopy (ICPMS), x-ray photoelectron spectroscopy (XPS) and glow discharge optical emission spectroscopy (GDOES). The optical properties were studied by optical absorption and the conductivity type was determined by PEC measurements. $Cu(InGa)(SeS)_2$ layers grown on glass/molybdenum by the two-stage method at Showa Shell have been used for comparison.

- Fabrication and assessment of $CuInSe_2$-based solar cells using current-voltage (I-V) and capacitance-voltage (C-V) measurements. Some of the structures studied were:

    - glass/ITO/ $CuInSe_2$/Au
    - glass/ ITO / $CuInSe_2$/In
    - glass/FTO/ZnSe/$CuInSe_2$/Au
    - glass/ITO/CdS/$CuInSe_2$/Au

1.3 Format of the thesis

This thesis is divided into eight chapters. The first three, including this introduction, concern the theory and provide a review of the work to date on $CuInSe_2$-based solar cells. The experimental details and results are presented in Chapters 4 to 7 and conclusions are drawn in Chapter 8.

- Chapter 2 is a summary of the background needed to understand the development of $CuInSe_2$. It provides the theory of semiconductor junctions and the principles of photovoltaic thin film solar cells. It also describes the properties of the studied materials and explains why they were chosen for this work. A brief review of the techniques used by other groups to grow $CuInSe_2$ and of the processes involved in the development of solar cells is given and the advances to date in the field of CIS-based solar cells are presented.

- Chapter 3 provides a description of the twelve techniques used to characterise the materials and the devices. It represents only a small cross-section of the vast literature describing these techniques. Only the basis of each technique and the subjects pertinent to this work are included here. For more details, the reader should consult the standard textbooks mentioned at the end of the chapter.
- In Chapter 4, the properties of the substrates used to grow the semiconductor films are explored as well as the growth of the window materials. This work is only briefly presented, as it has already been published [35, 37]. However, it was important to include it here because these properties are crucial to understand the device characteristics. In addition, the characterisation of the electrodeposited window material layers showed that there might be some differences with previous results.
- In Chapter 5, the results of the characterisation of $Cu(InGa)(SeS)_2$ layers grown on glass/molybdenum by the two-stage method at Showa Shell, which were used for comparison with the electrodeposited materials, are presented and discussed.
- Chapter 6 focuses on the growth of $CuInSe_2$ and gives a full set of results concerning the characterisation of the electrodeposited thin films. These results are also discussed.
- In Chapter 7, attention is given to the etching procedure of CIS layers, assessment of metal-semiconductor junctions as well as heterojunctions based on electrodeposited $CuInSe_2$ layers.
- Chapter 8 summarises the important conclusions of the work and suggests programmes for future research in this area.

1.4 References

[1] Chu T. L., Chu S. S., Solid State Electronics, 38 (3) (1995) 533.

[2] Moller H. J., Progress in Materials Science, 35 (1991) 205.

[3] Ikari T., Yoshino K., Shimizu T., Fukuyama A., Maeda K., Fons P. J., Yamada A., Niki S., Proceedings of 11th International Conference on Ternary and Multinary Compounds, Institute of Physics Conference Series, 152 (1998) 511.

[4] Loferski J. J., Journal of Applied Physics, 27 (7) (1956) 777.

[5] Wei S. H., Zhang S. B., Zunger A., Proceedings of 11th International Conference on Ternary and Multinary Compounds, Institute of Physics Conference Series, 152 (1998) 765.

[6] Scheer R., Vacuum Science and Technology, 2 (1997) 77.

[7] Rudmann D., Haug F. J., Krejci M., Zogg H., Tiwari A. N., Proceedings of 16th European Photovoltaic Solar Energy Conference and Exhibition, Glasgow, United Kingdom (2000) 298.

[8] Contreras M. A., Egaas B., Ramanathan K., Hiltner J., Swartzlander A., Hasoon F., Noufi R., Progress in Photovoltaics, 7 (1999) 311.

[9] Negami T., Nishitani M., Ikeda M., Wada T., Solar Energy Materials and Solar Cells, 35 (1994) 215.

[10] Kwon S. H., Ahn B. T., Kim S. K., Yoon K. H., Song J., Thin Solid Films, 323 (1998) 265.

[11] Hachiuma Y., Ashida A., Yamamoto N., Ito T., Cho Y., Solar Energy Materials and Solar Cells, 35 (1994) 247.

[12] Grindle S. P., Clark A. H., Rezaie-Serej S., Falconer E., McNeily J., Kazmerki L. L., Journal of Applied Physics, 51 (10) (1980) 5464.

[13] Zouaoui A., Lachab M., Hidalgo M. L., Chaffa A., Llinares C., Kesri N., Thin Solid Films, 339 (1-2) (1999) 10.

[14] Artaud M. C., Ouchen F., Martin L., Duchemin S., Thin Solid Films, 324 (1-2) (1998) 115.

[15] Jones P. A., Jackson A. D., Lickiss P. D., Pilkington R. D., Tomlinson R. D., Thin Solid Films, 238 (1) (1994) 4.

[16] Nakada T., Migita K., Niki S., Kunioka A., Japanese Journal of Applied Physics, 34 (Part 1) (No. 9A) (1995) 4715.

[17] Tanaka T., Tanahashi N., Yamaguchi T., Yoshida A., Solar Energy Materials and Solar Cells, 50 (1998) 13.

[18] Chung-Yang L., Xia H. Z., Rockett A., Shafarman W. N., Birkmire R. W., Solar Energy Materials and Solar Cells, 36 (1995) 445.

[19] Tseng B. H., Rockett A., Lommasson T. C., Yang L. C., Wert C. A., Thornton J. A., Journal of Applied Physics, 67 (5) (1990) 2637.

[20] Schäffler R., Klose M., Brieger M., Dittrich H., Schock H. W., Materials Science Forum, 173-174 (1995) 135.

[21] Sakata H., Ogawa H., Solar Energy Materials and Solar Cells, 63 (2000) 259.

[22] Ramaiah K. S., Raja V. S., Bhatnagar A. K., Juang F. S., Chang S. J., Su Y. K., Materials Letters, 45 (2000) 251.

[23] Kondo K., Sano H., Sato K., Thin Solid Films, 326 (1998) 83.

[24] Vidyadharan Pillai P. K., Vijayakumar K. P., Solar Energy Materials and Solar Cells, 51 (1998) 47.

[25] Firoz Hasan S. M., Subhan M. A., Mannan K. M., Optical Materials, 14 (2000) 329.

[26] Ka O., Alves H., Dirnstorfer I., Christmann T., Meyer B. K., Thin Solid Films, 361-362 (2000) 263.

[27] Nakada T., Onishi R., Kunioka A., Solar Energy Materials and Solar Cells, 35 (1994) 209.

[28] Terauchi M., Negami T., Nishitani M., Ikeda M., Wada H., Wada T., Solar Energy Materials and Solar Cells, 35 (1994) 121.

[29] Bhattacharya R.N., Journal of Electrochemical Society, 130 (10) (1983) 2040.

[30] Sudo Y., Endo S., Irie T., Japanese Journal of Applied Physics, 32 (Part 1) (No. 4) (1993) 1562.

[31] De Silva K. T. L., Priyantha W. A. A., Jayanetti J. K. D. S., Chithrani B. D., Siripala W., Blake K., Dharmadasa I. M., Thin Solid Films, 382 (2001) 158.

[32] Savadogo O., Solar Energy Materials and Solar Cells, 52 (1998) 361.

[33] Fernandez A. M., Sebastian P. J., Bhattacharya R. N., Noufi R., Contreras M., Hermann A. M., Semiconductor Science and Technology, 11 (1996) 964.

[34] Bhattacharya R. N., Batchelor W., Wiesner H., Hasoon F., Granata J. E., Ramanathan K., Alleman J., Keane J., Mason A., Matson R. J., Noufi R. N., Journal of Electrochemical Society, 145 (10) (1998) 3435.

[35] Samantilleke A. P., Boyle M. H., Young J., Dharmadasa I. M., Journal of Materials Science: Materials in Electronics, 9 (1998) 231

[36] Samantilleke A. P., PhD Thesis, Sheffield Hallam University (1998)

[37] Mc Gregor S. M., Dharmadasa I. M., Wadswoorth I., Care C. M., Optical Materials, 6 (1996) 75

[38] Mc Gregor S. M., PhD Thesis, Sheffield Hallam University (1999)

Chapter 2: $CuInSe_2$-based solar cells: Theory and current development

2.1 Introduction

At present, the photovoltaic device field in general is so dynamic and so fast-changing that today's concepts may be obsolete tomorrow. It is therefore important to understand the fundamental physical processes and to keep learning from other workers if one wants to adapt to these ceaseless changes. The material presented in this chapter is intended to serve as a foundation. It provides the theory of semiconductor junctions and the principles of photovoltaic thin film solar cells. It also describes the properties of the studied materials and explains why they were chosen for this work. It reviews the fabrication processes of $CuInSe_2$ solar cells, such as the material growth, and the post deposition steps (heat treatment, etching and metal contact formation), which are crucial for achieving devices with high conversion efficiency. It finally summarises the advances in the field of CIS-based solar cells. Much of the information is condensed and presented in tables and figures. The references listed at the end of this chapter can provide more information.

2.2 Physical principles of photovoltaic energy conversion

The properties of junctions are the basis of practically all semiconductor devices, including optoelectronic ones. The most common junction, and hence the one introduced first, is the p-n junction, which is formed from n- and p-type materials of the same semiconductor. Theoretically, one can expect an improvement in the efficiency of a solar cell device if it consists of materials with different band gap energies, which match different parts of the solar spectrum. This concept realised in a heterojunction device will be discussed next. Another important system is the metal-semiconductor junction, which is involved in all electronic device structures and is extremely important for

material characterisation, such as DLTS. Once the basic physics and structures are described, the operational solar cell structure and its principle will be detailed. Full coverage of the theoretical background and derivation of the equations can be found elsewhere [1,2, 3,4].

2.2.1 The p-n junction

When a p-semiconductor and an n-semiconductor are placed in intimate contact, holes diffuse from the p to n regions and electrons from n to p. As a result of this transfer of carriers, positively charged donor ions are left behind on the n side of the junction and negatively charged acceptor ions accumulate on the p side. The existence of positive charges on one side and negative charges on the other side causes an electric field. This field forces electrons to drift from p to n and holes from n to p so that a balance is established at which each of the hole and electron currents is zero. Because a voltage difference, V_{bi}, is formed between the p and n regions known as the built-in voltage, an energy difference, qV_{bi}, exists between them. Thus, an energy barrier is established across the depletion region. Consequently, the energy bands are bent and the Fermi levels of the two regions are aligned, as in Figure 2.1.

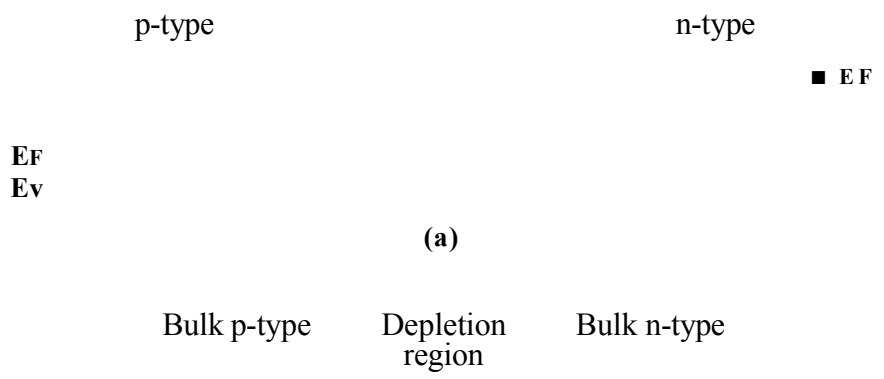

Figure 2.1: Band diagrams of a p-n junction in equilibrium (a) before contact and (b) after contact.

The built-in potential V_{bi} is given by

$$V_{bi} = \frac{E_g}{q} - (V_n + V_p) = \frac{kT}{q} \ln\left(\frac{N_A N_D}{n_i^2}\right) \tag{2.1}$$

where k is the Boltzmann constant, T the temperature, q the magnitude of electronic charge, N_A the acceptor concentration in the p-side, N_D the donor concentration in the n-side and n_i the intrinsic charge carrier density.

The width of the depletion layer w is given by

$$w = \left(\frac{2\varepsilon}{q}\frac{(N_A + N_D)}{N_A N_D} V_{bi}\right)^{\frac{1}{2}} \tag{2.2}$$

where ε is the semiconductor permittivity and other symbols have their usual meanings.

2.2.2 The heterojunction

Photons with energies greater than the band gap energy generate electrons in the conduction band, which transform part of their energy into heat until they occupy energy states at the conduction band edge, which tends to decrease the performance of the device. In addition, photons with energy lower than the band gap energy of the semiconductor do not contribute to the photocurrent. In order to overcome these problems, one can form a junction between materials with different band gap energies, which are optimised for different wavelength ranges of the spectrum. The material with the larger band gap energy is on the top. Light with energy less than its band gap but greater than the one of the second semiconductor passes through the first semiconductor, which acts as a window, and is absorbed by the second semiconductor. Two types of heterojunctions exist and their band diagrams differ from the one of a classical p-n homojunction.

2.2.2.1 The anisotype heterojunction

The band diagrams for N-p and P-n heterojunctions are displayed in Figure 2.2. The main dissimilarity between p-n heterojunctions and homojunctions is the difference in

energy of the conduction band edges ΔE_C and the valence band edges ΔE_V in the two semiconductors.

$$\Delta E_C = \chi_2 - \chi_1 \tag{2.3}$$

and

$$\Delta E_V = E_{g1} - E_{g2} + \chi_1 - \chi_2 \tag{2.4}$$

where χ_1, χ_2 are the electron affinities of the two semiconductors and E_{g1}, E_{g2} are their respective band gaps [5].

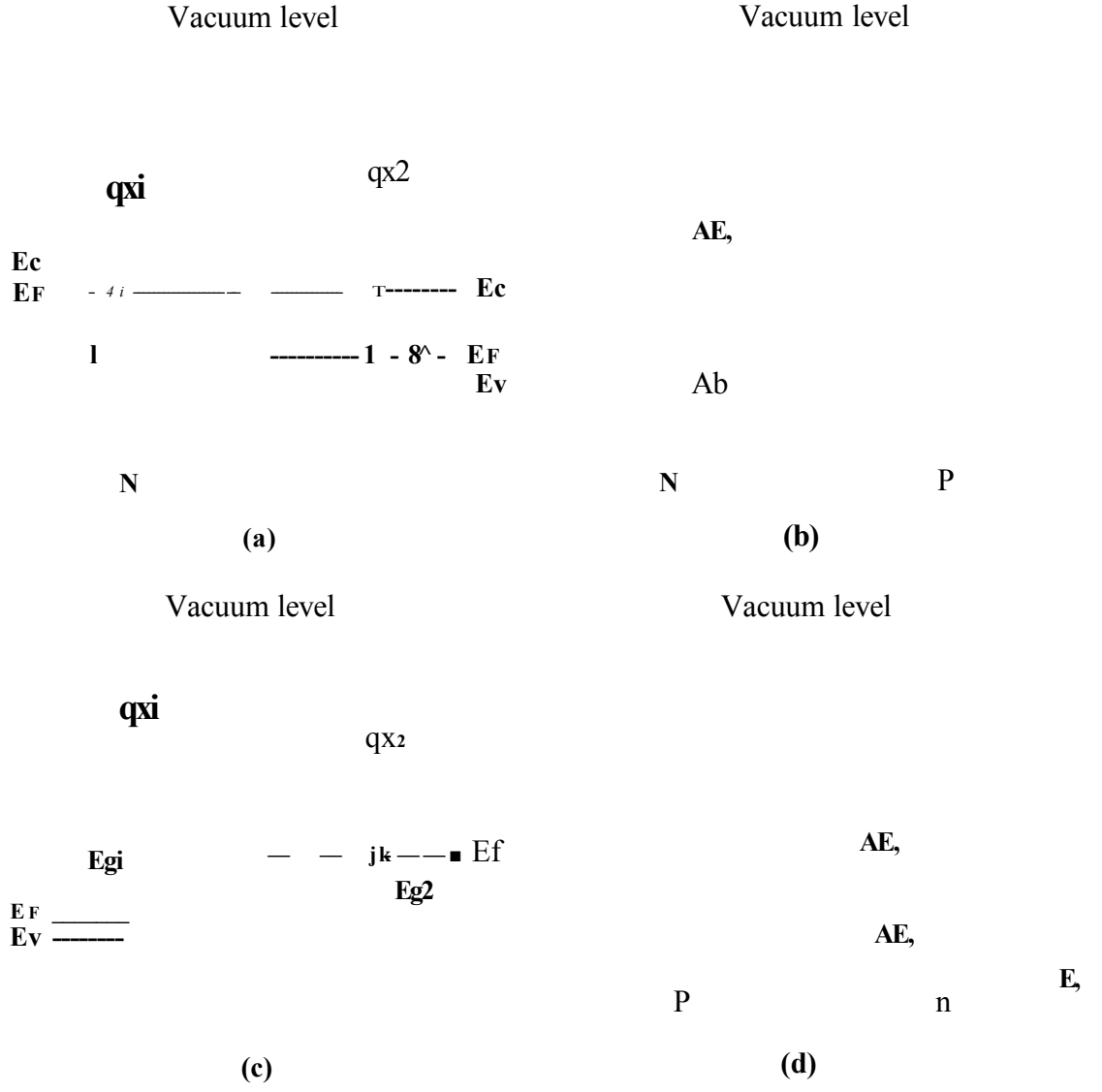

Figure 2.2: Band diagrams of anisotype heterojunctions: N-p (a) before contact and (b) after contact; P-n (c) before contact and (d) after contact.

In N-p heterojunctions, the negative ΔE_C produces a spike in the conduction band whereas the negative ΔE_V for a P-on-n heterojunction gives rise to a spike in the valence band. These spikes are undesirable for photovoltaic applications, as they impede the flow of minority carriers across the junction from the p-type to the n-type region and therefore reduce the photocurrent. Such spikes can however be avoided by a suitable combination of electron affinities and doping levels.

2.2.22 The isotype heterojunction

In contrast to a homojunction, a heterojunction can have the same type of conductivity in both semiconductors. It is called an N-n or P-p isotype heterojunction where the capital letter signifies the material of larger band gap. The band structures for N-n and P-p contacts are shown in figure 2.3.

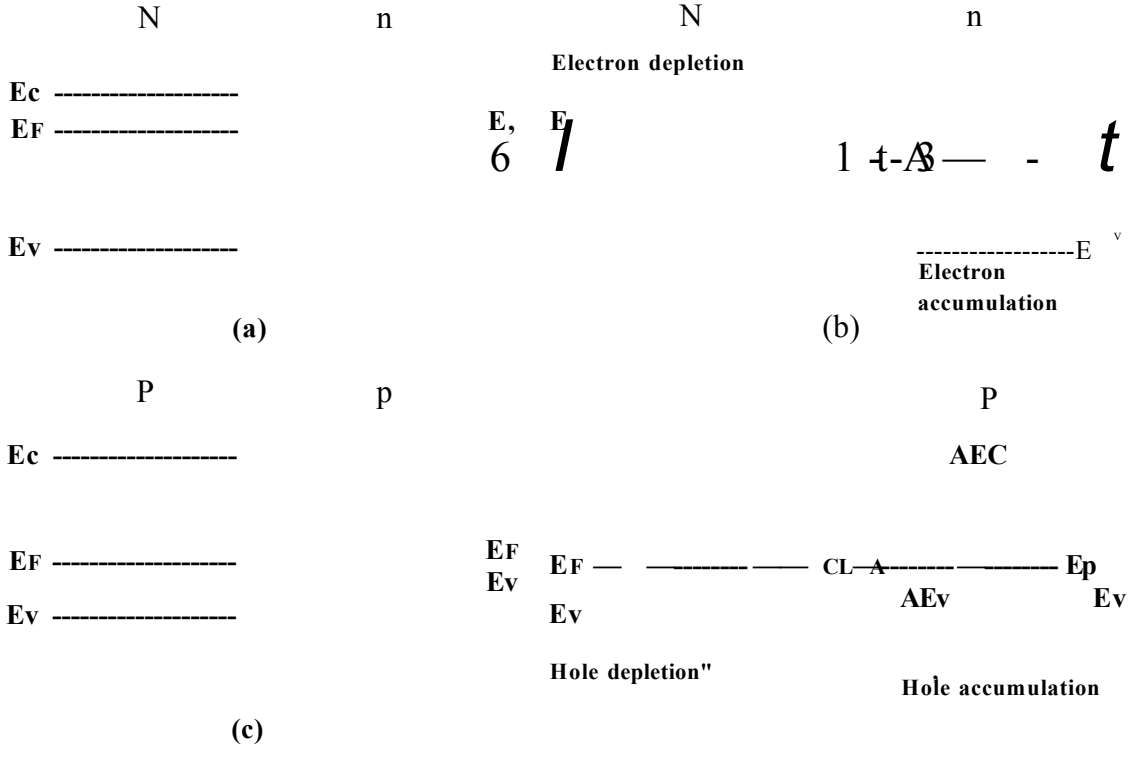

Figure 2.3: Band diagrams of isotype heterojunctions: N-n (a) before contact and (b) after contact; P-p (c) before contact and (d) after contact.

In the case of a N-n heterojunction, the electrons flow from a high potential region to a low potential region until the fermi levels have equalised, in our case from N to n. This leads to the depletion of electrons on the N-side and accumulation on the n-side, giving the corresponding band bending, as shown in Figure 2.3 (b). In the case of a P-p

heterojunction, the hole transfer from P to p causes a hole potential barrier at the interface, and hence corresponding depletion and accumulation layers.

2.2.3 The metal-semiconductor junction

Metal-semiconductor contacts show either rectifying or ohmic behaviour. Rectifying contacts permit current in one direction only, whereas ohmic contacts allow easy current flow in both directions from metal to semiconductor and from semiconductor to metal. Whether a contact is rectifying or ohmic depends on the Fermi levels in both the metal and the semiconductor.

2.2.3.1 The rectifying contact

Similarly to the p-n system, the Fermi levels equalise at a metal-semiconductor junction, and all other bands bend accordingly. The only levels of significance in this procedure are the energy levels of the conduction band E_c and the valence band E_v, which must bend upwards at the junction (Figure 2.4 (b)) for n-type semiconductors, if $\phi_m > \phi_n$. To achieve this, electrons must be transferred from the semiconductor to the metal, creating a depletion region in the near surface of the semiconductor and excess negative charge on the metal side resulting in an electric field distribution. The effect is similar to that of a p^+-n junction and the depletion region width w can be calculated in the same way from (2.2) assuming that $N_A >> N_D$. The difference between the work functions of the metal and the semiconductor gives the contact potential or built-in potential

$$V_{bi} = \phi_m - \phi_n \tag{2.5}$$

The electron barrier height ϕ_{bn} is given by

$$\phi_{bn} = \phi_m - \chi \tag{2.6}$$

For a p-type semiconductor with $\phi_m < \phi_p$, a positive and a negative charge on the metal and semiconductor sides respectively are required to equalise the Fermi levels. Similarly to (2.6), the hole barrier height is given by

$$K = Eg - Wm-x) \quad (2.7)$$

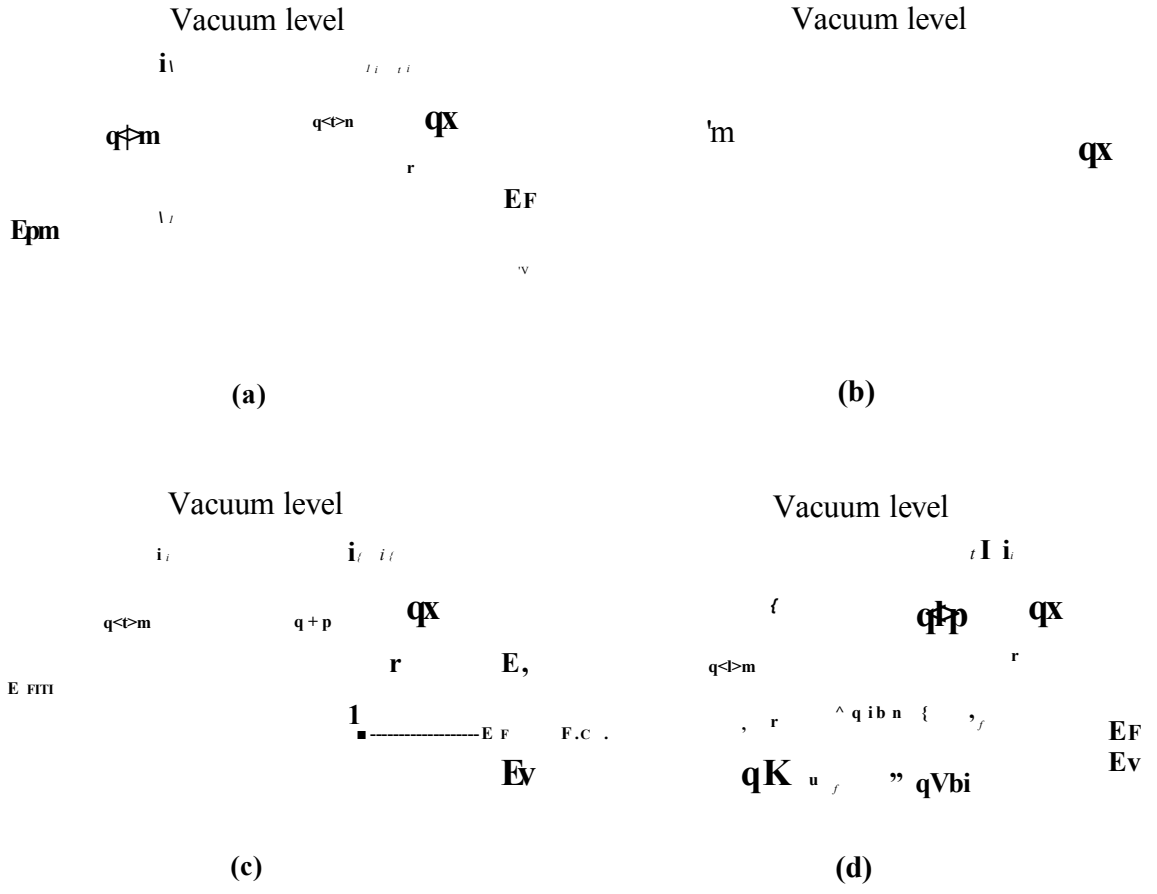

Figure 2.4: Band diagrams of rectifying contacts: metal and n-type semiconductor junction with $\phi_m > \phi_n$ (a) before contact and (b) after contact; metal and p-type semiconductor junction with $\phi_m < \phi_p$ (c) before contact and (d) after contact.

The above explanations given by the Schottky model [6] are not always valid, as they do not take into account the surface and interface states. At the surface, atoms have neighbours on one side only so that some of their electrons are left unpaired (dangling bonds). These dangling bonds act either as donors or acceptors and are therefore responsible for surface states. These states can lead to a positive or a negative charge at the surface, which generates a barrier. If the density of surface states is very large, the Fermi level of the semiconductor is then independent of the metal and is said to be pinned. In this model proposed by Bardeen [7], the resultant barrier height is thus independent of the metal work function but determined by the property of the semiconductor. The in-diffusion of metal atoms and out-diffusion of semiconductor elements can also generate interface states. Another source of interface states can come

from the wave functions of electrons in the metal with energies corresponding to the forbidden gap, which penetrate into the semiconductor in the form of evanescent waves. These are called metal induced gap states (MIGS). The deposition of metal on the semiconductor can also cause structural damage to the surface leading to the formation of interface states. Another phenomenon altering the barrier height between a metal and a semiconductor is known as the image force. When electrons approach the metal surface, they experience an attractive force, as if a positive charge of magnitude q was located at the mirror image of the electrons with respect to the interface. This effect confers to the electrons a negative potential energy, which has to be added to the potential of the Schottky barrier leading to its lowering.

2.2.3.2 The ohmic contact

This form of metal-semiconductor junction is far more common in optoelectronic devices than the rectifying Schottky contact. Ohmic contacts to both p-type and n-type materials are needed to connect the external circuitry to the device. Unlike the Schottky contact, which shows rectifying behaviour, the ohmic contact needs to have a linear I-V characteristic for both biasing directions and the contact resistance at the junction needs to be as small as possible. The material conditions for ohmic contact are $\phi_m < \phi_n$ for n-type and $\phi_m > \phi_p$ for p-type semiconductors. The band diagrams associated with ohmic contacts are shown in Figure 2.5. For the n-type case, the Fermi levels are equalised by transferring electrons from the metal to the semiconductor. There is thus no depletion at the junction, and because of the charge transfer the conduction band minimum is lowered. There is then only a small barrier to further electron flow from metal to semiconductor, easily overcome by thermal excitation or by an external bias. A similar situation occurs for the contact to the p-type material, where holes readily flow from the metal to the semiconductor.

If the semiconductor has surface states responsible for the pinning of the Fermi level and the formation of a barrier, ohmic contacts can be formed by introducing a heavily doped region close to the surface, which makes a narrow barrier width. There is then a finite probability that electrons can tunnel across the narrow barrier and into the main part of the metal or semiconductor.

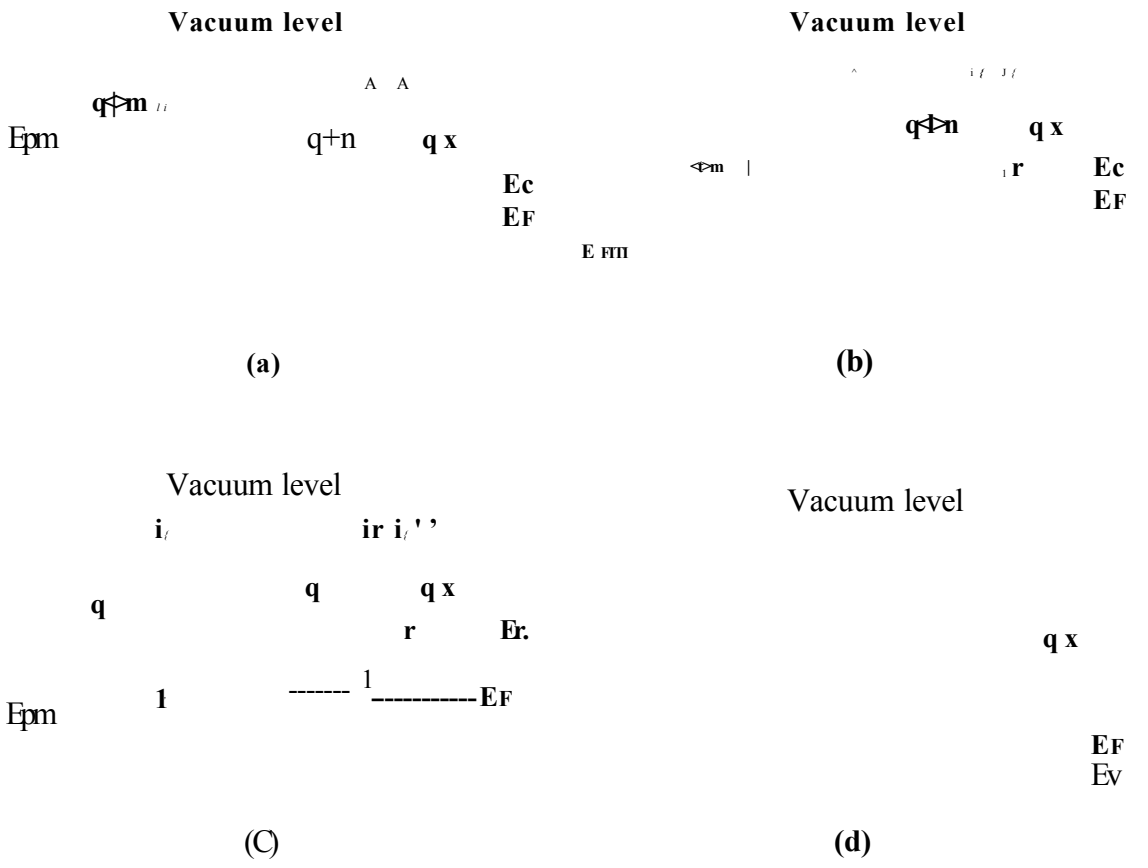

Figure 2.5: The formation of metal-semiconductor ohmic contacts. Metal and n-type semiconductor junction in equilibrium (a) before contact and (b) after contact, (c) Metal and p-type semiconductor in equilibrium (a) before contact and (d) after contact.

2.2.4 Theory of thin film solar cells

When a semiconductor is exposed to light, photons with energy $hv > Eg$ create electron-hole pairs. The internal electric field produced by one of the junctions described before separates these photogenerated carriers to produce an electric signal. As already discussed, heterojunctions have several advantages over conventional p-n homojunction solar cells and are therefore preferentially used. Figure 2.6 shows an idealised band structure for an N-p heterojunction solar cell without energy spikes. Here, the charge carriers generated in the depletion layer or within one diffusion length from the edge of the depletion region drift under the influence of the electric field with electrons going into the N region and holes going into the p region, both contributing to the photogenerated current. The current-voltage (I-V) characteristics as well as the efficiency requirements for the solar cells are discussed in Chapter 3, in the section describing the I-V measurements.

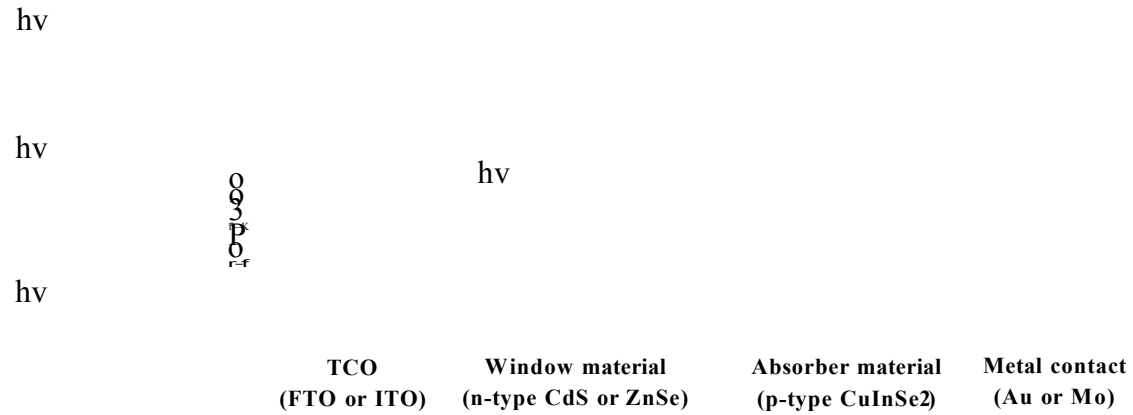

Figure 2.6: Energy band diagram of an N-p heterojunction under illumination.

2.3 Properties of the solar cell materials

Several groups of binary or ternary semiconductors have attracted interest because of their diverse optical, electrical and structural properties. These compounds offer a broad range of optical band gaps and charge carrier mobilities as well as the ability to accommodate different dopants. This explains their emergence as technologically significant device materials, including applications in photovoltaic solar cells and light emitting diodes. Semiconductors can be divided into two groups in heterojunction solar cell technology: the window material, which absorbs photons of higher energy and the absorber material, which absorbs photons of lower energy. The window materials used in this project are zinc selenide (ZnSe) and cadmium sulfide (CdS). The absorber material is copper indium diselenide ($CuInSe_2$ or CIS) and its alloys with gallium. In this section, the properties of these materials are summarised and discussed. The properties of the window materials will be described very shortly, as they have already been examined in previous work [8, 9]. $CuInSe_2$ properties will be given more attention, as this material is the main subject of this work.

2.3.1 Properties of ZnSe and CdS

ZnSe and CdS are wide band gap materials with energy band gaps of 2.67 eV and 2.42 eV, respectively, and have large optical absorption coefficients at wavelengths above band gap wavelengths [10]. Therefore, they are well suited for acting as window materials in solar cell devices. ZnSe crystallises in the sphalerite (or zinc blende) structure (Figure 2.7 (a)) whereas CdS crystallises in the wurtzite structure (Figure 2.7 (b)) [10, 11]. The interesting properties of CdS and ZnSe are reported in Table 2.1.

Property	Unit	CdS	ZnSe
Stable structure		wurtzite [10]	Sphalerite [10]
Space group [12]		$P6_3mc - C_{6v}^4$	$F\bar{4}3m - T_d^2$
Molecular weight	$g.mol^{-1}$	144.46 [12]	144.34 [12]
Density	$g.cm^{-3}$	4.82 [12]	5.42 [12]
Melting point	K	1748 [12]	1790 [12]
Lattice parameters (300K): a c	Å	4.1348 [12] 6.7490 [12]	5.6676 [12]
Thermal expansion coefficient (300K)	$x10^{-6} K^{-1}$	4.7 [12]	7.2 [12]
Thermal conductivity (300K)	$mW.cm^{-1}.K^{-1}$	401 [12]	140 [12]
Specific heat capacity	$J.kg^{-1} K^{-1}$	330 [12]	339 [12]
Debye temperature	K	219 [12]	400 [12]
Microhardness	$N.mm^{-2}$	1250 [12]	1350 [12]
Mobility (300K): electrons holes	$cm^2.V^{-1}.s^{-1}$	350 [12] 40 [12]	540 [12] 28 [12]
Electron effective mass: m_e/m		0.165 [12]	n.a.
Hole effective mass: m_h/m		0.800 [12]	n.a.
Energy gap	eV	2.42 [12]	2.67 [10]
Temperature dependence of gap: dE_g/dT	$x10^{-4} eV.K^{-1}$	-5.0 [12]	-7.2 [12]
Pressure dependence of gap: dE_g/dP	$x10^{-6} eV.cm^2.kg^{-1}$	3.3 [12]	6.0 [12]
Heat of formation (300K)	$kJ.mol^{-1}$	n.a.	422 [12]
Electron affinity	eV	4.5 [13]	4.0 [13]
Refractive index		2.32 [12]	2.89 [12]
Conductivity		n [10]	n, p [10]
Solubility product		10^{-29} [13]	n.a.
Phillips ionicity		0.69 [13]	0.68 [13]
Pauling ionicity		0.60 [13]	0.60 [13]

Table 2.1: Properties of CdS and ZnSe.

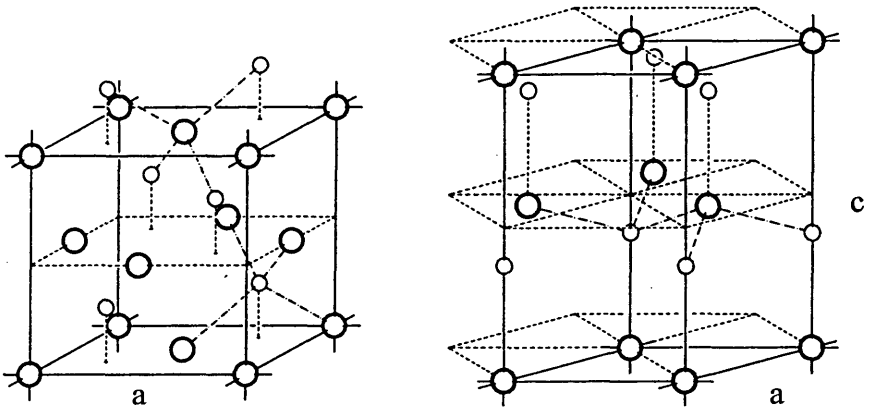

Figure 2.7: Structure of (a) sphalerite and (b) wurtzite (O metal, o chalcogen).

2.3.2 Properties of $CuInSe_2$

This section, which summarises the properties of $CuInSe_2$, helps understanding the choice of this material as an absorber semiconductor in solar cell technology. It will be shown that $CuInSe_2$ has several interesting properties that make it suitable for high efficiency photovoltaic devices, such as

- A direct band gap with nearly optimum values for either homojunction or heterojunction devices;
- A high optical absorption coefficient which minimises the requirement for high minority carrier diffusion length;
- The possibility to produce n- and p-type material so that the formation of homo-junction as well as heterojunction devices is feasible;
- A good lattice match and electron affinity match with window materials so that heterojunctions with low interface state densities can be formed and deleterious conduction band spikes can be avoided.

The properties of $CuInSe_2$ are reported in Table 2.2.

Property	Unit	Typical Value
Stable structure		Chalcopyrite [12]
Space group		$I\bar{4}2d - D_{2d}^{12}$ [12]
Molecular weight	$g.mol^{-1}$	336.29 [12]
Density	$g.cm^{-3}$	5.77 [12]
Colour		Grey [14]
Temperature of transition to sphalerite structure	K	1083 [14]
Melting point	K	1600 [12]
Lattice parameters (300K): a c	Å	5.785 [12] 11.56 [12]
Bond length: Cu–Se In–Se	Å	2.43 [15] 2.57 [15]
Thermal expansion coefficient (300K))	$10^{-6} K^{-1}$	6.6 [12]
Thermal conductivity (300K)	$mW.cm^{-1}.K^{-1}$	37 [12]
Specific heat: c_1 c_2 c_3	K^{-1}	$7.67x10^{-4}$ [14] $4.06x10^{-6}$ [14] $4.3x10^{-9}$ [14]
Debye temperature	K	221.9 [14]
Microhardness	$N.mm^{-2}$	2050 [12]
Volume Compressibility	$10^{-10} m^2.N^{-1}$	0.187 [12]
Dielectric constant: low frequency high frequency		13.6 ± 2.4 [14] 8.1 ± 1.4 [14]
Sound velocity (longitudinal)	$cm.s^{-1}$	$2.2x10^5$ [14]
Electrical resistivity (polycrystalline films): Cu-rich In-rich	Ω.cm	0.001 [14] > 100 [14]
Mobility (300K): electrons ($n = 10^{14} - 10^{17} cm^{-3}$) holes ($p = 8.10^{15} - 6.10^{16} cm^{-3}$)	$cm^2.V^{-1}.s^{-1}$	100 – 1000 [14] 50 – 180 [14]
Electron effective mass: m_e/m		0.09 [14]
Hole effective mass (heavy): m_{hh}/m		0.71 [14]
Hole effective mass (light): m_{lh}/m		0.092 [14]
Energy gap	eV	1.04 [5]
Temperature dependence of gap (77 – 300 K): dE_g/dT	$x10^{-4}$ eV.K^{-1}	-2 ± 1 [14]
Pressure dependence of gap: dE_g/dP	$x10^{-6}$ eV. $cm^2.kg^{-1}$	2.8 [14]
Heat of formation of 1 mole from isolated elements	Kcal	-48 [16]
Phillips ionicity		0.61 [13]
Pauling ionicity		0.43 [13]
Solubility product		10^{-73} [13]
Conductivity		n, p [5]
Electron affinity	eV	4.6 [13]
Absorption coefficient	cm^{-1}	10^5 [17]

Specific heat: $C_p(T) = 12R[F(\Theta + c_1T + c_2T^2 + c_3T^3]$ where R is the molar gas constant and F is the Debye function.

Table 2.2: Properties of $CuInSe_2$.

2.3.2.1 Structural properties

$CuInSe_2$ crystallises in the chalcopyrite structure (Figure 2.8) [11, 12]. The closed packed planes in the chalcopyrite lattice are the (112) planes (corresponding to the (111) planes in the sphalerite structure), which consist of a double layer of anions (Se) and cations (Cu, In) [5].

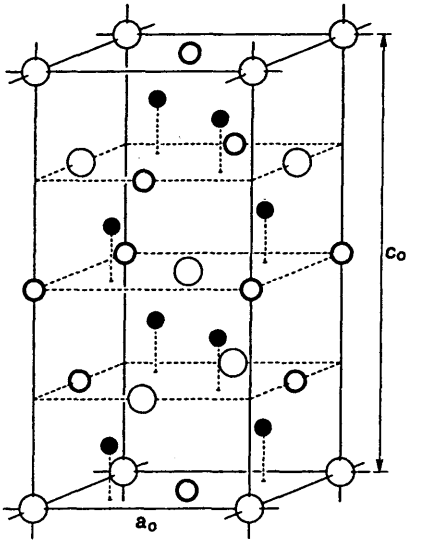

Figure 2.8: Structure of the chalcopyrite (○ Cu, O In, ● Se).

Whatever the preparation technique used, $CuInSe_2$ shows generally a preferential orientation growth along the <112> direction [18]. It is also often reported that Cu-rich films are considerably more crystalline than In-rich films [18, 19].

2.3.2.2 Compositional properties

It appears that chalcopyrite structure can be maintained over a wide range of composition by the incorporation of intrinsic defects in the crystal lattice [5]. Taking into consideration only the simplest defects, namely, vacancies, interstitial atoms and antisite defects, one can expect 12 possible types of defects in $CuInSe_2$: V_{Cu}, V_{In}, V_{Se}, Cu_i, In_i, Se_i, Cu_{In}, In_{Cu}, Cu_{Se}, Se_{Cu}, In_{Se} and Se_{In}. Defect pairs, such as $(2V_{Cu} + In_{Cu})$, have low formation energies, which can explain the existence of non-stoichiometric ordered compounds [20]. It is also often observed that $CuInSe_2$ is not uniformly grown and that the stoichiometry of the films varies between the bulk and the surface of the films [21]. Thus, it has been reported that slightly In-rich films ($Cu/(Cu+In) < 0.5$) presented highly In-rich surfaces ($In/(Cu+In) > 0.75$). This phase corresponds to

$CuIn_3Se_5$ compound. Similarly, a Cu_2Se phase has been found to cover Cu-rich $CuInSe_2$ films. It is therefore unlikely to have pure stoichiometric $CuInSe_2$ films on the surface. Two different processes have explained these phenomena: the bulk effects and the surface effects [13]. The bulk effects involve the diffusion of excess ions through the surface of the grains to form a new stable compound. The surface effects involve the drift of excess ions through the surface due to the electric field created by the surface band bending. Guillen and Herrero have also shown that the simultaneous presence of In_2Se_3 and Cu_2Se was possible in as-deposited films [22].

2.3.2.3 Morphological properties

The morphology of $CuInSe_2$ strongly varies according to the growth process used and the composition of the material so that it is not an easy task to fully describe it. However, it is generally reported that polycrystalline $CuInSe_2$ grown by conventional techniques has a morphology consisting of densely packed particles with sizes up to 10 μm (obtained for electrodeposited $CuInSe_2$ after selenisation [23] and for $CuInGaSe_2$ by rapid thermal processing (RTP) [24]). Bhattacharya et al. have shown by scanning electron microscopy that the surface of electrodeposited Cu-Se films contained long narrow grains [25]. This information can be useful for identification of the Cu_2Se phase covering the surface of Cu-rich $CuInSe_2$, as the x-ray diffraction pattern of these two compounds is very similar and it is not easy to differentiate the peaks relative to $CuInSe_2$ from those relative to Cu_2Se.

2.3.2.4 Electrical properties

As mentioned earlier, the $CuInSe_2$ crystal lattice may contain several defects, which are considered as the main electrically active defects. In fact, the conductivity type of $CuInSe_2$ is usually determined by the non-stoichiometry of the crystal instead of an external doping by shallow level impurities. Thus, the crystal lattice defects give rise to donor or acceptor levels, as summarised in table 2.3 and 2.4.

Copper-rich films and indium-rich films are generally reported to be p-type and n-type, respectively [5]. It is noteworthy that the $Cu_{2-x}Se$ phase covering the surface of Cu-rich $CuInSe_2$ films is highly conductive and therefore not suitable for photovoltaic solar cell devices [21]. Schmid et al. [21] also showed that n-type $CuIn_3Se_5$ was present at the

surface of slightly indium-rich films (see Section 2.3.2.2), which could be responsible for the formation of a p-n heterojunction between the p-type bulk $CuInSe_2$ and this n-type surface layer. This model could therefore change the usual $CuInSe_2$/CdS solar cell structure to a $CuInSe_2$/$CuIn_3Se_5$/CdS structure. Note also that the formation of this surface layer could also alter the properties of the metal-semiconductor or liquid-semiconductor junctions.

Energy ($E_c - E$) (meV)	Defect assignment
5 – 20	V_{Se}, In_{Cu}, Cu_i, Se_{Cu}
30 – 45	In_{Cu}
55 – 70	Cu_i, V_{Se}, In_i
80 – 115	In_i, V_{Se}, In_{Se}
180 – 225	In_i

Table 2.3: Identification of donor energy levels observed in the $CuInSe_2$ [26].

Energy ($E - E_v$) (meV)	Defect assignment
12 – 30	V_{Cu}, Cu_{In}, V_{In}, Se_i, Se_{In}, Cu_{Se}
40 – 70	V_{Cu}, Cu_{In}, Se_i, V_{In}
80 – 100	V_{Cu}, V_{In}, Se_i, Se_{In}
110 – 130	Cu_{Se}
250 – 400	Impurities

Table 2.4: Identification of acceptor energy levels observed in the $CuInSe_2$ [26].

2.3.2.5 Optical properties

$CuInSe_2$ is a direct gap semiconductor with high absorption coefficient at the band gap energy (10^5 cm^{-1}) [17]. Its accepted band gap is 1.04eV [5] but can be tailored to higher values by addition of elements, such as Ga [27], S [28] or Al [29]. It is therefore in the range of optimum band gap materials ($1.1eV < E_g < 1.6eV$), according to Loferski [30]. The optical characteristics of $CuInSe_2$ compounds are closely related to the defects of the crystal lattice, which introduce levels within the band gap, as seen in Section 2.3.2.4. Therefore, donor or acceptor levels can lower the measured band gap of $CuInSe_2$ when compared to its theoretical value. Tuttle et al. also reported a phenomenon of excessive sub-band gap absorption relative to the presence of the p-type degenerated secondary phase $Cu_{2-x}Se$ [31]. A second optical transition above the band gap is also observed and could be related to a spin-orbit valence band splitting, Δ_{so}, of 0.22-0.24 eV [31] or ~0.50 eV [32]. It is noteworthy that the band gap of the $CuIn_3Se_5$ phase,

present in In-rich $CuInSe_2$ is reported to be higher than the one of stoichiometric $CuInSe_2$ (1.3eV) [21].

2.3.2.6 Influence of Ga on $CuInSe_2$ properties

Addition of gallium to $CuInSe_2$ has been widely used, as it is reported to improve the device performances. The relatively low band gap energy of $CuInSe_2$ (1.04 eV) is responsible for the low open circuit voltage generally observed in solar cells made of this material [33]. As indium is replaced by gallium, the band gap energy of the chalcopyrite compound is raised to a maximum value of 1.68 eV, which is the band gap energy of $CuGaSe_2$ [5]. The larger band gap of $CuIn_xGa_{1-x}Se_2$ alloys is responsible for a higher built-in potential of the device, which results in the increase of the open circuit voltage. It is noteworthy that it can also provide a better match to the solar spectrum. The dependence of the band gap energy on x can be described by [27]

$$E_g(x) = 1.02 + 0.67x + 0.11x(x-1) \tag{2.8}$$

The structural properties of $CuInSe_2$ also change when adding Ga to the films, with the shift of x-ray diffraction peaks towards higher angles. The lattice parameters a and c therefore decrease with increasing the gallium content in the films [34], the reason being that indium atoms are substituted for smaller gallium atoms [35]. The variations of a and c are given in angstrom units by [36]

$$a = 5.618 + 0.163x \tag{2.9}$$

and

$$c = 11.01 + 0.59x \tag{2.10}$$

Schroeder et al. have shown that epitaxial $CuIn_xGa_{1-x}Se_2$ ($0.03<x<1$) films were always p-type and that the acceptor density was increasing dramatically with increasing the gallium content in the films [37].

Addition of sulphur atoms, which replace selenium atoms, has also been used to increase the band gap of $CuInSe_2$ and to passivate the surface and grain boundaries of the layers [38, 39].

2.3.2.7 Influence of Na on $CuInSe_2$ properties

It is of great interest to understand how sodium affects the performances of CIS thin film solar cells, as it has been widely observed that it diffused from the soda lime glass, traditionally used as a substrate in photovoltaic devices, through the surface of the films [40, 41]. Na is also located in grain boundaries within the polycrystalline films [42, 43]. It has been found to improve the efficiency of the CIS-based solar cells in many ways. Ruckh et al. reported an increased electrical conductivity, a reduced space charge width and a higher V_{oc} for films prepared on soda lime glass as compared to those prepared on Na-free glass substrates [40]. Other groups reported an enhancement in the grain size of CIGS crystals [44], a stronger (112) orientation [45] and a higher fill factor [44]. The improvement in the electrical performances due to sodium seems to stem from a higher effective acceptor concentration in the absorber material [37, 40, 45, 46].

Four models have been proposed to explain this phenomenon:

- The oxygen model is based on two well-established results: annealing CIS in an oxidising atmosphere leads to an improvement in photovoltaic conversion efficiency and alkali atoms are known to promote oxidation of many semiconductor surfaces catalytically. The increase in the acceptor density could then be due to the neutralisation of donor-like Se vacancies through a promoted chemisorption of oxygen in the presence of sodium species [40]. The observation that the oxygen content at the surface increases with the sodium content in the film further supports this model [45].
- The In_{Cu} model has been proposed by Contreras et al [45]. Here, the enhancement in the electrical conductivity and photovoltaic device performances is attributed to the annihilation of donor states (i.e., In_{Cu}) by sodium during CIS growth. This model was promoted by Wei et al. whose thermodynamical calculations lead to a strongly exothermic formation energy of the $Na_{In_{Cu}}$ defect [47]. It can also explain the better crystallinity reported for Na-containing CIS films, as the annihilation of In_{Cu} defects leads to a better ordering of the cations.

- The Na_{In} model proposed by Niles et al. suggests that the increase in the effective acceptor density is due to the direct creation of acceptors, such as antisite defect Na_{In} [42].
- The Na_{Cu} model proposed by Stanbery et al. is based on Cu substitution for Na to form $Na_3Cu_2In_5Se_{10}$ or $NaInSe_2$ phases, which segregate on the surface of the film and lead to shallow acceptor states [48]. This argument is supported by the findings of Klein et al. who showed that the deposition of Na on cleaved $CuInSe_2$ caused a reduction in the Cu 3d contribution to the valence band density of states [49].

It may be important to note that contact of the CIS layers with water is reported to decrease the device performance due to Na removal from the surface [50, 51].

2.4 Growth techniques of $CuInSe_2$

$CuInSe_2$ ingot crystals have been produced using a wide range of melt grown techniques, such as horizontal and vertical Bridgman methods [52, 53], travelling heater method [54] and freezing technique [55]. However, in this section, one will concentrate on the techniques used to grow thin solid films of $CuInSe_2$. Among all these methods, electrodeposition will be described more in detail, as it is the one used to grow the layers in this project. The advances made to date in electrodeposition of $CuInSe_2$ are also mentioned.

2.4.1 Electrodeposition

Electrodeposition of metal and metallic alloys has been used for more than a century but the application of this technique to grow semiconductors has been limited until recently, physicists having more confidence in high vacuum methods. However, electrochemical deposition from aqueous solution appears to be a promising technique for deposition of semiconductors, as it is low cost and requires a simple set-up and low power. It can be easily scaled up for commercial purposes and can yield very high purity materials with the possibility to purify further the starting chemicals present in the electrolytic solution.

2.4.1.1 Theory of electrodeposition

A basic electrochemical cell consists of two electrical conductors called electrodes, each immersed in a suitable electrolyte solution [56, 57]. Within the electrolyte, electricity is carried by the movement of ions and involves the reactions of oxidation and reduction. The positive ions or cations move towards the cathode where they discharge and this process is called reduction. The negative ions or anions move towards the anode where they release electrons. This is the reaction of oxidation. The simultaneous discharge of one cation at the cathode and one anion at the anode (both having a charge $\pm e$) is equivalent to the transport of one electron from the cathode to the anode through the electrolyte.

From thermodynamics, it can be shown that the cell potential, E_{cell}, is related to the free energy of the reaction, ΔG, by the relationship

$$\Delta G = -nFE_{cell} = -nF(E_{cathode} - E_{anode}) \tag{2.11}$$

where F is the Faraday constant and n the number of moles of electrons associated with the oxidation/reduction process. $E_{cathode}$ and E_{anode} are the cathode and anode potentials, respectively.

In the process of cathodic deposition used in this work, the relevant reaction is the reduction. Now, considering the reduction $oA_{ox} + ne^- \rightarrow rA_{red}$, Nernst defined the electrode potential or equilibrium potential of the couple A_{red} / A_{ox} as

$$E_A = E_A^o + \frac{RT}{nF}\ln\frac{(A_{ox})^o}{(A_{red})^r} \tag{2.12}$$

where E_A^o is the standard electrode potential of the couple A_{red} / A_{ox}, (A_{red}) and (A_{ox}) are the molar activities of the reduced and oxidised form of the substance A, respectively.

The electrode potential of a redox couple is measured with respect to the standard hydrogen electrode, the potential of which has been defined to be zero at all temperatures. In addition, the molar activities of its oxidised form and reduced form are equal to unity. The other available reference electrodes have been made with their

potential fixed with respect to the standard hydrogen electrode. The most widely marketed reference electrode is the Ag/AgCl electrode whose standard potential is 0.205V with respect to standard hydrogen electrode. This reference electrode has the advantage that it can be used at temperatures higher than 60°C.

The Nernst equation of a redox couple is useful for anticipating the reaction, which will occur in a cell by knowing the activities of the species in the electrolyte. Thus, if the electrode potential is positive, the free energy of the reaction will be negative and the reaction of reduction will be spontaneous. Inversely, if the electrode potential is negative, the free energy of the reaction will be positive. Therefore, one needs to apply a potential more negative than the electrode potential of the red/ox couple to force the reaction of reduction. The actual electrode potential is always greater than the one computed from the Nernst equation (i.e., more negative at the cathode and more positive at the anode). This difference known as overpotential is mainly due to the polarisation at the electrodes. The co-deposition of binary or ternary compounds requires the equality in the actual electrode potentials of all the elements forming the compound. For example, the condition for the simultaneous deposition of three elements A, B and C having the electrode potentials E_A, E_B and E_C and the overpotentials η_A, η_B and η_C, respectively, can be written as

$$E_A + \eta_A = E_B + \eta_B = E_C + \eta_C \tag{2.13}$$

Thus, the direct electrodeposition of binary or ternary compounds is rather difficult because the conditions favourable for the deposition of one constituent differ from those necessary for the others. One difficulty comes obviously from the disparate values of the equilibrium potentials. Another problem to deal with is the hydrogen evolution happening below a given potential, which can deteriorate the quality of the deposited films. In order to bring the potentials of the constituents closer, it is possible to adjust the composition of the solution. A decrease in the concentration of one type of ion does not change the equilibrium potential greatly but can introduce significant concentration polarisations. One can alternatively decrease the deposition rate of one element by the addition of a complexing agent to the electrolyte.

To determine the conditions of deposition, it can be useful to plot the electrode potentials of the species to be deposited versus the pH of the electrolyte. These diagrams

called Pourbaix diagrams give a possible potential and pH region for the deposition of the required material [58]. However, it must be kept in mind that these diagrams ignore the overpotentials, and moreover, the fact that the thermodynamic conditions for the deposition of one element can be modified by the co-deposition of another element, in particular in the case of a definite compound. Another practical way of establishing the deposition conditions for elements or compounds is voltammetry. The current-voltage characteristics (I_{dep}-vs-V_{dep}) for the deposition of a multinary compound generally present a plateau current region, which gives a possible deposition voltage range.

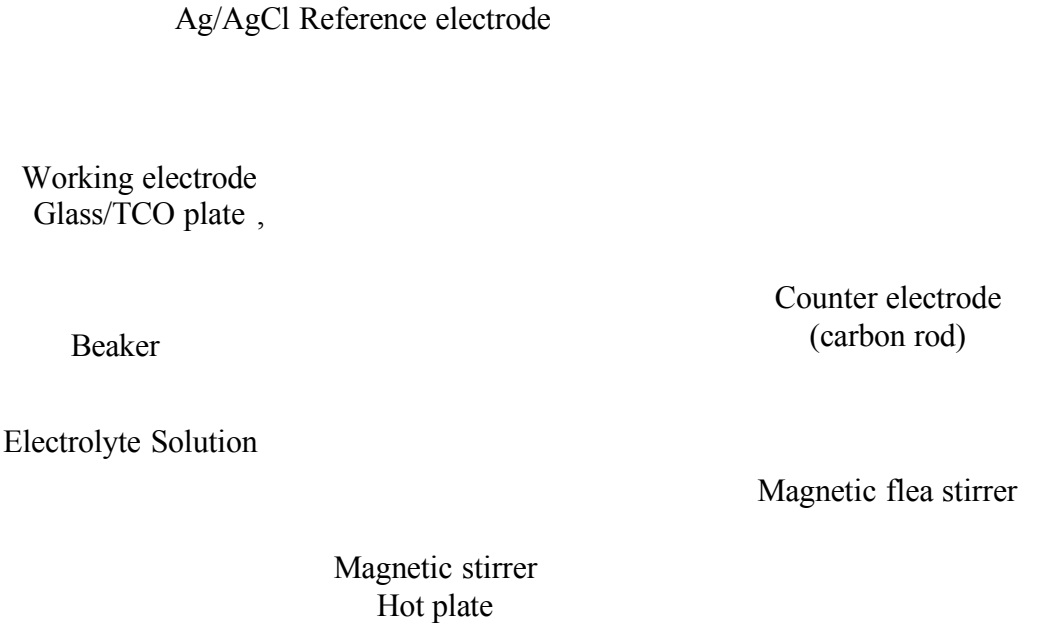

Figure 2.9: Schematic diagram of the three electrode cell.

During the cathodic deposition, there are continuous fluctuations of the cathode potential owing to the change of the cell parameters (concentrations of ions in the electrolyte, overvoltages, conductivity of the substrate). Hence, these changes will reduce the quality of the deposited layer. A typical arrangement used to overcome this problem consists of a three-electrode cell (see Figure 2.9). The three electrodes are called the working electrode, the counter electrode and the reference electrode. This technique is called potentiostatic electrolysis and involves establishing a constant potential on the working electrode with respect to the reference electrode by means of an electronic potentiostat.

The counter electrode keeps the potential difference unchanged between the cathode and the reference electrode.

The theoretical thickness T of an electrodeposited film can be evaluated by [59]

$$T = \frac{1}{nFA}\left(\frac{ItM}{\rho}\right) \tag{2.14}$$

where I is the delivered current, t is the time of deposition, M is the molecular weight, n is the number of electrons transferred, F is the Faraday's number, A is the area of the electrode and ρ is the density of the deposited material.

However, this equation gives only an approximate value of the thickness, as it does not take into account the formation of other elements or compounds through reduction and oxidation processes, which do not deposit on the working electrode (hydrogen and oxygen gases, for example). In addition, as the molecular weight and density of a particular compound vary with its composition, one has to estimate an average value for these two parameters.

2.4.1.2 Electrodeposition of $CuInSe_2$

The basic individual reactions for the deposition of copper, indium and selenium and their related Nernst equations are

$$Cu^{2+} + 2e^- \leftrightarrow Cu$$

$$E_{Cu} = E^o_{Cu} + \frac{RT}{2F}\ln\frac{(Cu^{2+})}{(Cu)} = 0.135 + 0.0295\log\frac{(Cu^{2+})}{(Cu)}$$

$$In^{3+} + 3e^- \leftrightarrow In$$

$$E_{In} = E^o_{In} + \frac{RT}{3F}\ln\frac{(In^{3+})}{(In)} = -0.545 + 0.0197\log\frac{(In^{3+})}{(In)}$$

$$H_2SeO_3 + 4H^+ + 4e^- \leftrightarrow Se + 3H_2O$$

$$E_{Se} = E^o_{Se} + \frac{RT}{4F}\ln\frac{(H_2SeO_3)}{(Se)} + \frac{3RT}{4F}\ln(H^+)^3 = 0.535 + 0.0148\log\frac{(H_2SeO_3)}{(Se)} - 0.0433pH$$

where $E°_{Cu}$, $E°_{In}$ and $E°_{Se}$ are the standard electrode potentials of Cu, In and Se, respectively with respect to the Ag/AgCl reference electrode. (Cu^{2+}), (In^{3+}) and (H_2SeO_3) refer to the activities of the respective ions in the solution. (Cu), (In) and (Se) represent the activities of the respective atoms in the electrodeposit, which are equal to 1 for pure elemental deposition.

It can be seen from the Nemst equations that the electrode potentials for selenium and copper are more positive than that of indium. Thus, the deposition of selenium and copper will precede the deposition of indium. Consequently, for the simultaneous deposition of Cu, In and Se, the pH of the electrolyte may be adjusted so that the electrode potentials of all the individual deposits may come closer to each other.

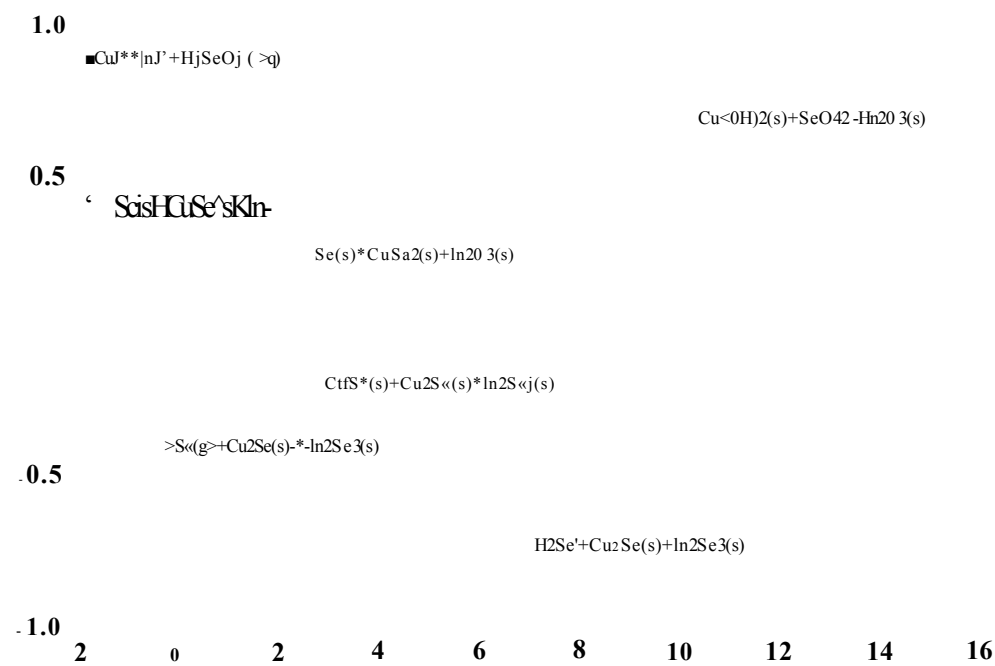

Figure 2.10: Pourbaix diagram showing corrosion, passivation and immunity domains of $CuInSe_2$. The electrode potential E is plotted with respect to hydrogen reference electrode at room temperature [60]. The yellow region corresponds to the possible range of pH and voltage for $CuInSe_2$ deposition.

The Pourbaix diagram of $CuInSe_2$ shown in Figure 2.10 is a useful tool to predict the different compounds one can obtain by just varying the deposition voltage and the pH. However, as discussed before, one has to remember that this is only a superposition of the three Pourbaix diagrams of the pure elements involved in the electrodeposition of $CuInSe_2$. As a matter of fact, the deposition of one element can act as a catalyst for the codeposition of another element.

In order to electrodeposit $CuInSe_2$, it is also possible to adjust the composition of the solution. This way, Vedel proposed a model, where the Se(IV):Cu(II) ratio would control the stoichiometry of the deposited film in the presence of excess In(III) in the electrolyte [61]. In this model, Cu(II) and Se(IV) are reduced into Cu_2Se and elemental Cu for low concentration of Se(IV) or elemental Se for high concentration of Se(IV). For low concentrations of Se(IV), the Cu_2Se phase can be further reduced in the presence of In(III) to form $CuInSe_2$ but the film will still remain Cu-rich. For high concentrations of Se(IV), the excess of Se can be reduced into Se(-II) and further react with In(III) to form In_2Se_3 compound leading to In-rich films. These results are summarised in Table 2.5.

	-0.95 < E(V) < -0.60	**-0.60 < E(V) < -0.25**	**-0.25 < E(V) < -0.20**
$\alpha > 2$	$CuInSe_2 + (\alpha-2)/3\ In_2Se_3$		$CuSe + (\alpha - 1)\ Se$
$0.5 < \alpha < 2$	$\alpha/2\ CuInSe_2$	$(2\alpha - 1)/3\ CuInSe_2 + (2 - \alpha)/3\ Cu_2Se$	$Cu_2Se + CuSe$
$0 < \alpha < 0.5$	$+ (1 - \alpha/2)\ Cu$	$(1-2\alpha)\ Cu + \alpha\ Cu_2Se$	

Table 2.5: Reaction products of the electrodeposition reactions as a function of the flux ratio $\alpha = J_{Se}/J_{Cu} = kC_{Se}/C_{Cu}$ (here, $k = 1.2$) and applied potential. In(III) is supposed to be in excess. The potentials are referred to the standard hydrogen electrode.

The first attempt to electrodeposit $CuInSe_2$ was reported by Bhattacharya [62]. The electrolyte contained CuCl, $InCl_3$ and SeO_2, complexed by triethanolamine and ammonia. However, the deposits obtained were rather amorphous. Another approach consisted of preparing a Cu-In film followed by a chemical treatment of selenisation but it was found difficult to obtain stoichiometric $CuInSe_2$ films [63, 64]. Other groups used pulse-plated electrodeposition, which showed good results after heat treatment [65, 66]. Several studies concerning $CuInSe_2$ electrodeposition have been made in the galvanostatic mode. However, a weak variation of current may induce large modifications of deposit composition, so it seems more logical to work under potentiostatic conditions. In the potentiostatic mode, most groups work at room temperature and at low pH (about 1.5) [67, 68, 69, 70] or using a complexing agent [16, 32, 71, 72, 73]. Nakamura et al [74] found that the reproducibility and uniformity of the film composition were improved by stirring the solution. Concerning the deposition potential, a wide range has been tried depending on the reference electrode, the concentration of reactants and the substrate used. As expected, the ratio of indium over copper increases with more negative electrodeposition potentials [75]. However, the crystallinity of the films considerably decreases from copper-rich to indium-rich films

[76]. Kampmann et al. also showed that the indium content in the films increased with deposition time [75]. Generally, the electrodeposited $CuInSe_2$ thin films are found to have a (112) preferential plane orientation [18]. The as-deposited films before heat treatment usually show weak XRD peaks, which is attributed to poor crystallinity but a great improvement in the sharpness and intensity is observed after annealing [18]. Vedel et al [18] thus reported that annealing in argon between 350°C and 400°C for 30 minutes enhanced the crystallinity of the films. It appeared that an increase of the annealing time beyond 30 minutes did not lead to a better crystallinity and that heat treatment at higher temperatures than 400°C gave rise to a loss of the (112) preferred orientation and degradation of the films (formation of pinholes). It has also been found that annealing under selenium atmosphere improves further the crystallinity [61]. Guillen and Herrero [32] have confirmed that a combination of thermal and cyanide chemical treatment led to an improvement in the compositional and optical properties of electrodeposited thin films.

2.4.2 Other conventional growth techniques

It is reported that $CuInSe_2$ thin films have been grown using various other techniques than electrodeposition, such as thermal evaporation [77, 78, 79], molecular beam epitaxy (MBE) [80], chemical vapour deposition (CVD) [81, 82, 83], sputtering [33, 84, 85, 86], pulsed laser deposition (PLD) [87], flash evaporation [88, 89], spray pyrolysis technique [90], electroless deposition [91], ionised cluster beam deposition [92], chemical bath deposition [93] and thermal processing of stacked precursor layers [94, 95, 96, 97]. In this section, one gives a brief description of all these techniques applied to the deposition of $CuInSe_2$.

2.4.2.1 Thermal evaporation

Evaporation is the most common method to prepare $CuInSe_2$ thin films. It is a vacuum process, where elemental Cu, In and Se [77] or some compounds containing all these elements are evaporated [79] by electrical heating. The vaporised atoms travel in a straight line before they collide with the substrate and form the expected $CuInSe_2$ thin film. Evaporation can be either simultaneous [77] or sequential [78] and involves the heating of the substrate to improve the quality of the layers [77].

2.4.2.2 Molecular beam epitaxy (MBE)

High quality $CuInSe_2$ films have also been prepared by MBE [80], which is a high vacuum evaporation process for deposition of epitaxial layers. This method is particularly suitable for precise control of the composition and thickness of the films but is a very expensive and slow process. Therefore, this technique is designed for growing high quality materials for small devices and is not suitable for terrestrial-scale production.

2.4.2.3 Chemical vapour deposition (CVD)

CVD is a process whereby a thin film is deposited from a gaseous phase by a chemical reaction occurring on a heated substrate surface. High quality $CuInSe_2$ thin films have been produced using several types of CVD process [81, 82, 83]. In metalorganic chemical vapour deposition (MOCVD), metalorganic precursors are used for copper and indium, which react with hydrogen selenide to form a $CuInSe_2$ film with controlled thickness and composition [82]. Jones et al. produced stoichiometric CIS films using the plasma-enhanced chemical vapour deposition [83]. Here, a glow discharge is produced in the gaseous reactant mixture, which is maintained at a pressure of 0.1-1 torr under a radio frequency (RF) plasma. $CuInSe_2$ has also been produced by close space chemical vapour transport (CSCVT) [81]. In CSCVT, a gas, hydrogen iodide, is used to form a volatile compound with a sintered CIS source. This volatile species subsequently undergoes the reverse chemical reaction on the substrate to form homogeneous $CuInSe_2$ thin films.

2.4.2.4 Sputter deposition

Several attempts of depositing $CuInSe_2$ by sputtering have been reported [33, 84]. Sputter deposition is a vacuum process, which consists of the ejection of atoms from a material through the collision of fast non-reactive ions (usually Ar ions) with its surface. As for evaporation, the ejected atoms are then condensed on a substrate to form the required coating. Sputter deposition technology includes many variations of the basic process described above. The target itself to deposit $CuInSe_2$ can change. For example, Tanaka et al. prepared $CuInSe_2$ and $CuIn_{1-x}Ga_xSe_2$ by RF sputtering from $CuInSe_2$ and $CuIn_{1-x}Ga_xSe_2$ targets, respectively [84] whereas Nakada et al. used three-source

magnetron sputtering from elemental targets of Cu, In and Se [33]. Magnetron sputtering is used to reduce the heat of the substrate due to the bombardment of its surface by electrons. RF methods are often used [33], as non-conducting targets cannot be sputtered by DC methods. Tseng et al. reported the deposition of $CuInSe_2$ by reactive sputtering in which Cu and In were sputtered in an Ar + H_2Se atmosphere. Cu and In then reacted with H_2Se at the substrate to form the $CuInSe_2$ film. A hybrid sputtering and evaporation method has also been used to deposit CIS thin films from sputtered Cu and In fluxes and evaporated Se [86].

2.4.2.5 Pulsed laser deposition (PLD)

In this technique, a CIS powder is vaporised and ejected from the surface of a target as a laser beam irradiates it. $CuInSe_2$ films are formed by condensing the material ablated from the target onto the substrate. By choosing adequate deposition parameters, homogeneous films of single phase CIS can be prepared [87].

2.4.2.6 Flash evaporation

In flash evaporation, $CuInSe_2$ powder is dropped from a hopper onto a superheated sheet to produce a complete evaporation of all the elements, which get deposited on the substrate [88]. The film composition can be changed by modifying the deposition parameters, such as the crucible and substrate temperatures and the deposition rate. Thus, the atomic concentration ratio Cu/In is found to increase with the crucible temperature and decrease when the deposition rate increases. The (Cu+In)/Se ratio also increases with the substrate temperature [89].

2.4.2.7 Spray pyrolysis technique

The growth of $CuInSe_2$ by the spray pyrolysis technique involves spraying a solution containing soluble salts of copper and indium and N, N-dimethyl selenourea (NDSU) onto a heated substrate. The sprayed droplets undergo pyrolytic decomposition and subsequent reactions at the surface of the substrate to form a well-crystallised thin film. Excess NDSU over stoichiometric amount is used to compensate for the loss of selenium during pyrolysis [90].

2.4.2.8 Electroless deposition

Electroless deposition differs from electrodeposition in that no external current source is required. It involves immersing a conducting glass substrate or a noble metal connected with an easily oxidisable metal, which acts as the anode, in a deposition bath containing the required ions and complexing agents. There is creation of an electrochemical potential difference between the two electrodes without applying an external voltage. Thus, Pattabi et al. used an Al counter electrode immersed in an aqueous solution containing $CuCl_2$, $InCl_3$, H_2SeO_3 and LiCl. $CuInSe_2$ thin films have been grown on both Mo and ITO substrates [91].

2.4.2.9 Ionised cluster beam deposition

Kondo et al. used ionised cluster beam deposition to grow $CuInSe_2$ thin films [92]. In this system, vaporised Cu, In and Se are subjected to adiabatic cooling and loosely united to form cluster beams. These cluster beams are positively ionised by the bombardment of electrons and deposited onto a heated substrate.

2.4.2.10 Chemical bath deposition

Chemical bath deposition involves producing the required ions in a solution by chemical means, which combine and precipitate out onto the substrate, if the right equilibrium conditions are met. Vidyadharan Pillai et al. used a mixture of copper citrate, indium citrate and sodium selenosulphite to deposit $CuInSe_2$ on SnO_2 conducting glass substrates [93].

2.4.2.11 Thermal processing of stacked precursor layers

In this technique, stacked precursor layers of Cu, In and Se are first deposited on a substrate and then annealed to form the $CuInSe_2$ film. There are several variants of this method depending on the stacked precursor layers used, the thermal process and the atmosphere where the annealing step is performed. In the stacked elemental layer (SEL) technique, elemental layers of Cu, In and Se are sequentially deposited on a substrate, generally by evaporation, and then thermally processed either in vacuum or in an inert gas atmosphere to synthesise the ternary compound [94]. Kundu et al. used a rapid

thermal furnace instead of the conventional annealing furnace and obtained high quality CIS films free from the secondary binary phases (e. g. Cu_2Se and In_2Se_3) [95]. Another frequently used technique is the selenisation, which consists of annealing the stacked precursor layers in H_2Se atmosphere. The stacked precursor layers are generally prepared by evaporation [96], sputtering [97] or electrodeposition [68].

2.5 Processes for solar cell completion

Solar cell completion is a crucial part of device fabrication, which generally involves three main steps: the heat treatment of as-deposited materials, the etching of material surfaces and the formation of metal contacts, either rectifying or ohmic, depending on the desired structure. The following sections explain these three fundamental steps with a brief review of the research achieved by other groups working in this field.

2.5.1 Heat treatment

Annealing in air plays a central role for improving $CuInSe_2$ thin film solar cells through the passivation of the grain boundaries and the increase of the minority carrier diffusion length [98]. It is also common observation that air annealing of as-deposited chalcopyrite films leads to an increase of the p-type conductivity [99], which could be explained by the annihilation of donor states due to the substitution of selenium vacancy by oxygen atoms [100]. Hariskos et al. reported that thermal oxidation of Cu-poor $CuIn_{1-x}Ga_xSe_2$ in air leads to the formation of In_2O_3, Ga_2O_3 and SeO_2 at the surface [101]. No Cu_xO was observed. They also showed the appearance of these oxides, at a lower extent, in the as-deposited samples. Dirnstorfer et al. found that the oxidation of gallium was more effective than the oxidation of the other elements probably due to its higher diffusion coefficient [102]. Whatever the atmosphere, annealing of as-deposited samples is found to improve the crystallinity [22] and to sharpen the optical band gap edge [32]. The loss of Se-excess is generally observed during heat treatment of $CuInSe_2$ [32], as its boiling point is very low when compared to those of copper and indium. This loss and the recrystallisation involve the reduction of degenerate phases and defect levels, which were responsible for the excessive sub-band-gap absorption in as-deposited $CuInSe_2$ (see Section 2.3.2.5). Annealing under selenium atmosphere has been found to be the most effective heat treatment for improving the crystallinity and the

optoelectronic properties of the films [61]. Table 2.6 gives some examples of annealing conditions generally used to improve the quality of electrodeposited samples of CdS, ZnSe and $CuInSe_2$. Table 2.7 displays the melting temperatures, boiling temperatures and vapour pressures of the elements involved in these compounds, as they can play an important role in the annealing process. Samples were heat treated in a Bio-Rad alloying furnace.

Compound	Annealing temperature (°C)	Annealing time (min.)	Atmosphere	Reference
CdS	450	20	N_2	[103]
ZnSe	200	15	Air	[104]
$CuInSe_2$	350	30	N_2	[70]
	200	15	Air	[23]
	450	30	Se	[23]

Table 2.6: Selected annealing conditions for electrodeposited CdS, ZnSe and $CuInSe_2$.

Element	T_m (1 atm) (°C)	T_b (1 atm) (°C)	Vapour pressure (temperatures expressed in °C) 1Pa	10Pa	100 Pa	1kPa	10kPa	100kPa
Cu	1085	2562	1236	1388	1577	1816	2131	2563
In	157	2072	923	1052	1212	1417	1689	2067
Ga	30	2204	1037	1175	1347	1565	1852	2245
S	115	444	102	135	176	235	318	444
Se	221	685	227	279	344	431	540	685
Zn	420	907	337	397	477	579	717	912
Cd	321	767	257	310	381	472	594	767

Table 2.7: Melting temperatures T_m, boiling temperatures T_b and vapour pressures of Cd, Cu, In, Ga, S, Se and Zn [12].

2.5.2 Wet chemical etching

Prior to device fabrication, semiconductor surfaces need to be etched. Tables 2.8 and 2.9 reports the different chemical agents generally used for etching the binary and ternary semiconductors used in this study. This process is used to clean the surfaces from contaminants (like oxides), to remove damaged surface layers, to modify the surface composition of the films and to passivate their surface states. Etchants containing cadmium, zinc or indium salts have also been used with the objective of surface passivation and n-type surface doping of $CuIn_{1-x}Ga_xSe_2$ [105].

Etchant solution	Remarks
1 % bromine in methanol (etchant 1)	Rough surface, depletion of Zn or Cd on polished samples
1 g of $K_2Cr_2O_7$, 10 ml of H_2SO_4, 20 ml of H_2O (etchant 2)	Shiny surface, depletion of Zn or Cd on polished samples
0.5 g of NaOH, 0.5 g of $Na_2S_2O_3$, 100 ml of H_2O (etchant 3)	Shiny surface, nearly stoichiometric surface on polished samples
Etchant 2 followed by etchant 3	Shiny surface, removal of oxides, stoichiometric surface on polished samples
Etchant 1 followed by a wash in hot NaOH solution (80 °C – 90 °C)	Shiny surface, formation of oxides, non-stoichiometric surface on polished samples
1 g of NaOH, 20 ml of H_2O, 1 ml of H_2O_2	Shiny surface, depletion of Se and S on polished samples
Etchant 1 followed by hydrazene-hydrate	Shiny surface on polished samples

Table 2.8: Commonly used etchants for CdS and ZnSe [106].

Etchant solution	Sample	Remarks
$K_2Cr_2O_7$:H_2SO_4 (1:9) saturated	$CuInSe_2$	Homogeneous etching of polished planes; etch pits on cleaved (112), (110) planes
0.5 % – 2 % Br_2:Me(OH)	$CuInSe_2$	Depletion of Cu, In on polished crystals; elemental Se layer on polished crystals
HCl:HNO_3 (1:1)	$CuInSe_2$	Depletion of Cu, In on polished crystals
HF:HNO_3 (1:3)	$CuInSe_2$	Depletion of Cu, In on polished crystals
$HClO_4$ (anodic polarisation)	$CuInSe_2$	Depletion of Cu, In on polished crystals; etch pits on (112) planes
H_2O_2:H_2SO_4:H_2O (1:1:2)	$CuInS_2$	Formation of In_2O_3, S^0 on polished sample
NH_3 bath at 60°C	$Cu(In,Ga)Se_2$	Removal of In-oxide, Se-oxide and Cu_xSe overlayers; depletion of In atoms
XCN (X=Na, K)	$CuB^{III}Ch^{VI}_2$	Removal of Cu-chalcogenide phase and native oxides

Table 2.9: Commonly used etchants for chalcopyrite crystals. Except for $HClO_4$, all etching treatments are without net current flow [13].

2.5.3 Metal contact formation

After all the semiconductor layer deposition and processing steps are completed for a device, it is necessary to provide metal contacts for interconnections with the external circuitry. The properties of the contact depend on the nature of the semiconductor surface, the metal used and particularly on its work function, as already outlined in Section 2.2.3. Table 2.10 displays the value of the work functions of various common metals and Table 2.11 reports the different metals generally deposited on $CuInSe_2$ and summarises the properties of the contacts. One has to refer to the work of Scheer for more information [13].

Metal	Pt	Ni	Au	Cu	Mo	Al	Ag	Ga	In
Work function (eV)	5.65	5.15	5.1	4.65	4.6	4.28	4.26	4.2	4.12

Table 2.10: Values of the work functions for some common metals (eV) [4].

Metal	Type of contact		Remarks
	n-type CIS/metal	p-type CIS/metal	
Pt		Ohmic	Good ohmic contact for Pt on p-type $CuInSe_2$
Ni		Ohmic	Formation of Ni-Se, decomposition of n-$CuInSe_2$ crystal with formation of In-Ni alloy
Au		Usually ohmic	Formation of Au-In alloy
Mo	Ohmic	Ohmic or rectifying	Formation of $MoSe_2$ at the interface
Al		Rectifying	Poor rectification with high leakage current
Ag		Ohmic	Formation of Ag-Se, diffusion of Ag atoms in the crystal
In-Ga	Ohmic	Ohmic	Ohmic contact to p-type CIS after etching in Br_2/methanol
In		Rectifying	Good rectification ($\phi = 0.59$ eV) with no discernable current breakdown, become ohmic after annealing with diffusion of In into the material

Table 2.11: Selected metals used for rectifying and ohmic contacts on $CuInSe_2$ semiconductors of different conductivity types [13].

Note that the electron affinity for $CuInSe_2$ is reported to be 4.6 eV [13]. Therefore, n-type materials will have their work function ranging between 4.6 and 5.1 eV and p-type materials between 5.1 and 5.6 eV. Thus, high work function metals, such as platinum should give rise to an ohmic contact when deposited on p-type $CuInSe_2$ and low work function metal, such as indium would lead to rectifying contact. It has however to be kept in mind that this is only valid in the assumption of the Schottky model, which does not consider the surface states. In addition, as reported in Table 2.11, the metals often react with $CuInSe_2$ to form interfacial alloy compounds, which also affects the properties of the contacts. The surface and interface states can lead to Fermi level pinning and give rise to rectifying contacts. Some metals may also dope the top layers of the semiconductor to form a buried p-n junction.

In this work, the formation of a metal contact was achieved by thermal evaporation. The samples were mounted on mask with holes ranging from 0.5 to 2 mm diameter and metallised in an Edwards metalliser at a pressure below 10^{-6} torr. In thermal evaporation, the source and the substrate are located in an evacuated chamber, as shown in Figure 2.11. The source is a small piece of the metal to be deposited attached to a coil of

tungsten, which serves as the heater. The heated filament with a high melting point remains solid while the source is vaporised. The metal atoms or molecules travel to the substrate where they condense, depositing a metallic layer on the surface of the substrate.

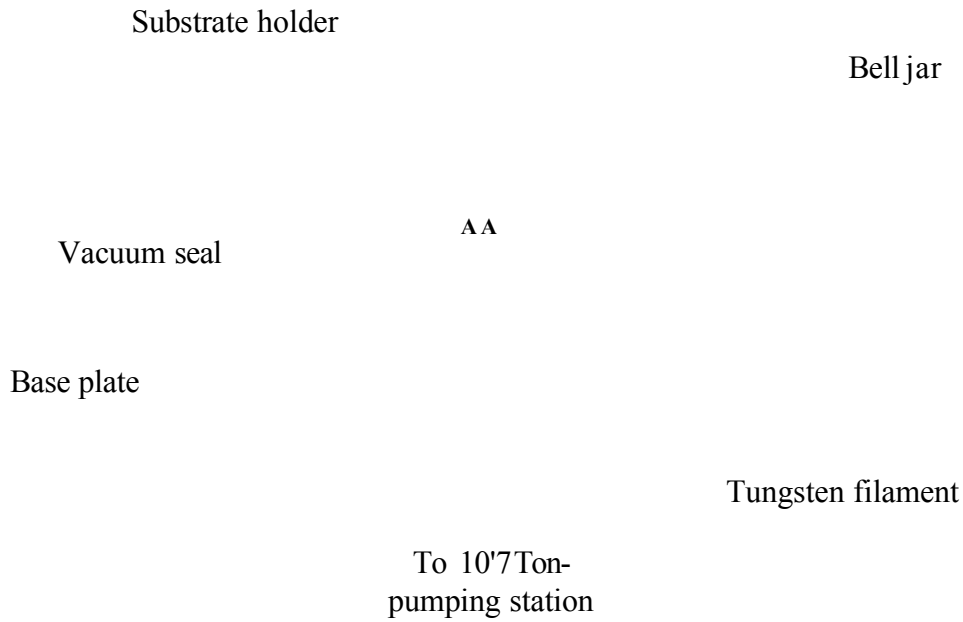

Figure 2.11: Metallisation using thermal evaporation process.

2.6 Advances in $CuInSe_2$-based solar cells

High efficiency solar cell devices have all used heterojunctions between a p-type layer of $CuInSe_2$ or $CuIn_xGa_{i\_x}Se_2$ and an n-type window layer, such as CdS [107], ZnSe [108], ZnO [99] or related compounds [109]. The Mo back contact is generally used in $CuInSe_2$ device structures because of its comparatively low cost and high melting point required in many high temperature growth processes. Transparent conductors, which also function as anti-reflective coatings, have been shown to provide high quality top contacts. The most popular choices are indium-tin oxides (ITO) [98] or suitably doped ZnO [99].

There are two layer deposition sequences possible in the fabrication of $CuInSe_2$-based solar cells, as illustrated in Figure 2.12. One can either grow the $CuInSe_2$ layer on a metal followed by the deposition of the window layer (CdS or ZnSe generally) and the transparent conducting oxide (TCO) layer (Figure 2.12 (a)) or first grow the window

layer on the TCO followed by the deposition of the $CuInSe_2$ layer and the metal contact (Figure 2.12 (b)).

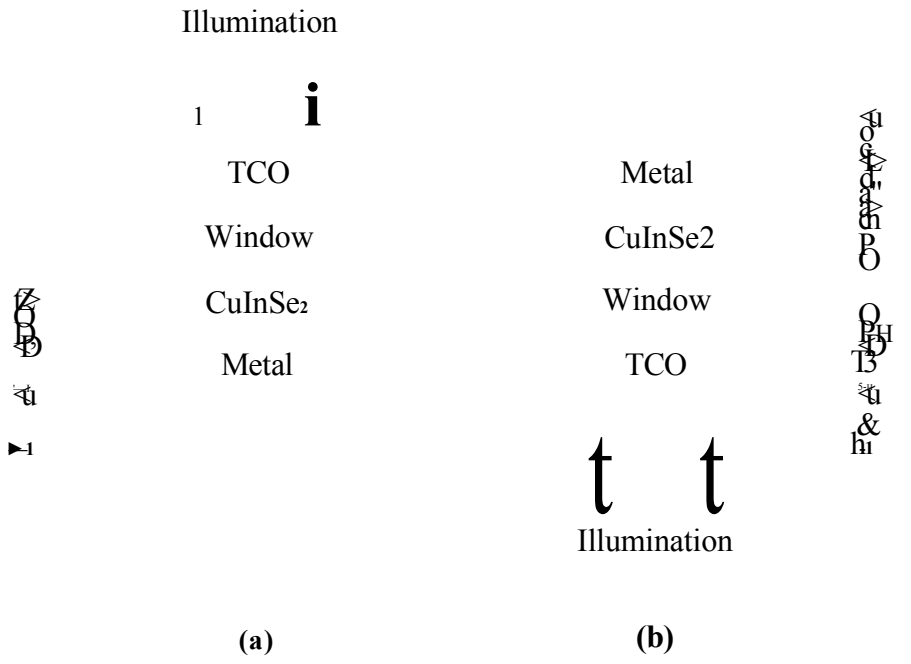

Figure 2.12: Illustration of the two layer deposition sequences followed in $CuInSe_2$-based solar cell fabrication.

Niemegeers et al. [110] demonstrated that the conduction band minimum (CBM) of $CuInSe_2$ should be lower than the CBM of CdS at the interface (Figure 2.13 (a)) for higher efficiency because this design was found to decrease the recombination processes in the depletion region (see Figure 2.13 (b)), therefore increasing the open circuit voltage, V_{oc}, as explained in Section 3.3.1. They showed that the spike at the CdS/$CuInSe_2$ junction was not a barrier to a good efficiency, as the photo-generated electrons could cross it through thermionic emission.

$CuInSe_2$-based solar cells usually achieve optimum performance after air heat treatments at 200°C of the completed device [23].

In the case of CdS/$CuInSe_2$ heterojunction solar cells, the performances are generally limited by a low open circuit voltage (V_{oc}). Addition of gallium into $CuInSe_2$ is generally used to increase the small band gap of $CuInSe_2$ (1.04eV), which is responsible for the low open circuit voltage, as discussed in Section 2.3.2.6. $CuIn_xGa_{i-x}Se_2$ graded band gap structures have also been used in order to further increase the efficiency of the devices [111]. Ga grading can enhance the electric field and therefore allows a higher

carrier collection. Recently, Contreras et al. reported the measurement of 18.8% efficiency for a graded copper indium gallium diselenide (CuInxGai-xSe2) cell [112].

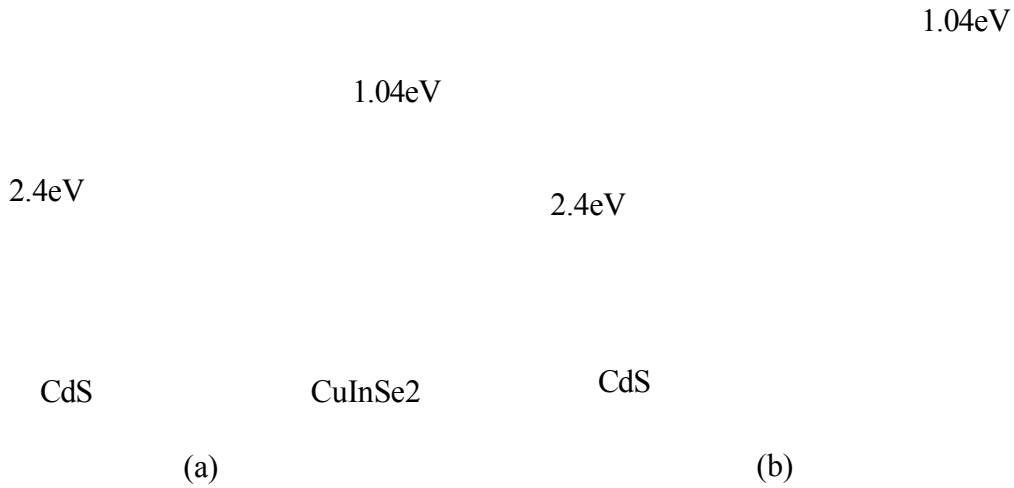

Figure 2.13: Schematic energy band diagram of CdS/CuInSe2 interface (a) when the conduction band minimum (CBM) of CuInSe2 is higher than the CBM of CdS and when the conduction band minimum (CBM) of CuInSe2 is lower than the CBM of CdS.

Tables 2.12 and 2.13 summarise the performances of solar cells based on CuInSe2 and CuInxGai_xSe2, respectively.

Structure	Process	η (%)	J_{sc} ($mA.cm^{-2}$)	V_{oc} (mV)	FF (%)	Area (cm^2)	Ref.
Mo/CIS/CdS/ZnO	Evap + Sel	13.7	38.7	493	72	n.a.	[113]
Mo/CIS/CdS/ZnO:Al	Evap	13.2	36.3	484	75	0.395	[107]
Mo/CIS/CdS/ZnO:Al	Hybrid Sput	11.3	39.8	405	70	0.070	[33]
Mo/CIS/CdS/ZnO:Al	Evap + Sel	10.9	35.4	463	67	0.100	[114]
Mo/CIS/CdS/ZnO/ITO	Evap	10.5	35.6	426	69	0.040	[98]
Mo/CIS/CdS/ZnO	Evap + Sel	10.3	39.0	427	62	n.a.	[99]
Mo/CIS/CdS/ZnO/ZnO:Al	Evap + Sel	10.2	33.6	460	66	0.500	[115]
Mo/CIS/CdS/ZnO:Al	Evap	10.0	n.a.	n.a.	n.a.	n.a.	[96]
Mo/CIS/CdS/ZnO	Sput + Sel	9.9	31.9	438	71	0.431	[116]
Mo/CIS/CdS/ZnO	Elec + Evap + Sel	9.4	35.9	414	63	0.429	[25]
Mo/CIS/OVC/CdS/ZnO:Al	Evap + Sel	8.7	34.4	390	65	0.317	[117]
Mo/CIS/CdS/ZnO	PLD	8.5	36.9	381	60	n.a.	[87]
Mo/CIS/OVC/In_2Se_3/ZnO	Evap	8.5	35.1	423	57	0.200	[78]
Mo/CIS/CdS/i-ZnO/ZnO	Elec + Sel	7.9	32.1	394	62	n.a.	[68]
Mo/CIS/CdS/ZnO:Al	Evap + Sel	6.9	32.8	360	58	0.272	[117]
Au/CIS/CdS/ZnO/ITO	Evap	6.7	32.2	357	58	0.075	[77]
Mo/CIS/CdS/ZnO/ZnO:Al	Elec + Sel	6.5	28.0	350	59	0.100	[23]
Mo/CIS/ZnO/ITO	Evap	6.0	33.5	340	53	0.040	[98]
Mo/CIS/OVC/CdS/ZnO	Flash evap	5.1	29.0	393	44	0.060	[89]
Au/CIS/CdS/ZnO	Bridgman	5.0	28.0	420	41	0.220	[118]
Mo/CIS/CdS/ZnO	MOCVD	n.a.	10.0	260	n.a.	0.050	[82]
Au/CIS/In_2Se_3/ITO	Elec + Sel	3.6	23.7	300	51	0.040	[119]
In/CdS/CIS/SnO_2	CBD	3.1	12.0	365	61	0.100	[93]
SnO_2/CIS/CdS/ZnO:Al	Elec	1.5	31.5	188	n.a.	0.010	[70]

Evap = Evaporation.
Sel = Selenisation.
Sput = Sputtering.
Elec = Electrodeposition.
PLD = Pulsed laser deposition.
SEL = Stacked elemental layer technique.
MOCVD = Metalorganic chemical vapour deposition.
CBD = Chemical bath deposition.
η: Conversion efficiency.
J_{sc}: Short circuit current.
V_{oc}: Open circuit voltage.
FF: Fill factor.

Table 2.12: Review of copper indium diselenide (CIS) thin film solar cell performance.

Structure	Process	η (%)	J_{sc} ($mA.cm^{-2}$)	V_{oc} (mV)	FF (%)	Area (cm^2)	Ref.
Mo/CIGS/CdS/ZnO/ZnO:AlO_3	Evap	18.8	35.2	678	79	0.449	[112]
Mo/CIGS/CdS/ZnO/ITO	Evap	17.6	36.1	649	75	1.000	[120]
Mo/CIGS/CdS/ZnO/ZnO:AlO_3	Evap	16.7	33.0	691	76	n.a.	[27]
Mo/CIGS/CdS/ZnO	Evap	15.9	33.7	648	73	n.a.	[121]
Mo/CIGS/CdS/ZnO/ZnO:Al	Evap	15.9	32.2	650	76	0.430	[122]
Mo/CIGS/In_x(OH, S)$_y$/ZnO	Evap	15.7	n.a.	n.a.	n.a.	n.a.	[123]
Mo/CIGS/CdS/ZnO/ITO	Evap	15.5	35.9	585	74	0.960	[124]
Mo/CIGS/CdS/ZnO	Evap	15.5	32.5	620	77	0.380	[125]
Mo/CIGS/CdS/ZnO	Evap	15.2	33.2	627	73	n.a.	[40]
Mo/CIGS/ZnIn_xSe_y/ZnO	Evap	15.1	30.4	652	76	n.a.	[121]
Mo/CIGS/ZnO/ZnO:AlO_3	Evap	15.0	36.2	604	69	0.462	[112]
Mo/CIGS/CdS/ZnO	Evap	14.9	32.7	621	74	0.100	[105]
Mo/CIGS/ZnO	Evap	14.2	30.8	606	76	0.380	[125]
Mo/CIGS/Zn(O, OH, S)/ZnO	Sput + Sel	14.1	35.2	570	70	3.200	[126]
Mo/CIGS/CdS/ZnO	Elec + Evap + Sel	14.1	29.0	656	74	0.411	[127]
Mo/CIGS/CdS/ZnO:Al	Evap	14.0	35.0	584	68	n.a.	[50]
Mo/CIGS/CdS/ZnO/ZnO:AlO_3	Evap	13.7	32.0	646	66	43.890	[112]
Mo/CIGS/CdS/ZnO/Al	Evap	13.5	32.6	621	67	0.180	[108]
Mo/CIGS/CdS/ZnO:Al	Evap	13.5	35.2	567	68	n.a.	[128]
Mo/CIGS/CdS/ZnO/ITO	Evap	13.2	33.0	563	71	n.a.	[50]
Mo/CIGS/CdS/ZnO	Sput + Sel	13.0	34.6	536	70	0.424	[116]
Mo/CIGS/Zn(O, OH, S)/ZnO	Sput + Sel	12.8	36.5	523	67	3.200	[129]
Mo/CIGS/ZnO	Evap	12.6	33.9	576	64	0.100	[105]
Mo/CIGS/CdS/ZnO:Al	Evap.	12.6	38.2	475	70	0.070	[96]
Mo/CIGS/CdS/ITO	Evap.	11.7	33.7	493	70	0.050	[98]
Mo/CIGS/ZnSe/ZnO/Al	Evap.	11.6	35.2	502	65	0.172	[130]
Mo/CIGS/ZnO:Al	Evap.	11.0	35.8	542	57	n.a.	[50]
Mo/CIGS/Zn(O, OH, S)/ZnO	Sput + Sel	10.7	31.8	550	60	50.000	[126]
Mo/CIGS/CdS/ZnO/ITO	Evap	10.5	26.5	626	63	80.800	[124]
Mo/CIGS/Zn(O, OH)/ZnO	Sput + Sel	9.7	35.5	420	65	0.950	[129]
Mo/CIGS/ZnSe/ZnO/Al	Evap.	9.1	24.6	609	61	0.126	[108]
Mo/CIGS/CdS/ZnO/Ni/Al	Sput + Sel	9.0	34.5	452	58	0.382	[131]
Mo/CIGS/CdS/ZnO/Ni/Al	RTP	6.3	36.5	385	45	0.500	[24]
Mo/CIGS/OVC/CdS/ZnO	Flash evap	5.9	21.4	438	63	n.a.	[89]
Mo/CIGS/CdS/ZnO	Elec + Sel	4.8	25.4	363	52	0.040	[119]

Evap = Evaporation.
Sel = Selenisation.
Sput = Sputtering.
Elec = Electrodeposition.
RTP = Rapid thermal process.
η: Conversion efficiency.
J_{sc}: Short circuit current.
V_{oc}: Open circuit voltage.
FF: Fill factor.

Table 2.13: Review of copper indium gallium diselenide (CIGS) thin film solar cell performance.

2.7 References

[1] Kano K., Semiconductor Devices, Prentice Hall (1998).

[2] Wood D., Optoelectronic Semiconductor Devices, Prentice Hall (1994).

[3] Sze S. M., Physics of Semiconductor Devices, 2nd Edition, Wiley (1981).

[4] Rhoderick E. H., Williams R. H., Metal-Semiconductor Contacts, Clarendon (1988).

[5] Moller H. J., Progress in Materials Science, 35 (1991) 205.

[6] Schottky W., Zeitschrift fur Physik B – Condensed Matter, 113 (1939) 367.

[7] Bardeen J., Physical Review, 71 (1947) 717.

[8] Samantilleke A. P., PhD Thesis, Sheffield Hallam University (1998).

[9] Mc Gregor S. M., PhD Thesis, Sheffield Hallam University (1999).

[10] Chu T. L., Chu S. S., Solid State Electronics, 38 (3) (1995) 533.

[11] Jong W. F. D., General crystallography : a brief compendium, Freeman (1959).

[12] Lide D. R., Handbook of Chemistry and Physics, 79th edition, CRC (1998-1999).

[13] Scheer R., Vacuum Science and Technology, 2 (1997) 77.

[14] Rockett A., Birkmire R. W., Journal of Applied Physics, 70 (7) (1991) R81.

[15] Jayachandran M., Chockalingam M. J., Murali K. R., Lakshmanan A. S., Materials Chemistry and Physic, 34 (1993) 1.

[16] Pottier D., Maurin G., Journal of Applied Electrochemistry, 19 (1989) 361.

[17] Ikari T., Yoshino K., Shimizu T., Fukuyama A., Maeda K., Fons P. J., Yamada A., Niki S., Proceedings of 11th International Conference on Ternary and Multinary Compounds, Institute of Physics Conference Series, 152 (1998) 511.

[18] Vedel J., Thouin L., Lincot D., Journal of Electrochemical Society, 143 (7) (1996) 2173.

[19] Klenk R., Walter T., Schock H. W., Cahen D., Advanced Materials, 5 (2) (1993), 114.

[20] Wei S. H., Zhang S. B., Zunger A., Proceedings of 11th International Conference on Ternary and Multinary Compounds, Institute of Physics Conference Series, 152 (1998) 765.

[21] Schmid D., Ruckh M., Grunwald F., Schock H. W., Journal of Applied Physics, 73 (6) (1993) 2902.

[22] Guillén C., Herrero J., Journal of Electrochemical Society, 141 (1) (1994) 225.

[23] Guillemoles J. F., Cowache P., Lusson A., Fezzaa K., Boisivon F., Vedel J., Lincot D., Journal of Applied Physics, 79 (9) (1996) 7293.

[24] Alberts V., Zweigart S., Schön J. H., Schock H. W., Bucher E., Japanese Journal of Applied Physics, 36 (1997) 5033.

[25] Bhattacharya R. N., Fernandez A. M., Contreras M. A., Keane J., Tennant A. L., Ramanathan K., Tuttle J. R., Noufi R. N., Hermann A. M., Journal of Electrochemical Society, 143 (3) (1996) 854.

[26] Rogacheva E. I., Proceedings of 11th International Conference on Ternary and Multinary Compounds, Institute of Physics Conference Series, 152 (1998) 1.

[27] Dullweber T., Hanna G., Shams-Kohali W., Schwartzlander A., Contreras M. A., Noufi R., Schock H. W., Thin Solid Films, 361 – 362 (2000) 478.

[28] Miyake H., Tsuda M., Sugiyama K., Proceedings of 11th International Conference on Ternary and Multinary Compounds, Institute of Physics Conference Series, 152 (1998) 83.

[29] Durante Rincón C. A., Mora M. T., León M., Proceedings of 11th International Conference on Ternary and Multinary Compounds, Institute of Physics Conference Series, 152 (1998) 123.

[30] Loferski J. J., Journal of Applied Physics, 27 (7) (1956) 777.

[31] Tuttle J. R., Albin D., Matson R. J., Noufi R., Journal of Applied Physics, 66 (9) (1989) 4408.

[32] Guíllen C., Herrero J., Solar Energy Materials and Solar Cells, 43 (1996) 47.

[33] Nakada T., Migita K., Niki S., Kunioka A., Japanese Journal of Applied Physics, 34 (Part 1) (No. 9A) (1995) 4715.

[34] Ramakrishna Reddy K. T., Chalapathy R. B. V., Crystal Research and Technology, 34 (1999) 127.

[35] Negami T., Kohara N., Nishitani M., Wada T., Hirao T., Applied Physics Letters, 67 (6) (1995) 825.

[36] Zaretskaya E. P., Gremenok V. F., Victorov I. A., Bodnar I. V., Rud Y. V., Proceedings of 11th International Conference on Ternary and Multinary Compounds, Institute of Physics Conference Series, 152 (1998) 361.

[37] Schroeder D. J., Hernandez J. L., Rockett A. A., Proceedings of 11th International Conference on Ternary and Multinary Compounds, Institute of Physics Conference Series, 152 (1998) 749.

[38] Yamamoto Y., Yamaguchi T., Demizu Y., Tanaka T., Yoshida A., Thin Solid Films, 281-282 (1996) 372.

[39] Nagoya Y., Kushiya K., Tachiyuki M., Yamase O., Solar Energy Materials and Solar Cells, 67 (2001) 247.

[40] Ruckh M., Schmid D., Kaiser M., Schäffler R., Walter T., Schock H. W., Solar Energy Materials and Solar Cells, 41/42 (1996) 335.

[41] Nelson A. J., Gabor A. M., Contreras M. A., Mason A., Asoka-Kumar P., Lynn K. G., Solar Energy Materials and Solar Cells, 41/42 (1996) 315.

[42] Niles D. W., Al-Jassim M., Ramanathan K., Journal of Vacuum Science and Technology A, 17 (1) (1999) 291.

[43] Heske C., Fink R., Umbach E., Riedl W., Karg F., Applied Physics Letters, 68 (24) (1996), 3431.

[44] Kohara N., Negami T., Nishitani M., Hashimoto Y., Wada T., Applied Physics Letters, 71 (6) (1997) 835.

[45] Contreras M. A., Egaas B., Dippo P., Webb J., Asher S., Swartzlander A., Ramanathan K., Hasoon F. S., Noufi R., Proceedings of 11th International Conference on Ternary and Multinary Compounds, Institute of Physics Conference Series, 152 (1998) 333.

[46] Schroeder D. J., Rockett A. A., Journal of Applied Physics, 82 (10) (1997) 4982.

[47] Wei S. H., Zhang S. B., Zunger A., Journal of Applied Physics, 85 (10) (1999) 7214.

[48] Stanbery B. J., Chang C. H., Anderson T. J., Proceedings of 11th International Conference on Ternary and Multinary Compounds, Institute of Physics Conference Series, 152 (1998) 915.

[49] Klein A., Löher T., Pettenkofer C., Jaergermann W., Journal of Applied Physics, 80 (9) (1996) 5039.

[50] Stolt L., Hedström J., Skarp J., Proceedings of 1st World Conference on Photovoltaic Solar Energy Conversion, Hawaï, USA (1994) 250.

[51] Heske C., Richter G., Chen Z., Fink R., Umbach E., Riedl W., Karg F., Journal of Applied Physics, 82 (5) (1997) 2411.

[52] Lam W. W., Shih I., Solar Energy Materials and Solar Cells, 50 (1998) 111.

[53] Zegadi A., Yakushev M. V., Ahmed E., Pilkington R. D., Hill A. E., Tomlinson R. D., Solar Energy Materials and Solar Cells, 41/42 (1996) 295.

[54] Miyake H., Haginoya T., Sugiyama K., Solar Energy Materials and Solar Cells, 50 (1998) 51.

[55] Sander M., Jaegermann W., Lewerenz H. J., Journal of Physical Chemistry, 96 (2) (1992) 782.

[56] Harris D. C., Exploring Chemical Analysis, 2nd Edition, W. H. Freeman (2001).

[57] Pandey R. K., Sahu S. N., Chandra S., Handbook of Semiconductor Electrodeposition, M. Dekker (1996).

[58] Pourbaix M., Atlas of Electrochemical Equilibria in Aqueous Solutions, Pergamon (1966).

[59] Raffaelle R. P., Forsell H., Potdevin T., Friedfeld R., Mantovani J. G., Bailey S. G., Hubbard S. M., Gordon E. M., Hepp A. F., Solar Energy Materials and Solar Cells, 57 (1999) 167.

[60] Savadogo O., Solar Energy Materials and Solar Cells, 52 (1998) 361.

[61] Vedel J., Proceedings of the 11th International Conference on Ternary and Multinary Compounds, Institute of Physics Conference Series, 152 (1998) 261.

[62] Bhattacharya R. N., Journal of Electrochemical Society, 130 (10) (1983) 2040.

[63] Calixto M. E., Sebastian P. J., Journal of Materials Science, 33 (1998) 339-345.

[64] Fritz H. P., Chatziagorastou P., Thin Solid Films, 247 (1994) 129.

[65] Boumerzoug M., Dao L. H, Journal of Materials Science-Materials in Electronics, 1 (1990) 123-128.

[66] Edamura T., Muto J., Journal of Materials Science-Materials in Electronics, 5 (1994) 275.

[67] Fernández A. M., Advanced Materials for Optics and Electronics, 8 (1998) 1.

[68] Fernandez A. M., Sebastian P. J., Bhattacharya R. N., Noufi R., Contreras M., Hermann A. M., Semiconductor Science and Technology, 11 (1996) 964.

[69] Sasikala G., Moorthy Babu S., Dhanasekaran R., Materials Chemistry and Physics, 42 (1995) 210.

[70] Sudo Y., Endo S., Irie T., Japanese Journal of Applied Physics, 32 (1993) 1562.

[71] Molin A. N., Dikusar A. I., Kiosse G. A., Petrenko P. A., Sokolovsky A. I., Saltanovsky Y. G., Thin Solid Films, 237 (1994) 66.

[72] Molin A. N., Dikusar A. I., Thin Solid Films, 237 (1994) 72.

[73] Stratieva N., Tzvetkova E., Ganchev M., Kochev K., Tomov I., Solar Energy Materials and Solar Cells, 45 (1997) 87.

[74] Nakamura S., Sugawara S., Hashimoto A., Yamamoto A., Solar Energy Materials and Solar Cells, 50 (1998) 25.

[75] Kampmann A., Cowache P., Lincot D., Vedel J., Journal of Electrochemical Society, 146 (1) (1999) 150.

[76] Tzvetkova E., Stratieva N., Ganchev M., Tomov I., Ivanova K., Kochev K., Thin Solid Films, 311 (1997) 101.

[77] Negami T., Nishitani M., Ikeda M., Wada T., Solar Energy Materials and Solar Cells, 35 (1994) 215.

[78] Kwon S. H., Ahn B. T., Kim S. K., Yoon K. H., Song J., Thin Solid Films, 323 (1998) 265.

[79] Hachiuma Y., Ashida A., Yamamoto N., Ito T., Cho Y., Solar Energy Materials and Solar Cells, 35 (1994) 247.

[80] Grindle S. P., Clark A. H., Rezaie-Serej S., Falconer E., McNeily J., Kazmerki L. L., Journal of Applied Physics, 51 (10) (1980) 5464.

[81] Zouaoui A., Lachab M., Hidalgo M. L., Chaffa A., Llinarès C., Kesri N., Thin Solid Films, 339 (1-2) (1999) 10.

[82] Artaud M. C., Ouchen F., Martin L., Duchemin S., Thin Solid Films, 324 (1-2) (1998) 115.

[83] Jones P. A., Jackson A. D., Lickiss P. D., Pilkington R. D., Tomlinson R. D., Thin Solid Films, 238 (1) (1994) 4.

[84] Tanaka T., Tanahashi N., Yamaguchi T., Yoshida A., Solar Energy Materials and Solar Cells, 50 (1998) 13.

[85] Chung Yang L., Xiao H. Z., Rockett A., Shafarman W. N., Birkmire R. W., Solar Energy Materials and Solar Cells, 36 (1995) 445.

[86] Tseng B. H., Rockett A., Lommasson T. C., Yang L. C., Wert C. A., Thornton J. A., Journal of Applied Physics, 67 (5) (1990) 2637.

[87] Schäffler R., Klose M., Brieger M., Dittrich H., Schock H. W., Materials Science Forum, 173-174 (1995) 135.

[88] Sakata H., Ogawa H., Solar Energy Materials and Solar Cells, 63 (2000) 259.

[89] Merino J. M., Leon M., Rueda F., Diaz R., Thin Solid Films, 361-362 (2000) 22.

[90] Ramaiah K. S., Raja V. S., Bhatnagar A. K., Juang F. S., Chang S. J., Su Y. K., Materials Letters, 45 (2000) 251.

[91] Pattabi M., Sebastian P. J., Mathew X., Batthacharya R. N., Solar Energy Materials and Solar Cells, 63 (2000) 315.

[92] Kondo K., Sano H., Sato K., Thin Solid Films, 326 (1998) 83.

[93] Vidyadharan Pillai P. K., Vijayakumar K. P., Solar Energy Materials and Solar Cells, 51 (1998) 47.

[94] Firoz Hasan S. M., Subhan M. A., Mannan K. M., Optical Materials, 14 (2000) 329.

[95] Kundu S. N., Bhattachryya D., Chaudhuri S., Pal A. K., Materials Chemistry and Physics, 57 (1999) 207.

[96] Nakada T., Onishi R., Kunioka A., Solar Energy Materials and Solar Cells, 35 (1994) 209.

[97] Terauchi M., Negami T., Nishitani M., Ikeda M., Wada H., Wada T., Solar Energy Materials and Solar Cells, 35 (1994) 121.

[98] Nishitani M., Ikeda M., Negami T., Kohoki S., Kohara N., Terauchi M., Wada H., Wada T., Solar Energy Materials and Solar Cells, 35 (1994) 203.

[99] Kushiya K., Hakuma H., Sano H., Yamada A., Konagai M., Solar Energy Materials and Solar Cells, 35 (1994) 223.

[100] Suzuki R., Ohdaira T., Ishibashi S., Uedono A., Niki S., Fons P. J., Yamada A., Mikado T., Yamazaki T., Tanigawa S., Proceedings of 11th International Conference on Ternary and Multinary Compounds, Institute of Physics Conference Series, 152 (1998) 757.

[101] Hariskos D., Bilger G., Braunger D., Ruckh M., Schock H. W., Proceedings of 11th International Conference on Ternary and Multinary Compounds, Institute of Physics Conference Series, 152 (1998) 707.

[102] Dirnstorfer I., Burkhardt W., Kriegseis W., Osterreicher I., Alves H., Hofmann D. M., Ka O., Polity A., Meyer B. K., Braunger D., Thin Solid Films, 361-362 (2000) 400

[103] Mc Gregor S. M., Dharmadasa I. M., Wadswoorth I., Care C. M., Optical Materials, 6 (1996) 75.

[104] Samantilleke A. P., Boyle M. H., Young J., Dharmadasa I. M., Journal of Materials Science: Materials in Electronics, 9 (1998) 231.

[105] Canava B., Guillemoles J. F., Yousfi E. B., Cowache P., Kerber H., Loeffl A., Schock W. H., Powalla M., Hariskos D., Lincot D., Thin Solid Films, 361-362 (2000) 187.

[106] Dharmadasa I. M., Blomfield C. J., Gregory G. E., Young J., International Journal of Electronics, 76 (5) (1994) 961.

[107] Chen W. S., Stewart J. M., Devaney W. E., Mickelsen R. A., Stanbery B. J., Conference Record of the 23rd IEEE Photovoltaic Specialists Conference (1993) 364.

[108] Kushiya K., Ohtake Y., Yamada A., Konagai M., Japanese Journal of Applied Physics, 33 (1994) 6599.

[109] Hassan G. E., Ramadan M. R. I., El-Labani H., Badawi M. H., Aboul-Enein S., Carter M. J., Hill R., Semiconductor Science and Technology, 9 (1994) 1261.

[110] Niemegeers A., Burgelman M., Vos A. D., Applied Physics Letters, 67 (6) (1995) 843.

[111] Kushiya K., Tachiyuki M., Kase T., Sugiyama I., Nagoya Y., Okumura D., Sato M., Yamase O., Takeshita H., Solar Energy Materials and Solar Cells, 49 (1997) 177

[112] Contreras M. A., Egaas B., Ramanathan K., Hiltner J., Swartzlander A., Hasoon F., Noufi R., Progress in Photovoltaic Research and Applications, 7 (1999) 311.

[113] Zweigart S., Schmid D., Kessler J., Dittrich H., Schock H. W., Journal of Crystal Growth, 146 (1995), 233.

[114] Arya R. R., Lommasson T. C., Wiedeman S., Russel L., Skibo S., Fogelboch J., Conference Record of the 23rd IEEE Photovoltaic Specialists Conference (1993) 516.

[115] Alberts V., Zweigart S., Schock H. W., Semiconductor Science and Technology, 12 (1997) 217.

[116] Beck M. E., Swartzlander-Guest A., Matson R., Keane J., Noufi R., Solar Energy Materials and Solar Cells, 64 (2000) 135.

[117] Okano Y., Nakada T., Kunioka A., Solar Energy Materials and Solar Cells, 50 (1998) 105.

[118] Shukri Z. A., Yip L. S., Qiu C. X., Shih I., Champness C. H., Solar Energy Materials and Solar Cells, 37 (1995) 395.

[119] Kampmann A., Sittinger V., Rechid J., Reineke-Koch R., Thin Solid Films, 361-362 (2000) 309.

[120] Wada T., Proceedings of the 11th International Conference on Ternary and Multinary Compounds, Institute of Physics Conference Series, 152 (1998) 903.

[121] Ohtake Y., Okamoto T., Yamada A., Konagai M., Saito K., Solar Energy Materials and Solar Cells, 49 (1997) 269.

[122] Tuttle J. R., Albin D. S., Tennant A., Gabor A. M., Contreras M., Noufi R., Solar Energy Materials and Solar Cells, 35 (1994) 193.

[123] Hariskos D., Ruckh M., Rühle U., Walter T., Schock H. W., Hedström J., Stolt L., Solar Energy Materials and Solar Cells, 41/42 (1996) 345.

[124] Negami T., Satoh T., Hashimoto Y., Nishiwaki S., Shimakawa S., Hayashi S., Solar Energy Materials and Solar Cells, 67 (2001) 1.

[125] Walter T., Braunger D., Dittrich H., Köble C., Herberholz R., Schock H. W., Solar Energy Materials and Solar Cells, 41/42 (1996) 355.

[126] Cooray N. F., Kushiya K., Fujimaki A., Sugiyama I., Miura T., Okumura D., Sato M., Ooshita M., Yamase O., Solar Energy Materials and Solar Cells, 49 (1997) 291.

[127] Bhattacharya R. N., Batchelor W., Wiesner H., Hasoon F., Granata J. E., Ramanathan K., Alleman J., Keane J., Mason A., Matson R. J., Noufi R. N., Journal of Electrochemical Society, 145 (10) (1998) 3435.

[128] Nakada T., Ohbo H., Fukuda M., Kunioka A., Solar Energy Materials and Solar Cells, 49 (1997) 261.

[129] Kushiya K., Nh T., Sugiyama I., Sato Y., Inamori Y., Takeshita H., Japanese Journal of Applied Physics, 35 (Part 1) (No8) (1996) 4383.

[130] Ohtake Y., Kushiya K., Ichikawa M., Yamada A., Konagai M., Japanese Journal of Applied Physics, 34 (Part 1) (Number 12A) (1995) 5949.

[131] Dhere N. G., Lynn K. W., Solar Energy Materials and Solar Cells, 41/42 (1996) 271.

Chapter 3: Characterisation techniques

3.1 Introduction

This chapter describes the twelve techniques used to study the $CuInSe_2$-based photovoltaic solar cells from the material layers to the completed devices. These techniques can be divided into two categories.

- The material characterisation techniques, which give the details on the structure, morphology, composition, optical and electrical properties of the deposited layers and therefore help understanding and optimising the thin film growth.
- The device characterisation techniques, which allow the assessment of the completed solar cells and, combined with the material characterisation results, provide useful information for further improvements of the different processes involved in the development of thin film devices.

Section 3.2 describes the techniques for characterising the materials, including x-ray diffraction (XRD), Raman spectroscopy, scanning electron microscopy (SEM), atomic force microscopy (AFM), x-ray fluorescence (XRF), inductively coupled plasma (ICP) spectroscopy, x-ray photoelectron spectroscopy (XPS), glow discharge optical emission spectroscopy (GDOES), optical absorption and photoelectrochemical (PEC) measurements. The techniques for characterising the completed devices, including current-voltage (I-V) and capacitance-voltage (C-V) measurements, will be discussed in Section 3.3.

It is useful to recall that the technique of electrodeposition employed to grow the material has already been described in Section 2.4.1.1.

3.2 Material characterisation

The semi-conducting layers were characterised to investigate their crystallinity, morphology, composition, optical and electrical properties. Thus, the structure of the layers were characterised by XRD and Raman spectroscopy. The morphology was studied by SEM and AFM. The elemental analysis was performed using XRF, ICP spectroscopy, XPS and GDOES. The optical properties were studied by optical absorption. Finally the conductivity type was determined using PEC measurements.

3.2.1 X-ray diffraction (XRD)

X-ray diffraction is a versatile, non-destructive analytical technique for identification of the various crystalline compounds present in powdered and solid samples [1]. The technique of XRD is based on Bragg's law

$$nk - 2d \sin 6 \qquad (3.1)$$

where n is the order of diffraction, k is the wavelength of the x-rays, d is the distance between two neighbouring planes, 6 is the angle between the incident x-ray and the crystalline plane (in radians).

X-ray beam Diffracted beam

Atomic plain

Atomic plam

Figure 3.1: Schematic diagram of the x-ray diffraction by a crystal lattice.

As shown in Figure 3.1, when a monochromatic x-ray beam of wavelength k is incident on the lattice planes of a crystal at an angle 6, diffraction occurs only when the distance travelled by the rays reflected from successive planes differs by a complete number n of wavelengths. In polycrystalline materials, several d-values satisfy Bragg's law by varying the angle 6.

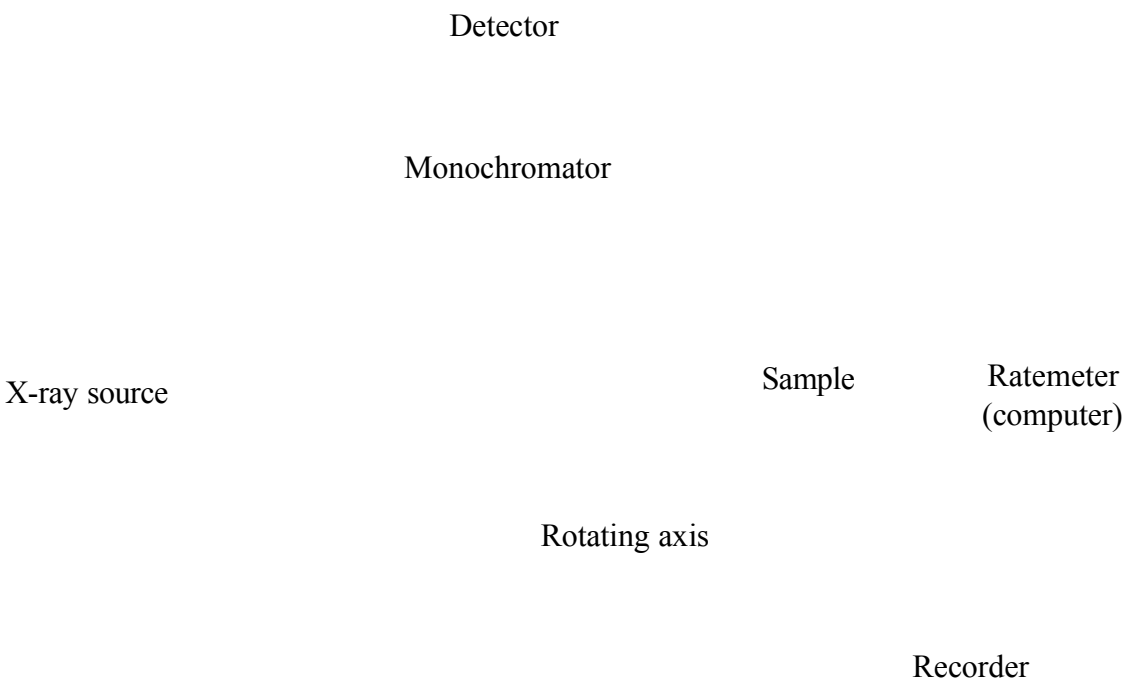

Figure 3.2: Schematic of the X-ray Powder Diffractometer.

X-ray diffraction analysis was carried out on a PW 1710 Philips Powder Diffractometer, as schematically shown in Figure 3.2. The x-ray source provides a polychromatic radiation produced from a copper target source. The monochromator positioned in front of the detector is timed to select only the CuKa emission line from the source. The system can then be viewed as operating with a monochromatic source whose wavelength is 1.5406 A. The sample is rotated around an axis, as shown in Figure 3.2. As the scanning proceeds, the detector is rotated around the same axis to detect the diffracted beam. The instrument is fully computer-controlled via the software PC-APD. The x-rays detected from the sample surface have been diffracted by families of planes, according to Bragg's law. The result of XRD measurements is a difffactogram, which is a plot of the

intensity (number of counts) versus the angle. The different phases in the crystal (from peak positions), phase concentrations (from peak heights), crystallite sizes (from peak widths) and amorphous content (from background hump) can be deduced from a diffractogram.

The traditional measure of crystallite size is based on the Scherrer equation:

$$*m = \text{Q-94}\frac{}{B(29)\,\hat{}\,cos\,9} \quad (3.2)$$

where $thkl$ is the crystallite size in the direction normal to the diffracting plane (hkl), A is the x-ray wavelength, $B(9)$ is the full width at half maximum (FWHM) of the peak (radians) and 6 is the Bragg angle (radians). It is important to mention that instrumental broadening and micro-strain can contribute to peak broadening [2].

3.2.2 Raman spectroscopy

Raman spectroscopy is based on inelastic light scattering by molecules in organic samples or phonons in crystals [3].

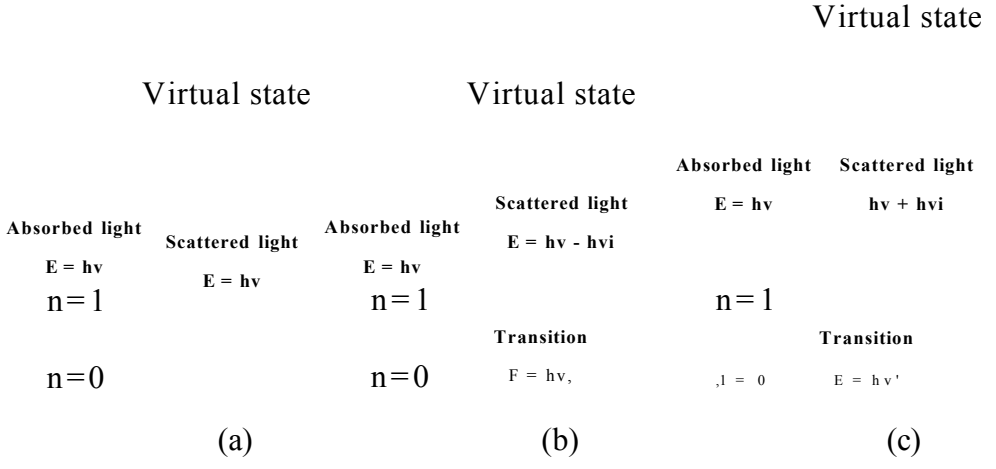

Figure 3.3: Origin of (a) Rayleigh, (b) Stokes and (c) anti-Stokes scattering.

A laser is used to illuminate the specimen of interest. The vibrations of the molecules or the phonons have characteristic frequencies. The light scattered back from these

molecules or phonons is shifted in frequency by amounts specific to each type of molecule or phonon.

As described in Figure 3.3, two processes are possible. The incident photon either gains energy (anti-Stokes scattering) or looses energy (Stokes scattering). In a crystal, this principle brings into play the annihilation of a phonon (anti-Stokes scattering) or creation of a phonon (Stokes scattering). The scattered light is then separated by a grating into the individual spectral lines as a function of wavelength and registered by a charged coupled device (CCD) detector. The grating is mounted on a rotary stage whose position can be changed by the computer so that all the frequencies can be scanned.

Raman measurements of $CuInSe_2$ layers were performed using a Renishaw Raman Microprobe (780 nm line). ZnSe and CdS samples were sent to Warsaw University of Technology and studied using a triple XY-800 DILOR spectrometer with multichannel detection (CCD camera) (514.5 nm line).

3.2.3 Scanning electron microscopy (SEM)

SEM is a non-destructive technique used to study the morphology of solid samples. The main components of the instrument are shown to the left in Figure 3.4, while the optical system is shown schematically to the right.

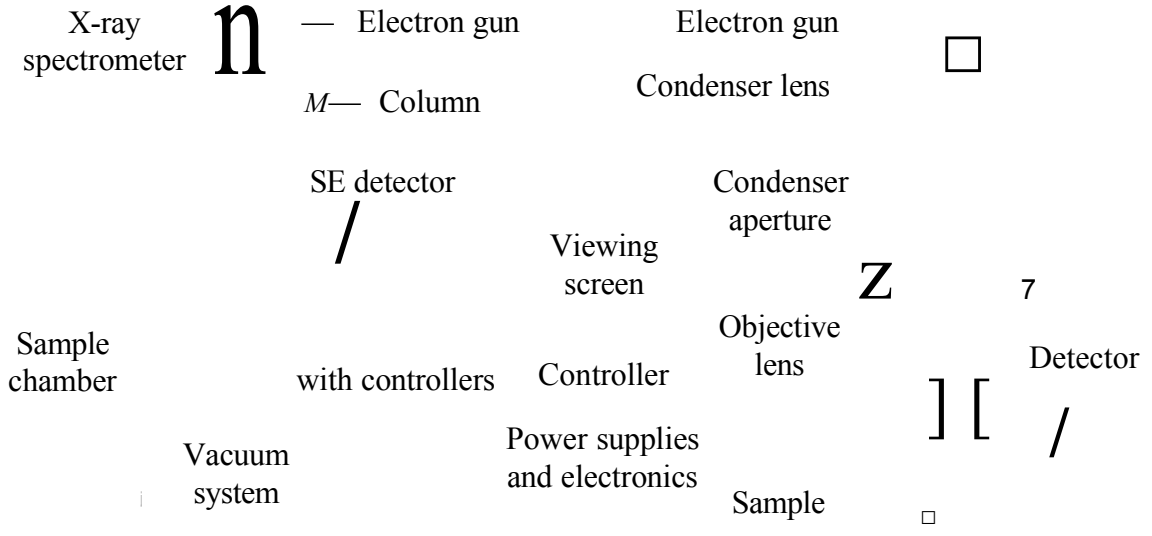

Figure 3.4: Main components of an SEM with its optical system.

An electron beam is generated by an electron gun at the top of the column. This beam is focused by two magnetic lenses and deflected by two scanning coils before hitting the sample in a very small spot. To avoid undue scattering and absorption of the electrons, the column and sample chamber is operated under vacuum. When the electrons penetrate into the sample, several processes take place as they are being absorbed. Some are reflected (back scattered electrons, BSE) out of the sample and are collected by a suitable detector. These electrons can be used to obtain information on the mean atomic number in the part of the sample from which they originate. Secondary electrons (SE), with very low energy, are also released from the sample from an area close to the spot where the primary electrons enter. Collected by a suitable detector, these are used to obtain information on the topography of the sample. Thus, this signal is used to modulate the intensity on a viewing screen, which is scanned synchronously with the primary beam in the column. Thereby, an image is generated on the viewing screen with high brightness in areas with a strong signal from the detector, and darker areas where weak signals are detected. To select an area for investigation, the sample is mounted on a special stage, which allows translation, tilt and rotation of the sample. This stage can be controlled from outside the vacuum chamber. An energy dispersive x-ray (EDX) spectrometer is also mounted within the equipment. When an electron hits an atom in the sample with sufficient energy, x-rays might be generated. Some of these x-rays leave the sample and might be analysed by this spectrometer. From the x-rays, the atomic composition of the sample can be obtained [4].

The equipment used for analytical scanning electron microscopy was a Phillips XL40 series ASEM with a Link eXL EDX.

3.2.4 Atomic force microscopy (AFM)

Atomic force microscopy is a non-destructive three-dimensional imaging technique. AFM can be used to study electrical conductors and semiconductors as well as insulators [5]. The main components of an AFM, displayed in Figure 3.5, are a tip (generally made from Si_3N_4 or Si) extended down from the end of a reflective cantilever, a diode laser focused onto the back of a reflective cantilever and a segmented photo-detector. The tip is brought very close to the surface of the sample to be studied such that it experiences very small interaction forces. The forces are governed by the interaction potentials

between atoms. The interaction is attractive at large distances due to the Van der Waals interaction. At short distances the repulsive forces have their origin in the quantum mechanical exclusion principle. Consequently, two different modes of imaging in AFM are possible.

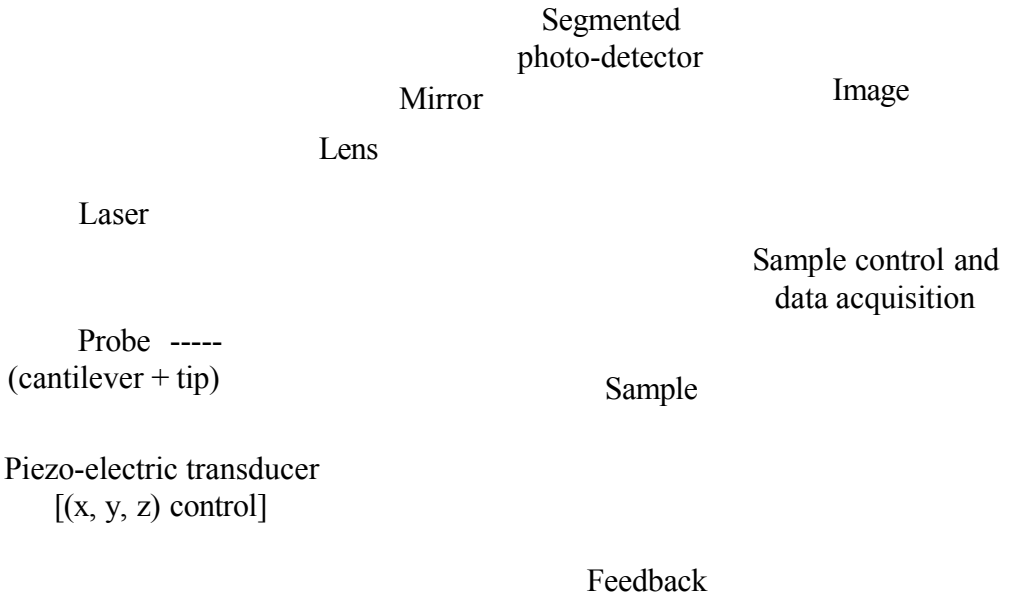

Figure 3.5: Sketch of an atomic force microscope.

The basic mode of operation is known as the contact mode, in which the tip is held a few angstroms above the surface. The surface and the tip interact by repulsive forces. As the tip scans the surface of the sample, moving up and down with the contour of the surface, the laser beam is deflected off the attached cantilever into a dual element photodiode. The photo-detector measures the difference in light intensities between the upper and lower photo-detectors, and then converts to voltage. Feedback from the photodiode difference signal, through software control from the computer, enables the tip to maintain either a constant force or constant height above the sample. In the constant force mode the piezo-electric transducer monitors real time height deviation. In the constant height mode the deflection force on the sample is recorded. The alternative method of measurement is known as the non-contact mode, which is used in situations where tip contact might alter the sample in subtle ways. In this mode, the tip hovers 50-150 Angstrom above the sample surface. Attractive Van der Waals forces acting between the tip and the sample are detected and topographic images are constructed by

scanning the tip above the surface. Unfortunately the attractive forces from the sample are substantially weaker than the forces used in contact mode. Consequently, the tip must be given a small oscillation so that AC detection methods can be used to detect the small forces between the tip and the sample by measuring the change in amplitude, phase, or frequency of the oscillating cantilever in response to force gradients from the sample.

The AFM measurements were made in contact mode using a SPM 9500 J at the Materials Research Laboratory – Institute of Physics and Electronics at Bhopal University in India.

3.2.5 X-ray fluorescence (XRF)

X-ray fluorescence (XRF) is a non-destructive analytical technique used to identify and determine the concentrations of the elements present in a solid, powdered or liquid sample [5]. When sample atoms are irradiated with high-energy primary x-ray photons, electrons are ejected in the form of photoelectrons. This creates electron vacancies in one or more of the orbitals, converting the atoms into ions, which are unstable. Electrons from outer orbitals fill the vacancies in inner orbitals to restore the atoms to a more stable state. Such transitions may be accompanied by an energy emission in the form of a secondary x-ray photon, a phenomenon known as fluorescence. The energy of the emitted fluorescent photons is determined by the difference in energy between the initial and final orbitals of the individual transitions. The wavelength of the fluorescent photons is related to the atomic number Z of the elements present in the studied sample. In addition, the intensity of emission, i.e., the number of photons, is proportional to the concentration of the responsible element in the sample.

As can be seen in the sketch of the x-ray fluorescence spectrometer, displayed in Figure 3.6, an analysing crystal is used to separate the various wavelengths by diffraction. Finally a detector based on an ionisation effect similar to that described under sample excitation, converts the photon energies into measurable voltage pulses. All x-ray fluorescence analyses were carried out on a Philips PW2400 x-ray fluorescence spectrometer.

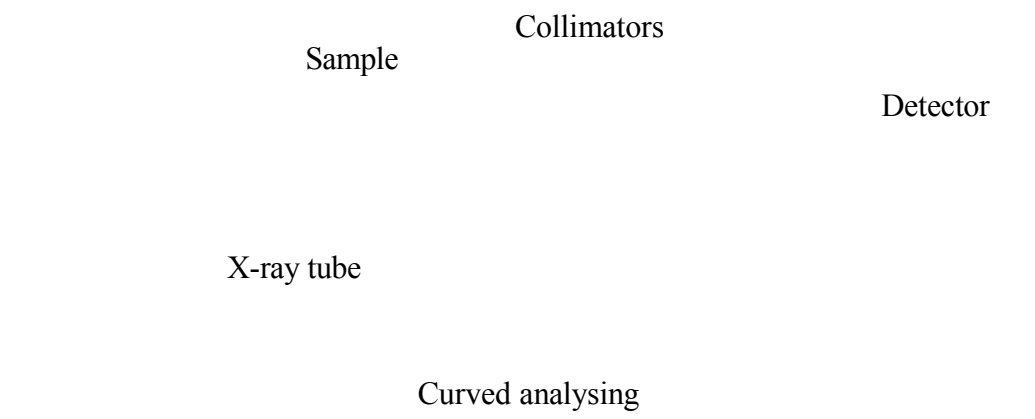

Figure 3.6: Layout of a wavelength dispersive x-ray fluorescence spectrometer.

3.2.6 Inductively coupled plasma (ICP) spectroscopy

Inductively coupled plasma (ICP) spectroscopy has become one of the most widely used technique for elemental analysis at the trace, minor and major level [5]. As shown in Figure 3.7, the experimental arrangement for plasma production consists of three concentric quartz tubes through which argon flows.

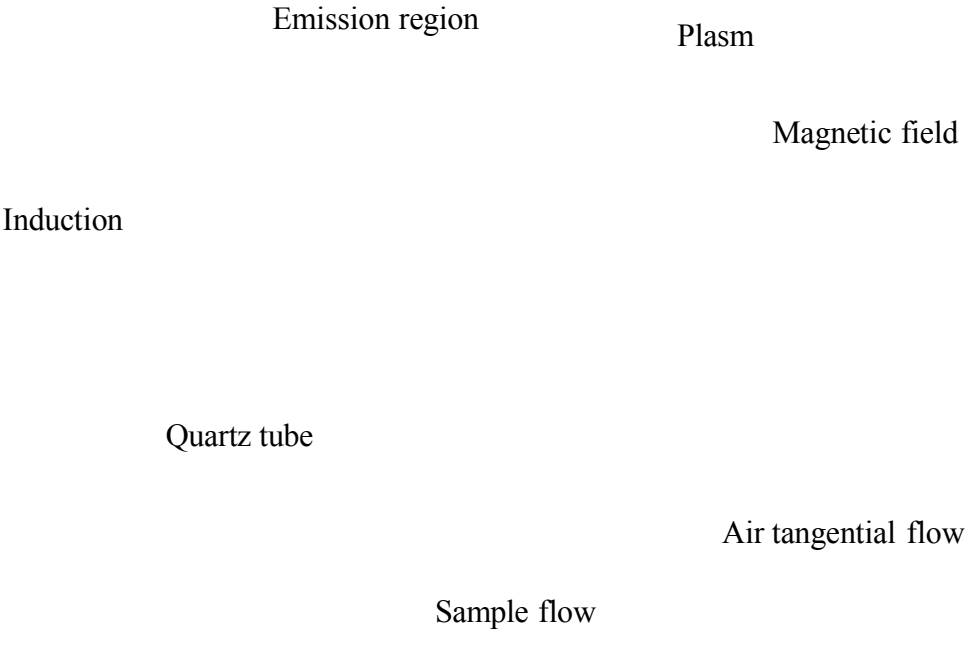

Figure 3.7: Schematic cross section of an ICP torch [6].

A water-cooled induction coil powered by a radio-frequency generator surrounds the top end of the outside tube. A spark from a Tesla coil initiates ionisation of the flowing argon. The resulting ions and their associated electrons quickly interact with the fluctuating magnetic field produced by the induction coil and gain sufficient energy to ionise more argon atoms by collisional excitation and intense thermal energy. A flame-shaped plasma forms near the top of the torch. The high temperatures (6000 – 10000 K) produced by the plasma generally require a second stream of gas, generally argon, to cool the inside quartz wall of the torch. The argon, which flows tangentially around the walls of the tubes, as indicated by the arrows in Figure 3.7, also serves to centre and stabilise the plasma. Samples are nebulised to form a fine aerosol mist and then injected through the centre of the ICP by a stream of argon. The high temperature environment dissociates the sample into individual atoms and ions, which are then excited.
Two kinds of ICP spectrometers can be used for elemental analysis:

- Inductively coupled plasma atomic emission spectroscopy (ICPAES) uses quantitative measurements of the optical emission from excited atoms in the same way as for GDOES (see section 3.2.8). The light emitted by the elements is separated by the spectrometer (Figure 3.13 in section 3.2.8) into the individual spectral lines as a function of the wavelength and registered by photomultipliers.
- Inductively coupled plasma mass spectroscopy (ICPMS) uses the analysis of the ions present in the plasma through their mass to charge ratio (m/z) values. The separation of ions can be achieved in a number of ways. In a quadrupole mass analyser, only electric fields are used to separate ions according to their m/z values.

A quadrupole (see Figure 3.8) consists of four parallel rods or poles through which the ions being separated are passed. The poles have a fixed DC and alternating RF voltages applied to them. Depending on the produced electric field, only ions of a particular m/z will be focused on the detector, all the other ions will be deflected into the rods. By varying the amplitude and frequency of the electric field, different ions will be detected and a mass spectrum will be obtained.

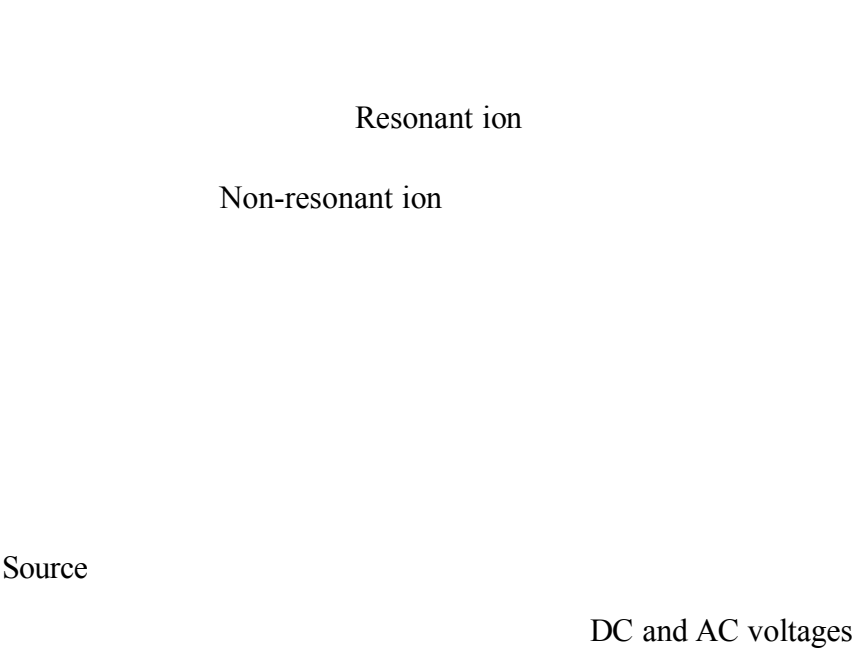

Figure 3.8: Schematic diagram of a quadrupole mass analyser [6].

Both SPECTRO MODEL P ICPOES and AGILENT 4500 SERIES ICP/MS were used for composition analysis. However, ICPMS gave more complete and accurate results than ICPAES. So it was decided to concentrate only on ICPMS for this work.

3.2.7 X-ray photoelectron spectroscopy (XPS)

X-ray photoelectron spectroscopy is a non-destructive ultra high vacuum (UHV) technique used for surface elemental analysis [7]. It is based on the absorption of a photon by an atom in the specimen of interest, leading to the emission of a core electron (see Figure 3.9). The kinetic energy (KE) of the emitted photoelectron can be measured using an appropriate energy analyser and a photoelectron spectrum can thus be recorded. The binding energy BE of the electron is given by the Einstein relation

$$BE = h\,o - KE \tag{3.3}$$

where hu is the energy of the incident photon.

Generally, an XPS spectrum is a plot of the number of photoelectrons detected as a function of the binding energy. From the observed peaks, it is possible to identify all the elements present at the surface of the samples and obtain their respective concentration. Other peaks will also appear in the spectrum due to Auger emission, which is a two-electron process following the emission of the core electron, as depicted in Figure 3.9.

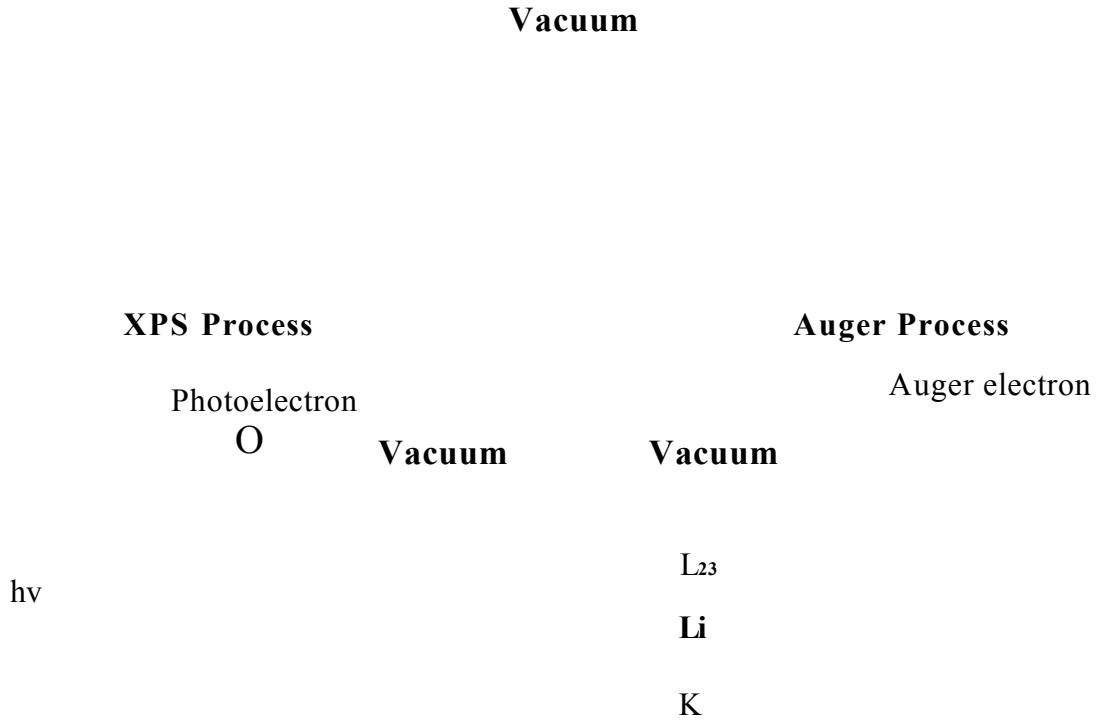

Figure 3.9: Processes involved in XPS and AES.

The VG ESCALAB II instrument used for XPS analysis is sketched in Figure 3.10. In this system, the samples are introduced via a locked chamber connected to the transfer chamber in order to maintain vacuum and are subsequently transferred to the XPS analysis chamber by a combination of railway tracks and wobblesticks. The x-ray source is either an aluminium or magnesium anode. The advantages of having both AlKa or MgKa radiations are not only to differentiate between the photoelectron and Auger peaks in the spectrum, but also to resolve photoelectron and Auger peaks, which may otherwise interfere with each other. As a matter of fact, the Auger electron energy is independent of the x-ray energy, whereas the photoelectron energy is related to the x-ray energy via the Einstein equation. The photoelectrons emitted from the specimen are

dispersed according to their energies by a spherical sector electrostatic analyser. Then, they are made to enter an electron multiplier, which is used as a pulse counting detector.

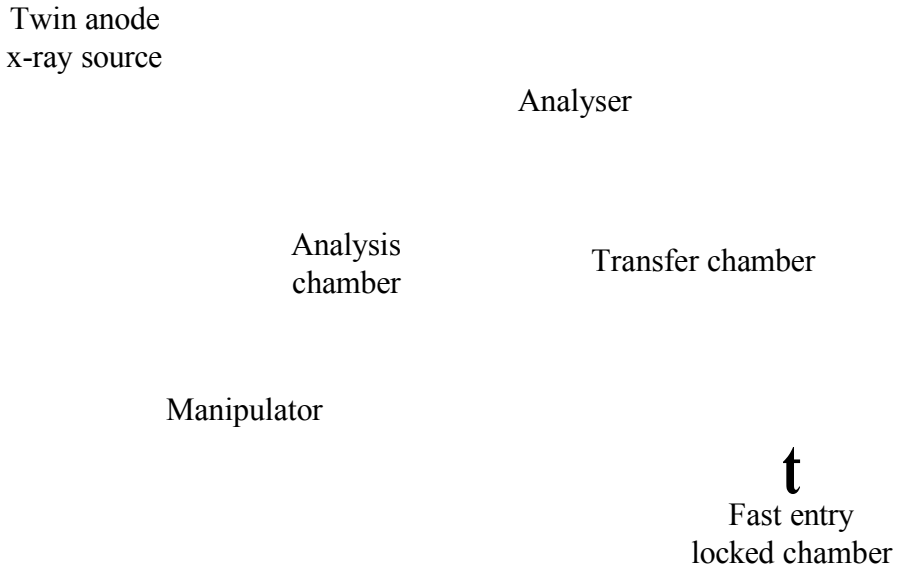

Figure 3.10: Schematic of the VG microlab XPS.

3.2.8 Glow Discharge Optical Emission Spectroscopy (GDOES)

Glow Discharge Optical Emission Spectroscopy (GDOES) is used for qualitative or quantitative determination of elemental composition and allows depth profile analysis of solid samples [8]. The main components of the instrument are the glow discharge source and the spectrometer.

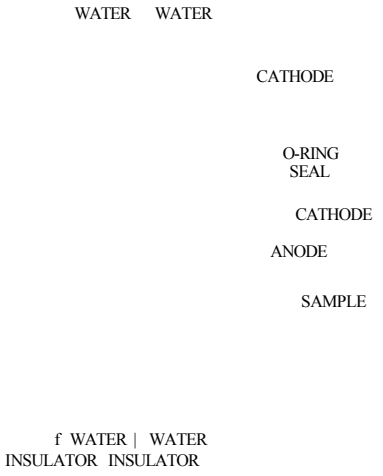

Figure 3.11: Mechanical design of the glow discharge plasma source.

Figure 3.11 shows a section through the mechanical structure of the glow discharge plasma source. It consists of a cathode and an anode, which are electrically isolated from one another by means of insulating disks. The electrodes are cooled by circulating water in order to create thermally stable conditions necessary for the constancy of the sputter rate. The sample has electrical and thermal contact with the cathode plate. A plasma made of argon ions is generated into the evacuated anode space. These ions are accelerated towards the cathode by applying a high voltage between the two electrodes (see Figure 3.12). Excited surface atoms removed from the sputtering process diffuse into the plasma where they relax by emitting photons of characteristic wavelengths.

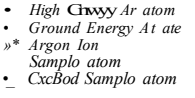

Figure 3.12: Cathode sputtering process.

The light emitted by the elements is separated by the spectrometer (Figure 3.13) into the individual spectral lines as a function of the wavelength and registered by photomultipliers. The intensity of the individual spectral lines is directly proportional to the concentration of the elements sputtered from the sample. Operating parameters, such as high voltage, vacuum from glow discharge source and spectrometer tank are monitored via analysis software developed by LECO. This software also processes the signals supplied from the photomultipliers and the results of analysis in numerical and graphic form.

All the GDOES profile analyses were carried out on a LECO GDS-750 QDP glow discharge spectrometer.

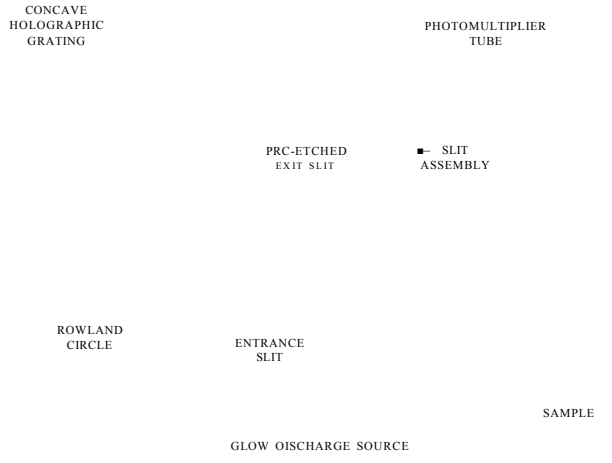

Figure 3.13: Basic design of the glow discharge spectrometer.

3.2.9 Optical absorption spectroscopy

Optical absorption spectroscopy is an important technique in chemistry, as it is an easy way to identify a large variety of inorganic and organic species [5]. This technique is also useful to determine the band gap of a semiconductor from its optical absorption spectrum using

$$hv \tag{3.4}$$

where A is the absorbance, a is the absorption coefficient, t is the thickness of the sample, C is a constant depending on the refractive index of the semiconductor, hv is the energy of the absorbed light and Eg is the band gap of the semiconductor of interest [9]. This equation applies only to direct energy gap materials.

The absorption spectrum of a sample is a plot of the absorbance versus the wavelength of the radiation, the absorbance A being a function of the intensity of the incident light 70 and the transmitted light I

$$\left(\frac{I}{I_0}\right) \tag{3.5}$$

The optical absorption measurements of wide band gap semiconductors, such as CdS and ZnSe can be done using UV-visible spectroscopy, whereas low band gap materials, such as $CuInSe_2$, which absorb radiation in the near infrared, have to be studied by infrared spectroscopy.

3.2.9.1 UV-visible spectroscopy

The main components of a UV-visible spectrometer, which is based on a continuous wave spectrometer, are shown in Figure 3.14.

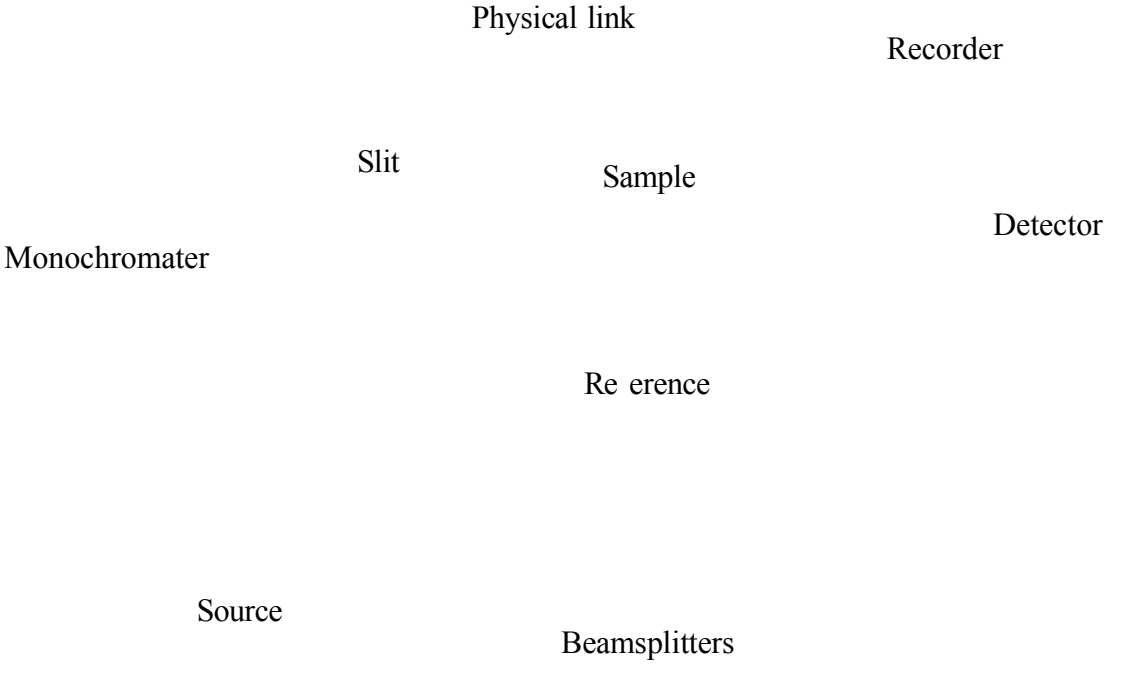

Figure 3.14: Schematic of a continuous wave spectrometer.

A deuterium arc for the UV and a quartz halogen lamp for the visible, selected by a computer-controlled selector mirror generate light across the spectrum of interest. The monochromater (diffraction grating) disperses the light into the complete spectrum. The desired wavelength is selected by a slit. A beam splitter separates the incident beam into two: half goes to the sample and half to the reference, which is the substrate for our samples. The sample absorbs the light according to its chemical properties. A detector collects the radiation that passes through the sample and compares its energy to that going through the reference. The detector gives an electrical signal, which is normally

sent directly to an analog recorder. A link between the monochromater and the recorder allows recording energy as a function of frequency or wavelength, depending on how the recorder is calibrated. The instrument must be repetitively calibrated, because the analog connection between the monochromater position and the recording device is subject to misalignment and wear.

The equipment used in these measurements was a UNICAM model UV2 UV-visible spectrophotometer.

3.2.9.2 Infrared spectroscopy

A Nicolet model MAGNA-IR 860 FTIR spectrometer was used for all the measurements of low band gap materials. Figure 3.15 illustrates the design of the spectrometer.

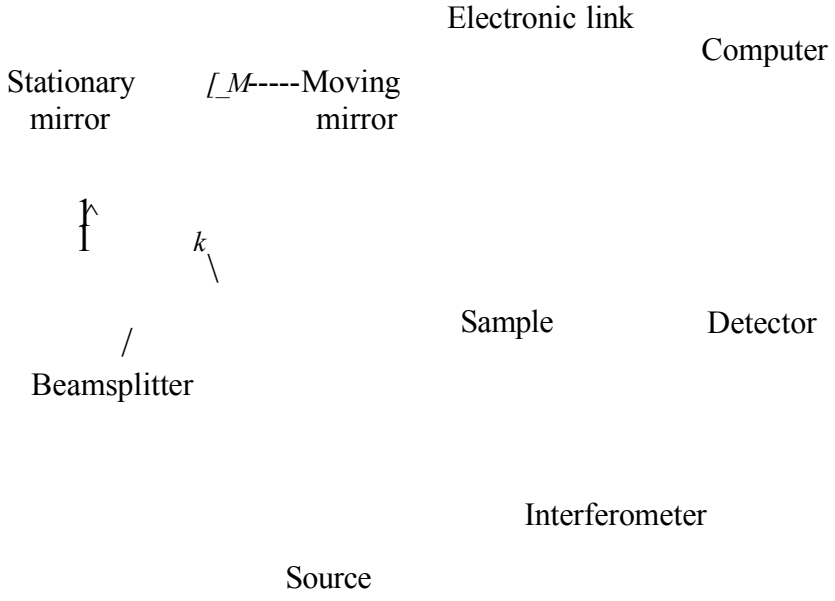

Figure 3.15: Schematic of a FTIR spectrometer.

In a Fourier transform infrared (FTIR) spectrometer, which is based on a Michelson interferometer, radiations of all wavelengths pass through the sample to the detector simultaneously. The interferometer is a fundamentally different piece of equipment than a monochromater. The light passes through a beamsplitter, which sends it in two directions at right angles. One beam goes to a stationary mirror then back to the

beamsplitter. The other goes to a moving mirror. The motion of the mirror makes the total path length variable versus that taken by the stationary-mirror beam. When the two meet up again at the beamsplitter, they recombine, but the difference between the path lengths creates constructive and destructive interference: an interferogram. The recombined beam passes through the sample. The sample absorbs some radiadions of particular wavelength, according to its optical properties, which subtracts specific wavelengths from the interferogram. The detector now reports variation in energy-versus-time for all wavelengths simultaneously. A laser beam is superimposed to provide a reference for the instrument operation.

Energy versus time is an unusual way to record a spectrum. A mathematical function called Fourier Tranform (FT) allows the conversion of an intensity-versus-time spectrum into an intensity-versus-frequency spectrum.

The Fourier Transform is given by

$$A(f)=\sum X(t)\exp\left(-2\pi\frac{ift}{N}\right) \tag{3.6}$$

$A(f)$ and $X(t)$ are the frequency and time domain points, respectively, for a spectrum of N points.

The output of the detector is digitised, and a small computer program will do the transform in a matter of seconds (or less).

There are several advantages to this design:

- All of the source energy gets to the sample, improving the inherent signal-to-noise ratio.
- The resolution is limited by the design of the interferometer. The longer the path of the moving mirror, the higher the resolution. Even the least expensive FT instrument provides better resolution than the best dispersive instrument.
- The digitisation and computer interface allow multiple scans to be collected, therefore dramatically improving the signal-to-noise ratio. Most of the computer programs today allow further mathematical refinement of the data, such as the

subtraction of a reference spectrum, the correction of the baseline or the edition of spurious peaks.

The one minor drawback is that the FT instrument is inherently a single-beam instrument. It cannot use the "channel ratio" trick used in continuous wavelength operation. One result is that IR-active atmospheric components (CO_2, H_2O) will appear in the spectrum. Usually, a "Background" spectrum is run, then automatically subtracted from every spectrum.

3.2.10 Photoelectrochemical (PEC) measurements

PEC measurements are non-destructive and used to determine the electrical conductivity type of semiconductor materials [10].

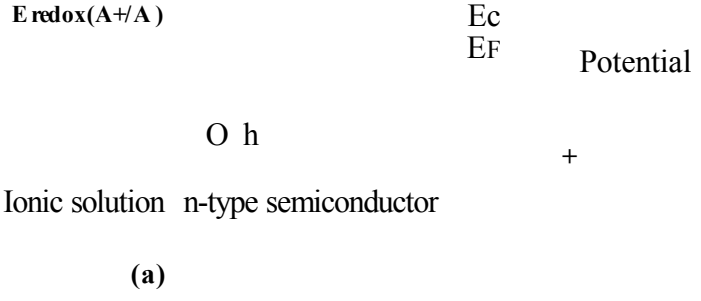

(a)

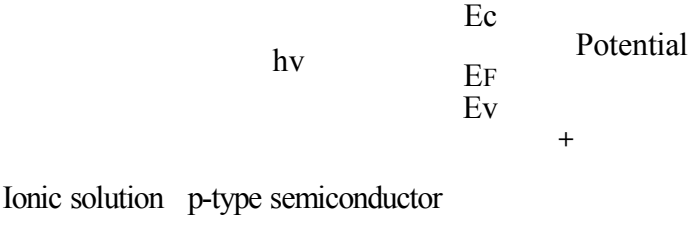

(b)

Figure 3.16: Band diagrams of (a) n-type semiconductor-liquid junction, p-type semiconductor-liquid junction.

When a semiconducting electrode is immersed in a solution containing a redox couple, the chemical potential at both electrode and solution must be identical, if no external force is applied. The bands in the semiconductor bend so as to equalise the Fermi level and the redox potential. The direction of bending depends on the particular system, but for n- or p-type materials it is usually in the direction indicated in Figure 3.16. Illumination of the electrode surface can bring about promotion of electrons from valence to conduction bands and the field gradients at the junction will result in separation of the photo-generated electrons and holes, as in the purely solid-state case described in Section 2.2.4. For upward curvature, as in Figure 3.16 (a), electrons move into the bulk of the semiconductor, while holes leave the surface to oxidise the anions of the redox couple. If an external circuit is made with a counter electrode immersed in the solution, then the electrons will flow from the semiconductor electrode to the counter electrode to reduce ions in solution. Figure 3.16 (b) shows the analogous energy diagram for absorption by the p-type material, from which electrons leave the surface to reduce the cations of the redox couple. The direction of the current or the polarity of the voltage measured in the external circuit gives the conductivity type of the semiconductor. The magnitude of the detected response indicates the suitable doping range of the solid material.

3.3 Device characterisation

Two methods were used to characterise the solar cells: current-voltage (I-V) and capacitance-voltage (C-V) measurements. Several electrical properties of the devices were examined, such as the fill factor FF, short circuit current I_{sc}, open circuit voltage V_{oc}, energy conversion efficiency η, series resistance R_s, shunt resistance R_{sh}, ideality factor n, barrier height ϕ_b, depletion width w and doping concentrations N_d or N_a.

3.3.1 Current-voltage (I-V) measurements

This technique, which simply measures the I-V characteristics, provides the most important information for device assessment. The equivalent circuit of a solar cell, shown in Figure 3.17, includes the series resistance R_s from the bulk of the semiconductor materials, metal contacts and interconnections, and the shunt resistance

R_{sh} related to the leakage currents [11]. The current source I_{ph} represents the photogenerated current.

V

Figure 3.17: Equivalent circuit of a solar cell.

The relationship between I and V under illumination is given by

$$I = I_0 \left[\exp\left(\frac{q(V - IR_s)}{nkT} \right) - 1 \right] + \frac{V - IR_s}{R_{sh}} - I_{ph} \qquad (3.7)$$

which can be reduced, if $I_{ph} > V > 3kT/q$ ($\approx 0.075V$) and $R_{sh} \to +\infty$, to

$$I = I_0 \left[\exp\left(\frac{qV}{nkT} \right) - 1 \right] - I_{ph} \qquad (3.8)$$

where I_{ph} is the photogenerated current, I_s is the saturated current, q is the magnitude of the electronic charge, T is the temperature, V is the bias applied, R_s is the series resistance, R_{sh} is the shunt resistance and n is the ideality factor.

The typical current-voltage characteristics of a p-n junction diode in the dark and when illuminated are given in Figure 3.18.

The saturated current I_s can have different expressions depending on the structure of the device considered.

For a p-n junction, $$I_s = Aq \left(\frac{D_p p_n}{L_p} + \frac{D_n n_p}{L_n} \right) \qquad (3.9)$$

where A is the area of the contact, Dp is the diffusion coefficient of holes in the n-type region, Dn is the diffusion coefficient of electrons in the p-type region, pn is the density of free holes in the n-type region at thermal equilibrium, npo is the density of free electrons in the p-type region at thermal equilibrium, Lp is the diffusion length of holes in the n-type region and Ln is the diffusion length of electron in the p-type region.

For a Schottky junction, $Is = AA^{**}T2 \exp \frac{}{kT}$ (3.10)

where A^{**} is the effective Richardson constant and ϕh is the barrier height.

These expressions for the saturated current are only valid for near ideal diodes, i. e. for pure thermionic emission of electrons over the barrier. If recombinations and generations occur in the depletion region and field emission occurs across the barrier, the value for the saturated current will increase.

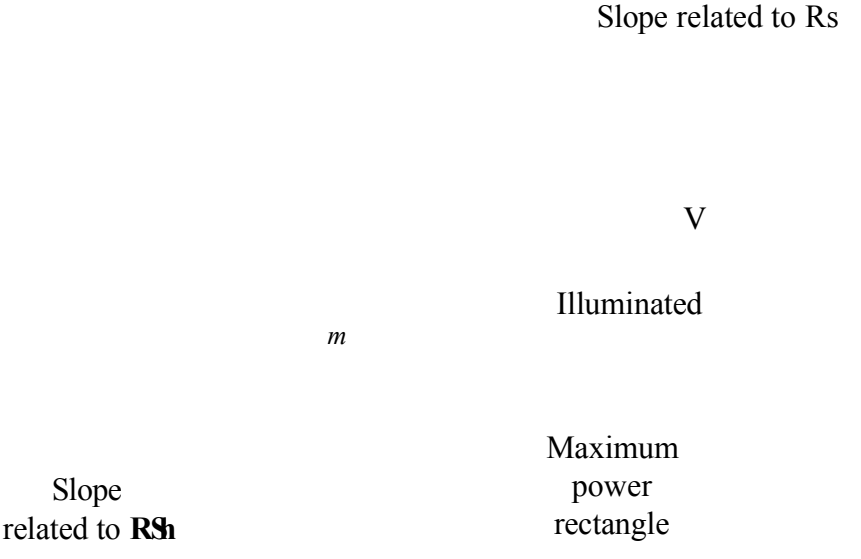

Figure 3.18: **Current-voltage characteristics of a p-n junction diode in the dark and when illuminated defining the basic parameters: the short circuit current Isc, the open circuit voltage V''. and the fill factor FF.**

Three parameters are generally used to characterise the solar cell performance. The first one is the short-circuit current I_{sc}, which is ideally equal to the photo-generated current:

$$I_{sc} = I_{ph} \tag{3.11}$$

From the current-voltage characteristics in Figure 3.18, it can be determined as the intercept of the curve with the y-axis.

The second parameter is the open-circuit voltage V_{oc}, which is obtained from equation (3.8) by putting $I = 0$, when $V = V_{oc}$:

$$V_{oc} = \frac{nkT}{q} \ln\left(\frac{I_{ph}}{I_S}\right) \tag{3.12}$$

which becomes, for near ideal Schottky junctions

$$V_{oc} = n\left[\phi_b + \frac{kT}{q} \ln\left(\frac{I_{sc}}{AA^{**}T^2}\right)\right] \tag{3.13}$$

From the current-voltage characteristics, it can be determined as the intercept of the curve with the x-axis.

The power output for a given operating point in the fourth quadrant (in bottom, on the right) of the current-voltage curve, $P = IV$, is equal to the area of the rectangle that is defined by the corresponding values (V_p, I_p). The maximum possible area (V_{mp}, I_{mp}) (see Figure 3.18) defines the fill factor FF:

$$FF = \frac{V_{mp} I_{mp}}{V_{oc} I_{sc}} \tag{3.14}$$

The energy conversion efficiency of the solar cell η is a function of these three parameters:

$$\eta = \frac{I_{mp}V_{mp}}{P_{in}} = \frac{FF.V_{oc}.I_{sc}}{P_{in}} \tag{3.15}$$

where P_{in} is the total power of the incident light.

The three parameters, which determine the efficiency of the solar cell, depend on several factors.

- The series resistance R_s, which can be evaluated by the slope of the I-V curve in the high forward direction. Large slope indicates low series resistance and therefore higher fill factor and short circuit current.
- The shunt resistance R_{sh}, which can be evaluated by the slope of the I-V curve in the reverse direction. Low slope indicates large shunt resistance desired for increasing the fill factor.
- The barrier height ϕ_b, which is related to the open circuit voltage in a Schottky junction, as seen in equation (3.13). In the dark and in the voltage range $\phi_b > V > 3kT/q$, equation (3.8) is used to extract the zero-bias barrier height. When plotted on a semi-log scale, (3.8) is a straight line whose y-intercept provides I_S and therefore ϕ_b through equation (3.10). This calculation is only valid if the recombination and generation and field emission processes are negligible. As discussed before, these processes increase the reverse saturated current leading to an under estimation of the barrier height ϕ_b.
- The ideality factor, which is deduced from the $gradient = q/(2.303nkT)$ of the semi-log scale plot of equation (3.8) in the dark. The more n is close to the unity, the more ideal is the diode, i.e. the electron transport mechanism across the barrier is mainly related to thermionic emission of electrons over the barrier. The more n is close to 2, the more recombination and generation occur, which increase the saturated current and therefore decrease the open circuit potential.

The I-V measurements were made using a fully automated Keithley 619 system. Light was produced by a Bentham 605 Illuminator system adjusted to give an input power of

100 mWcm^{-2}. Two sharp probes were placed into contact with the processed sample, one on the diode and the other on the substrate used as an ohmic contact.

3.3.2 Capacitance-voltage (C-V) measurements

The C-V measurements provide the depletion width w, the doping concentration N_d or N_a and the barrier height ϕ_b in metal semiconductor junctions [11]. When a small AC voltage is superimposed upon a DC bias on a metal-semiconductor junction, charges of one sign are induced on the metal surface and charges of the opposite sign in the semiconductor. The relationship between C and V is given by

$$C = \left(\frac{q \varepsilon N_d}{2(V_{bi} - V - kT/q)} \right)^{\frac{1}{2}} = \frac{\varepsilon}{w} \tag{3.16}$$

where V_{bi} is the built-in potential, ε the semiconductor permittivity, k the Boltzmann constant, T the temperature and q the magnitude of the electronic charge.

A similar expression is given for semiconductors doped p-type, where N_a substitutes for N_d in equation (3.16). If the material is uniformly doped, the plot of $1/C^2$ versus V is a straight line whose slope is inversely proportional to the doping concentration N_d or N_a. From the intercept on the voltage axis, one can determine the built-in potential V_{bi} and therefore the barrier height ϕ_b through

$$\phi_b = V_{bi} + \xi \tag{3.17}$$

where ξ is the voltage difference between the Fermi level and the conduction band for a n-type semiconductor or the valence band for a p-type semiconductor.

The capacitance–voltage measurements were carried out using a fully automated Keithley 619 system and a Hewlett Packard 4284 A Oscilloscope.

3.4 References

[1] Andrews K. W., Physical Metallurgy: Technique and Applications, Allen & Unwin (1973).

[2] Warren B. E., X-Ray Diffraction, Addison-Wesley (1969).

[3] Gardiner D. J., Graves P. R., Practical Raman Spectroscopy, Springer (1989).

[4] Brune D., Hellborg R., Whitlow H. J., Hunderi O., Surface Characterization, VCH (1997).

[5] Skoog D. A., West D. M., Holler F. J., Fundamentals of analytical chemistry, 7th edition, Saunders (1996).

[6] http://www.chemistry.vt.edu/chem-ed/ac-meths.html.

[7] Vickerman J. C., Surface analysis: the principal techniques, Wiley (1997).

[8] Payling R., Jones D. G., Bengtson A., Glow discharge optical emission spectrometry, Wiley (1997).

[9] Raffaelle R. P, Forsell H., Potdevin T., Friedfeld R., Mantovani J. G., Bailey S. G., Hubbard S. M., Gordon E. M., Hepp A. F., Solar Energy Materials and Solar Cells 57 (1999) 167.

[10] Wayne R. P., Principles and Applications of Photochemistry, 2nd Edition, Oxford UP (1988).

[11] Sze S. M., Physics of Semiconductor Devices, 2nd Edition, Wiley (1981).

Chapter 4: Characterisation of TCO and development of window materials

4.1 Introduction

In this section, the properties of the substrates used to grow the semiconductor films are explored as well as the growth and development of the window materials.

This chapter can be divided into two parts. First, attention will be given to the structural and morphological properties of the transparent conducting oxides (TCO). Both indium tin oxide (ITO) and fluorine tin oxide (FTO) substrates were used in this work because their different compositional and structural properties allow a full characterisation of the deposited films. The glass/FTO substrate was used for compositional analysis of the absorber layers, as ITO contains indium, which enters the composition of $CuInSe_2$. It will be shown that the glass/FTO substrate is not suitable for XRD analysis, as FTO peaks overlap $CuInSe_2$ and CdS peaks. Therefore, glass/ITO was preferentially used as a substrate for electrodepositing $CuInSe_2$ and CdS when the structural properties of these films were studied. In the second part of this chapter, the experimental details for the growth of the window materials (ZnSe and CdS) will be given. Then, one will report and discuss the structural, morphological and optical properties of the deposited layers in order to confirm that these window materials can effectively be grown by the technique of electrodeposition. Finally, the conductivity type of the electrodeposited layers will be determined, as it is crucial for the design of the final device structures. The main results will be summarised at the end of the chapter.

4.2 Characterisation of the TCO materials

Thin film solar cells rely on transparent conducting oxide (TCO) to make the front contact of the devices. The TCOs generally used are In_2O_3 and SnO_2, which are wide band gap semiconductors (Eg= 3.5 eV). Doping of these materials with tin for In_2O_3 and fluorine for SnO_2 is usual in order to increase their conductivity, as the resistance of the TCO layer contributes to the series resistance of the solar cell. These conducting oxides, which have high electrical conductivity and optical transparency, serve not only as an electrical contact to the thin film solar cells but also as an anti-reflective coating.

4.2.1 Structural analysis

4.2.1.1 XRD of FTO

Figure 4.1 shows the XRD pattern of the glass/FTO substrate. The spectrum is dominated by nine peaks related to the diffraction by the atomic planes (110), (101), (200), (211), (220), (310), (112) or (301), (321) and (222) of the polycrystalline tetragonal structure of SnO_2.

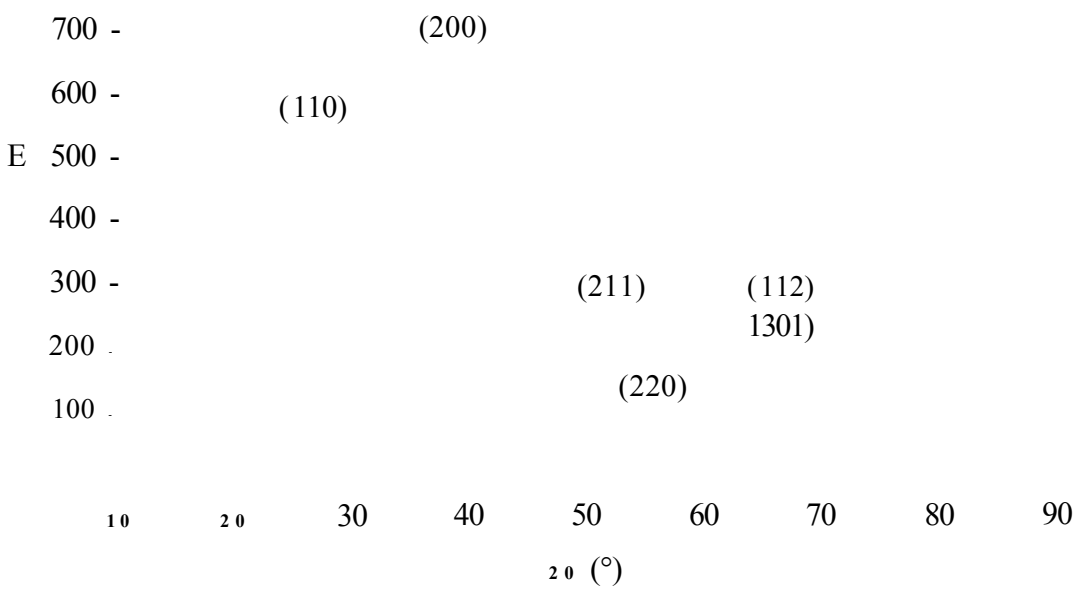

Figure 4.1: XRD pattern of the glass/FTO substrate.

The fluorine, which is used to dope the tin oxide semiconductor layer, does not make any noticeable changes to the XRD pattern, as it is present in very low concentrations.

The amorphous hump is due to the background of the glass. Considering the most intense and sharpest peak related to the (200) plane orientation, a crystallite size of 28.3 nm was estimated using the Scherrer equation.

All the peaks observed in the XRD pattern of the glass/FTO substrate are reported in Table 4.1 and their respective positions, relative intensities and associated atomic planes related to the tetragonal structure of SnO_2 are given.

2θ (°)	d (Å)	Relative intensity (%)	(hkl)
26.60	3.35	62.4	(110)
33.76	2.65	9.4	(101)
37.84	2.37	100.0	(200)
51.54	1.77	28.5	(211)
54.62	1.68	5.1	(220)
61.83	1.50	12.5	(310)
65.53	1.42	18.0	(112)(301)
78.34	1.22	1.8	(321)
80.71	1.19	4.1	(222)

Table 4.1: Respective positions, relative intensities and associated atomic planes of the peaks observed in the XRD spectrum of the glass/FTO substrate.

4.2.1.2 XRD of ITO

Figure 4.2 shows the XRD pattern of the glass/ITO substrate. The spectrum is dominated by six peaks related to the diffraction by the atomic planes (211), (222), (400), (431), (440) and (622) of the polycrystalline cubic structure of In_2O_3. The fact that there is no noticeable peaks or shifts related to the presence of a SnO_2 phase, suggests that the ITO films used in this work are more likely to be Sn doped-In_2O_3 than a mixture of In_2O_3 and SnO_2. It is interesting to note that the amorphous hump due to the background of the glass is bigger than in the case of the glass/FTO substrate, the reason being probably that the ITO layer is thinner than the FTO layer. Considering the most intense and sharpest peak related to the (400) plane orientation, a crystallite size of 27.2 nm was estimated using the Scherrer equation, which is very close to the one calculated for FTO.

All the peaks observed in the XRD pattern of the glass/ITO substrate are reported in Table 4.2 and their respective positions, relative intensities and associated atomic planes related to the cubic structure of In_2O_3 are given.

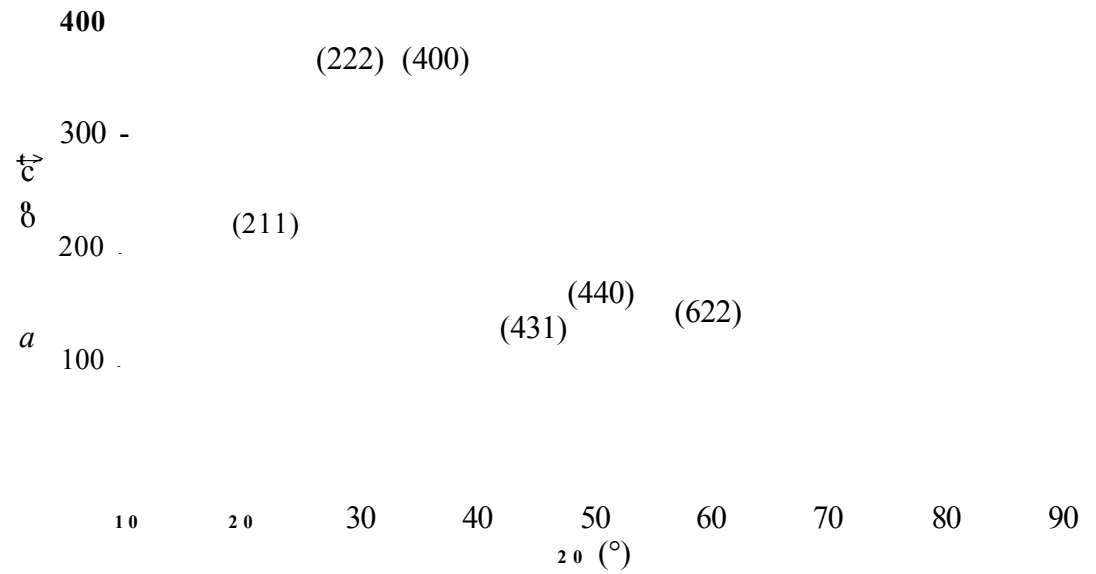

Figure 4.2: XRD pattern of the glass/ITO substrate.

2θ (°)	d(A)	Relative intensity (%)	(bkl)
21.36	4.16	17.6	(211)
30.37	2.94	81.6	(222)
35.29	2.54	100.0	(400)
45.15	2.01	7.3	(431)
50.66	1.80	21.0	(440)
60.16	1.54	15.5	(622)

Table 4.2: Respective positions, relative intensities and associated atomic planes of the peaks observed in the XRD spectrum of the glass/ITO substrate.

4.2.2 Morphological analysis

As the grain size of the TCO films was too small to observe any crystalline features within the capability of SEM, atomic force microscopy was performed in order to examine the surface morphology of the substrates used in this work. The contact mode operating with a very low frequency of 0.5 Hz and high resolution was employed for the analysis of the films. Both FTO and ITO have very similar morphology, therefore only the AFM pictures of ITO are displayed in Figure 4.3 (refer to [1] for AFM pictures of FTO). The observed grain morphology is typical of polycrystalline uniform growth. The layers are formed of very small and sharp grains with a size of approximately 0.1 pm. Evidence of a compact surface morphology was obtained by high resolution 3-D AFM of the film surface, as shown in Figure 4.3 (b). One can also see that the TCO films are

uniform and void free. It is finally interesting to note that the grains are electrically well connected to each other. The surface roughness calculated using a root mean square (rms) value function is 2.2 nm on a 5 x 5 jam2 scan area.

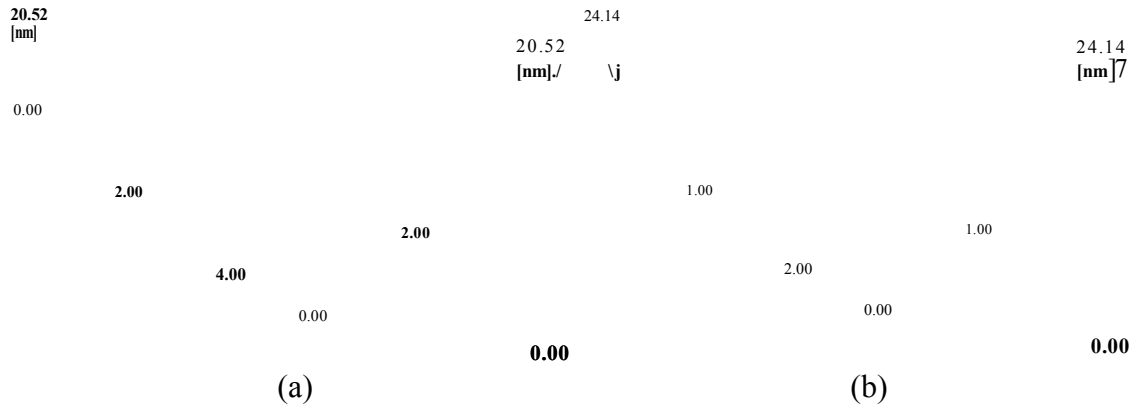

Figure 4.3: 3-dimentional view AFM pictures of the glass/ITO substrate: scan area of (a) 5 x 5 pm2 and (b) 2.5 x 2.5 pm2.

4.3 Development of the window materials

The window materials used in this project are zinc selenide (ZnSe) and cadmium sulfide (CdS), which are semiconductors with wide optical band gap of 2.67 eV and 2.42 eV [2], respectively. The electrodeposition of ZnSe and CdS on glass/FTO or glass/ITO substrates was achieved following the conditions established at Sheffield Hallam University and the deposited films were characterised to investigate their structural, morphological, optical and electrical properties. More details about the growth and the analysis of these materials can be found elsewhere [3,4, 5, 6].

4.3.1 Electrodeposition of ZnSe

4.3.1.1 Experimental details

Electrodeposition of ZnSe is based on the individual reactions of zinc and selenium and their related Nemst equations:

$$Zn^{2+} + 2e^- \leftrightarrow Zn$$

$$E_{Zn} = E^o_{Zn} + \frac{RT}{2F}\ln\frac{(Zn^{2+})}{(Zn)} = -0.96 + 0.0295\log\frac{(Zn^{2+})}{(Zn)}$$

$$H_2SeO_3 + 4H^+ + 4e^- \leftrightarrow Se + 3H_2O$$

$$E_{Se} = E^o_{Se} + \frac{RT}{4F}\ln\frac{(H_2SeO_3)}{(Se)} + \frac{3RT}{4F}\ln(H^+) = 0.535 + 0.0148\log\frac{(H_2SeO_3)}{(Se)} - 0.0433pH$$

where E^o_{Zn} and E^o_{Se} are the standard electrode potentials of zinc and selenium, respectively with respect to Ag/AgCl reference electrode. (Zn^{2+}) and (H_2SeO_3) refer to the activities of the respective species in the solution. (Zn) and (Se) represent the activities of the respective atoms in the electrodeposit, which are equal to 1 for pure elemental deposition.

Electrodeposition of ZnSe was carried out using a classical three-electrode potentiostatic system, as described in section 2.4.1.1, by means of a Gillac ACM instrument, a double-junction Ag/AgCl reference electrode, a carbon counter electrode and TCO coated glass substrates as working electrodes. As already discussed, both ITO and FTO were used as the TCO in this project. The substrates were cleaned thoroughly by refluxing in dichloromethane and washing in acetone followed by distilled water prior to deposition. Aqueous solution for depositing ZnSe layers contained 0.1 M $ZnCl_2$ (99.999 %) and 10^{-5} M H_2SeO_3 (99.999%). The pH of the electrodeposition bath was adjusted to 2.3 by addition of HCl. The temperature of deposition was maintained at 60°C. A slow stirring was used to improve the quality of the films. The deposition of ZnSe was performed at -0.54 V with respect to Ag/AgCl reference electrode for 3 hours. The measured current density was about 60 $\mu A.cm^{-2}$ and the theoretical thickness of the films was estimated to be 0.3 μm by using Equation (2.14). For this calculation, the values of the molecular weight (144.34 $g.mol^{-1}$) and the density (5.42 $g.cm^{-3}$) of intrinsic ZnSe were used [7]. The number of electrons transferred was taken as 6, according to the total electrode reaction. The samples were finally annealed at 200°C in air atmosphere for 15 minutes to improve their bulk as well as electrical properties.

4.3.1.2 Structural analysis

It has not been possible to detect ZnSe from XRD analysis, as the electrodeposited material does not develop abundant crystallites. Thus, Raman analysis has been performed because it is more sensitive to short-range order than XRD and weak Raman peaks can be observed, if there are few bonds to scatter. One reason is given by considering Raman as measuring the vibrations of Zn-Se bonds in a phase whilst XRD looks at the diffraction of x-rays by the planes of the crystals. Another reason may be that Raman spectroscopy is more of a surface sensitive technique and XRD is a bulk analysis technique, as x-rays penetrate into the sample deeper than Raman excitation line. Therefore, the substrate of the films is detected more in XRD than in Raman, leading to less sensitivity for the detection of the films on the surface.

Raman measurements of the ZnSe layers were performed on a triple XY-800 DILOR spectrometer with multichannel detection (CCD camera) at Warsaw University of Technology. The argon laser power (514.5 nm line) was kept below 40 mW to prevent sample damage. In Figure 4.4 is displayed the Raman spectrum of an annealed ZnSe film grown on a glass/ITO substrate by electrodeposition. The assignment of the observed modes was made on the basis of published data [8, 9]. Two broad bands are observed at 202 and 256 cm'1, which are attributed to the transverse and longitudinal oscillations of the cubic lattice, respectively. Therefore the presence of ZnSe is confirmed.

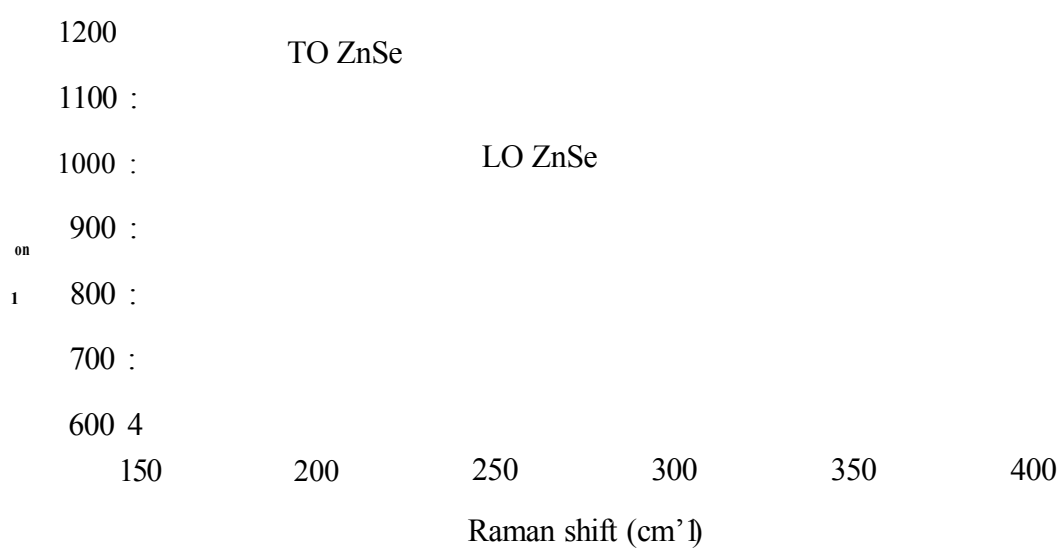

Figure 4.4: **Raman spectrum of an annealed ZnSe film grown on a glass/ITO substrate by electrodeposition.**

4.3.1.3 Morphological analysis

The surface morphology of the films was examined by AFM in the contact mode operating with a very low frequency of 0.5 Hz and high resolution. Figures 4.5 (a) and (b) represent the 2-dimensional and 3-dimensional images of a ZnSe film on a 2.5 x 2.5 pm_2 scan area. The observed grain morphology is representative of polycrystalline uniform growth. The layers are formed of platelets orientated along the same direction with a size of approximately 0.5 pm. The high resolution 3-D AFM of the film surface shown in Figure 4.5 (b) reveals a compact surface morphology. It can also be seen that the surface of the film is smooth and void free and that the grains are electrically well connected to each other. The surface roughness calculated using a root mean square (rms) value function is 8.3 nm on a 2.5 x 2.5 pm_2 scan area.

(a) (b)

Figure 4.5: AFM pictures of an annealed ZnSe film grown on a glass/FTO substrate by electrodeposition: (a) plane view and (b) 3-D view on a 2.5 x 2.5 pm_2 scan area.

4.3.1.4 Optical analysis

The optical measurements of ZnSe thin films were performed on a UNICAM model UV2 UV-visible spectrophotometer.

Figure 4.6 (a) shows the optical absorption curves of an annealed ZnSe film grown on a glass/ITO substrate by electrodeposition. One can see a sharp change in the absorbance, which occurs at wavelengths lower than 600 nm. This is representative of the optical

properties of semiconductors and demonstrates the existence of a well defined band gap energy.

To determine the band gap value of the electrodeposited ZnSe films, a plot of the (Absorbance.Energy)^2 versus the energy of the incident photons is shown in Figure 4.6 (b). A linear region is observed, indicating a direct energy gap. The interception of the slope with the x-axis gives a band gap value of 2.5 eV. This value, which is lower than the band gap of ZnSe reported to be 2.67 eV [2], could be explained by the deviation from the ideal composition or/and to some impurities or/and imperfections in the crystal lattice leading to some levels within the band gap. It is important to mention that the reflections and scatterings of the incident light are not taken into account, which could change the value of the measured band gap.

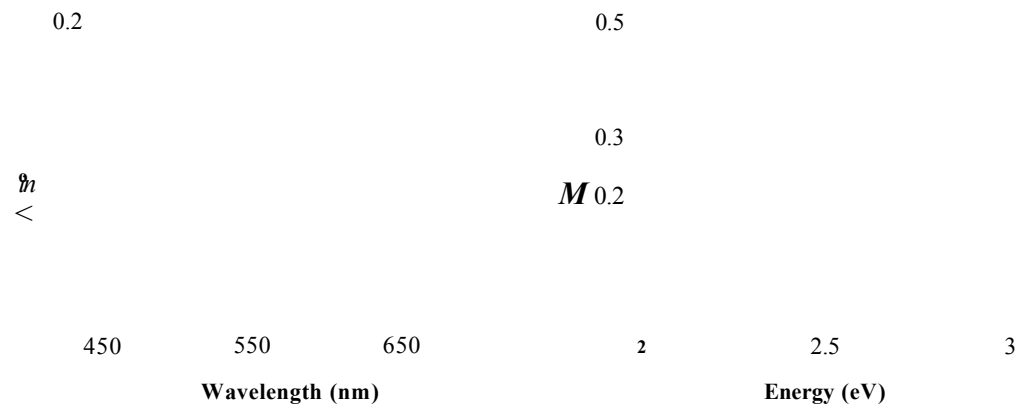

Figure 4.6: Optical absorption curves of an annealed ZnSe film grown on a glass/ITO substrate by electrodeposition: (a) plot of the absorbance versus the wavelength of the incident photons and (b) plot of the (Absorbance.Energy)^2 versus the energy of the incident photons.

4.3.1.5 Electrical analysis

Photoelectrochemical measurements were performed to determine the conductivity type of the electrodeposited ZnSe layers. The electrolyte used for photoelectrochemical (PEC) measurements was a 0.1 M KCl aqueous solution. As can be seen in Table 4.3, ZnSe films show a negative photovoltage demonstrating the n-type character of the material. Note that ZnSe can be doped with arsenic to produce p-type materials by addition of AS_2O_3 into the electrolyte [3]. As a matter of fact, selenium atoms are substituted for arsenic atoms and extra free holes are generated.

Material	V_{dark} (mV)	V_{light} (mV)	V_{photo} (mV)	Conductivity type
p-Si	-360	-320	+40	p-type
n-Si	-390	-530	-140	n-type
ZnSe	-232	-422	-190	n-type

Table 4.3: Photovoltage produced at liquid/ZnSe junction during white light illumination. P- and n-type silicon was used for comparison.

4.3.2 Electrodeposition of CdS

4.3.2.1 Experimental details

Electrodeposition of CdS is based on the overall electrode reaction:

$$Cd^{2+} + S_2O_3^{2-} + 2e^- \leftrightarrow CdS + SO_3^{2-}$$

Just as for the deposition of ZnSe, the electrodeposition of CdS was carried out by means of a classical three-electrode potentiostatic system using a Gillac ACM instrument, a double-junction Ag/AgCl reference electrode, a carbon counter electrode and TCO coated glass substrates as working electrodes. The substrates were cleaned thoroughly by refluxing in dichloromethane and washing in acetone followed by distilled water prior to deposition. The CdS deposition bath contained $CdCl_2$ (99+ %) dissolved in Millipore water (18 MΩ Resistance) to make a solution of 0.2 M Cd^{2+}. This solution was then electropurified at -0.55 V for a period of approximately 12 hours, so that a small amount of cadmium was plated out on to the glass/TCO substrate, as the electrode potential of cadmium is -0.61 V versus Ag/AgCl reference electrode. High purity $Na_2S_2O_3$ (99.999 %) was added to the purified solution to make it 0.01 M $S_2O_3^{2-}$. The pH of the electrodeposition bath was adjusted to 2.3 by addition of HCl acid. The temperature of deposition was maintained at 60°C. A slow stirring was used to improve the quality of the films. The deposition of CdS was performed at -0.6 V with respect to Ag/AgCl reference electrode for 2 hours. The measured current density was about 0.1 $mA.cm^{-2}$ and the theoretical thickness of the films was estimated to be about 1.1 μm by using Equation (2.14). For this calculation, the values of the molecular weight (144.36 $g.mol^{-1}$) and the density (4.82 $g.cm^{-3}$) of intrinsic CdS were used [7]. The number of electrons transferred was taken as 2, according to the total electrode reaction given above. Note that the effective thickness of the layers is likely to be less than the

estimated value, as some other reductions or oxidations can occur, in addition to those leading to the formation of CdS. The samples were annealed at 450°C in nitrogen atmosphere for 20 minutes to improve their bulk as well as electrical properties.

4.3.2.2 Structural analysis

Figure 4.7 shows the XRD pattern obtained for an annealed CdS layer grown on a glass/ITO substrate by the technique of electrodeposition. The spectrum is dominated by six peaks related to the diffraction by the atomic planes (100), (002), (101), (110), (112) and (104) of the polycrystalline hexagonal structure of CdS. All other peaks arise from the ITO substrate layer. Considering the most intense and sharpest peak related to the (002) plane orientation, a crystallite size of 38.8 nm was estimated using the Scherrer equation.

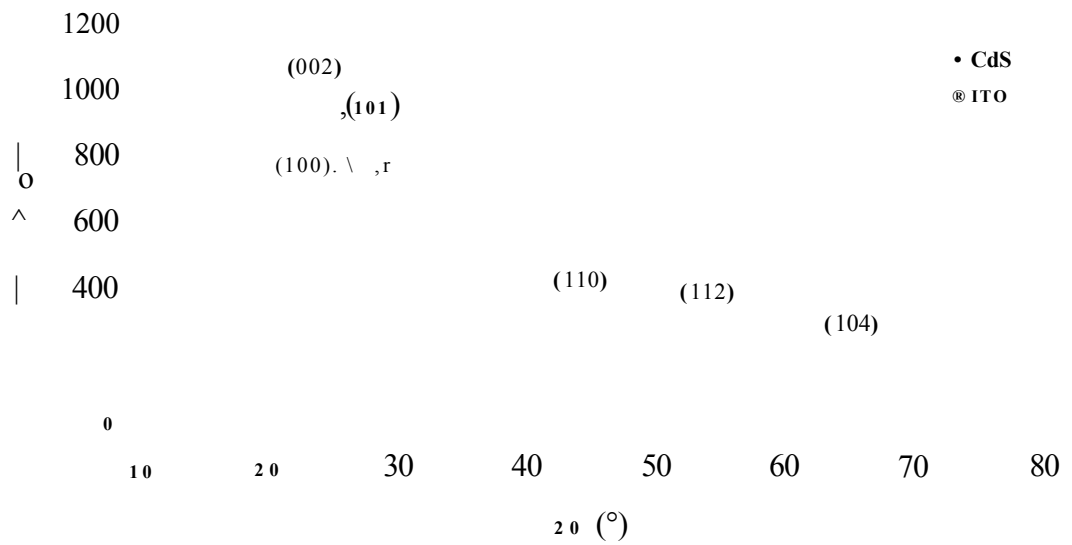

Figure 4.7: XRD pattern of an annealed CdS film grown on a glass/ITO substrate by electrodeposition.

Raman analysis of CdS layers was performed on a triple XY-800 DILOR spectrometer with multichannel detection (CCD camera) at Warsaw University of Technology. The argon laser (514.5 nm line) power was kept below 40 mW to prevent sample damage. The assignment of the modes observed in the Raman spectra was made on the basis of published data [10]. Figure 4.8 shows the typical Raman spectrum of an annealed CdS film grown on a glass/ITO substrate by electrodeposition. Two broad bands are observed

at 296 and 596 cm'1, which are attributed to the longitudinal optical phonons and its overtone, respectively. This result therefore confirms the XRD result and shows that CdS can be grown by the technique of electrodeposition.

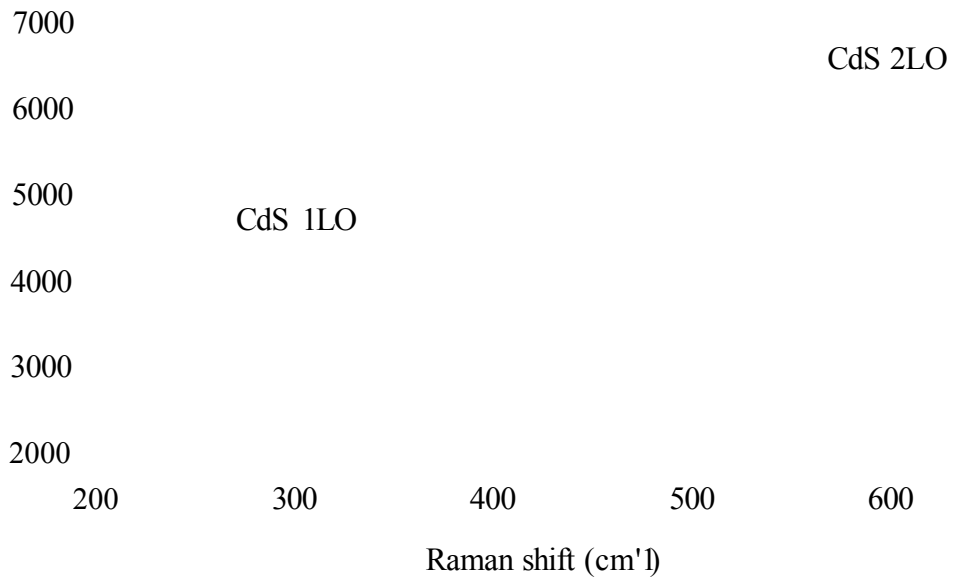

Figure 4.8: Raman spectrum of an annealed CdS film grown on a glass/ITO substrate by electrodeposition.

4.3.2.3 Morphological analysis

The surface morphology of the films was examined by AFM in the contact mode operating with a very low frequency of 0.5 Hz and high resolution. In order to grow high-efficiency photovoltaic CdS based heterojunctions, it is crucial to deposit compact CdS window layers on TCO coated glass substrates. This can be achieved by electrodeposition, as shown in Figures 4.9 (a) and (b) representing the 2-D and 3-D images of an annealed CdS film electrodeposited on a glass/FTO substrate. The films are polycrystalline and uniform. The layers are formed of platelets orientated along the same direction. The grains are bigger than for ZnSe thin films with an average size of 1 pm. Note the large difference between the grain size obtained from XRD and AFM analysis. The grain size estimated from the Scherrer equation is about 25 times smaller than the one observed in the AFM images. This is probably because the particles in the films seen in AFM pictures are not real crystallites, as detected by XRD, but consist of groups of small crystals. Another reason could be the lack of accuracy given by the calculations

using the Scherrer equation, as several factors, such as the instrumental broadening or the micro-strain, can contribute to the XRD peak broadening. It can also be seen from the high-resolution 3-D view image that the surface of the film is rather smooth, void free and that the grains are electrically well connected to each other. The surface roughness calculated using a root mean square (rms) value function is 8.8 nm on a 2.5 x 2.5 pm_2 scan area, which is higher than the one estimated for electrodeposited ZnSe surface.

(a) (b)

Figure 4.9: AFM pictures of an annealed CdS film grown on a glass/FTO substrate by electrodeposition: (a) plane view and (b) 3-D view on a 2.5 x 2.5 pm_2 scan area.

4.3.2.4 Optical analysis

The optical measurements of CdS thin films were performed on a UNICAM model UV2 UV-visible spectrophotometer.

Figure 4.10 (a) shows a typical optical absorption curve of an annealed CdS film grown on a glass/ITO substrate by electrodeposition. Similarly to the optical absorption curve of ZnSe, a sharp change in the absorbance occurs at wavelengths lower than 500 nm, which also demonstrates the existence of a well defined band gap energy.

To determine the band gap value of the electrodeposited CdS films, a plot of the $(Absorbance.Energy)_2$ versus the energy of the incident photons is displayed in Figure 4.10 (b). A quasi-linear region is observed, indicating a direct energy gap. The extrapolation of the linear portion to the intercept of the photon energy axis gives a band gap value of 2.48 eV, which is acceptable, as the band gap of CdS is reported to be 2.42

eV [2]. As already discussed, the reflections and scatterings of the light are not considered here, which could change the value of the measured band gap slightly.

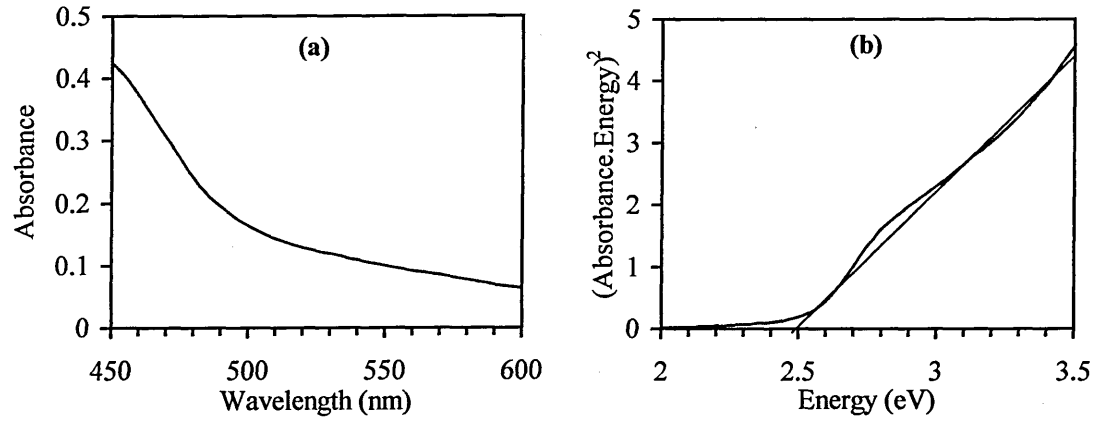

Figure 4.10: Typical optical absorption curves of an annealed CdS film grown on a glass/ITO substrate by electrodeposition: (a) plot of the absorbance versus the wavelength of the incident photons and (b) plot of the (Absorbance.Energy)^2 versus the energy of the incident photons.

4.3.2.5 Electrical analysis

Photoelectrochemical measurements have been performed to determine the conductivity type of the electrodeposited CdS layers. The electrolyte used for PEC measurements was a 0.1 M KCl aqueous solution. As can be seen in Table 4.4, CdS films show a negative photovoltage demonstrating the n-type character of the material. It is not very surprising that the electrodeposited CdS films are all n-type, as this is the conductivity type generally reported in the literature for this material, whatever the growth technique employed [2]. This conductivity is probably related to the presence of native defects, such as sulphur vacancies.

Material	V_{dark} (mV)	V_{light} (mV)	V_{photo} (mV)	Conductivity type
p-Si	-360	-320	+40	p-type
n-Si	-390	-530	-140	n-type
CdS	-230	-550	-320	n-type

Table 4.4: Photovoltage produced at liquid/CdS junction during white light illumination. P- and n-type silicon was used for comparison.

4.4 Summary and conclusions

In this chapter, it was demonstrated the polycrystalline structure of the transparent conducting oxides used in this work as well as their capacity to act as substrates suitable for the electrodeposition of good quality semiconducting materials.

It was also shown that ZnSe and CdS films could successfully be grown on glass/ITO or glass/FTO using the technique of electrodeposition. ZnSe films are rather amorphous, as no peaks were observed in the XRD spectra. However, Raman measurements showed the presence of the electrodeposited ZnSe material. CdS films are polycrystalline and the XRD pattern is dominated by 6 peaks related to the diffraction by the atomic planes (100), (002), (101), (110), (112) and (104) of the hexagonal structure.

Both CdS and ZnSe layers are smooth, void free and formed of densely packed grains, uniformly distributed, well orientated and electrically well connected to each other, as observed by atomic force microscopy of the surface of the films. This result is of prime importance for the growth of good quality absorber layers and the achievement of high-efficiency photovoltaic heterojunction devices. As a matter of fact, smooth films can show reduced light trapping at the surface but they are advantageous in that the number of interface states between the absorber layer and the window layer in the device is lowered. It is also crucial to be able to grow compact window materials in order to prevent the diffusion of Cu, In or Se atoms from the CIS layer though the window material layer.

Optical absorption and PEC measurements confirmed the semiconducting properties of these material layers. The band gaps of the ZnSe and CdS films were found to be 2.5 eV and 2.48 eV, respectively. Both electrodeposited materials showed n-type electrical conductivity. Therefore, p-type $CuInSe_2$ will have to be electrodeposited in order to make N-p heterojunction solar cells.

4.5 References

[1] Samantilleke A. P., Dharmadasa I. M., Prior K. A., Choy K. L., Mei J., Bacewicz R., Wolska A., Journal of Materials Science: Materials in Electronics, in print.

[2] Chu T. L., Chu S. S., Solid State Electronics, 38 (3) (1995) 533.

[3] Samantilleke A. P., Boyle M. H., Young J., Dharmadasa I. M., Journal of Materials Science: Materials in Electronics, 9 (1998) 231.

[4] Samantilleke A. P., PhD Thesis, Sheffield Hallam University (1998).

[5] Mc Gregor S. M., Dharmadasa I. M., Wadsworth I., Care C. M., Optical Materials, 6 (1996) 75.

[6] Mc Gregor S. M., PhD Thesis, Sheffield Hallam University (1999).

[7] Lide D. R., Handbook of Chemistry and Physics, 79th edition, CRC (1998-1999).

[8] Melnik N. N., Sadofyev Y. G., Zavaritskaya T. N., Journal of Crystal Growth, 214/215 (2000) 651.

[9] Dinger A., Becker R., Göppert M., Petillon S., Grün M., Klingshirn C., Liang J., Wagner V., Geurts J., Journal of Crystal Growth, 214/215 (2000) 676.

[10] Oladeji I. O., Chow L., Liu J. R., Chu W. K., Bustamante A. N. P., Fredricksen C., Schulte A. F., Thin Solid Films, 359 (2000) 154.

Chapter 5: Characterisation of $Cu(InGa)(SeS)_2$ grown by the two-stage method

5.1 Introduction

This section presents the results of the characterisation of $Cu(InGa)(SeS)_2$ layers grown on glass/molybdenum by the two-stage method at Showa Shell in Japan. These materials have been used as benchmark materials for comparison and development of electrodeposited materials. The two-stage method to prepare CIGSS thin film absorbers consists in the selenisation and sulfidation of Cu-25%Ga/In precusor stacked layers in a reaction furnace. The Cu-25%Ga/In precusor stacked layers are grown by DC magnetron sputtering on Mo sputter-coated soda-lime-glass substrates. The precursor layers are then annealed in a low-concentration H_2Se gas atmosphere at temperatures above 450°C and in low concentration H_2S gas atmosphere at temperatures above 500°C. The ramp-up rate is adjusted to enable a good adhesion between the absorber layers and the Mo substrates [1]. The best solar energy conversion efficiency achieved so far for a 30 x 30 cm^2 CIGSS thin film sub-module has been 11.6 % with a $Mo/Cu(InGa)(SeS)_2/Zn(O, S, OH)_x/ZnO$ device structure [2]. In this section, one will first study the structural properties of the $Cu(InGa)(SeS)_2$ material using x-ray diffraction (XRD) and Raman techniques. The morphology will then be examined through scanning electron microscopy (SEM) and atomic force microscopy (AFM) characterisation. The elemental analysis was performed using x-ray fluorescence (XRF), inductively coupled plasma mass spectroscopy (ICPMS), x-ray photoelectron spectroscopy (XPS) and glow discharge optical emission spectroscopy (GDOES) techniques. Finally, the conductivity type of the material will be determined by photoelectrochemical measurements. The main results will be summarised at the end of the chapter and used for comparison with electrodeposited CIS films.

5.2 Structural analysis

5.2.1 XRD analysis

XRD studies were carried out in order to identify the composition, crystallinity and phases of Cu(InGa)(SeS_2) thin films grown on glass/Mo substrates by the two-stage method. In the XRD pattern displayed in Figure 5.1, seven peaks corresponding to the diffraction by the atomic planes (101), (112), (211), (220) or (204), (312) or (116), (316) or (332) and (424) or (228) of the chalcopyrite structure are identified by comparison with the APD data card 40-1487. The material also shows a strong preferential growth with (112) orientation. All the peaks related to $CuInSe_2$ have a shoulder, which corresponds to a mixture of other phases, such as $CuInS_2$ or $CuGaSe_2$.

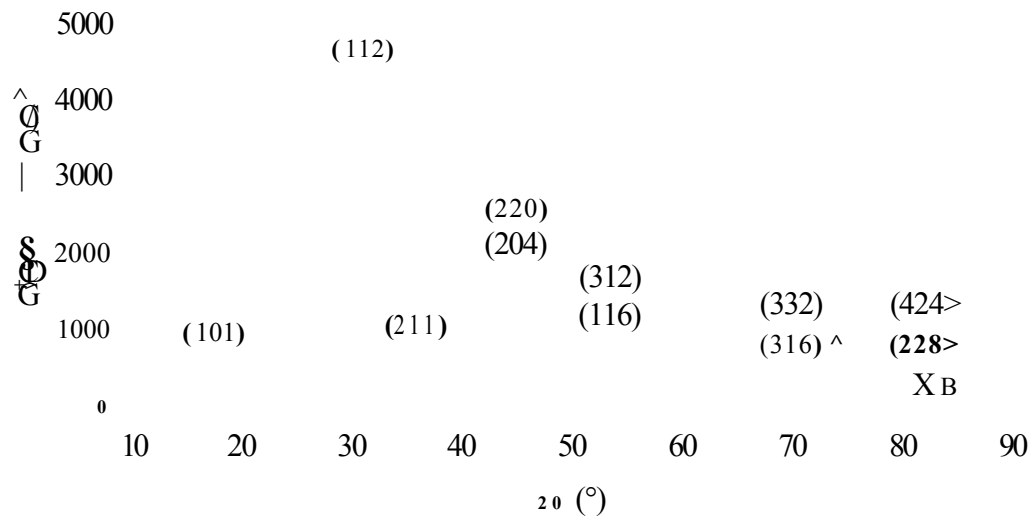

Figure 5.1: XRD pattern of Cu(InGa)(SeS_2) grown on glass/Mo substrate by the two-stage method.

Considering the most intense and sharpest peak related to the (112) plane orientation, a crystallite size of 28.4 nm was estimated using the Scherrer equation. One has, however, to consider this value with extreme care because the (112) peak contains several phases, as already discussed, which could explain the small crystallite size estimated using the Scherrer equation.

Other peaks, in addition to those related to the molybdenum substrate, are also observed at 31.83° and 56.22°. Although it was not possible to identify them, it is thought that they

are associated with selenium alloys, such as Cu-Se, Ga-Se or In-Se, as they appear after the selenisation step process of the two-stage method [1].

5.2.2 Raman analysis

Raman measurements of Cu(InGa)(SeS_2 layers were performed using a Renishaw Raman Microprobe (780 nm line). Figure 5.2 shows the Raman spectrum of a Cu(InGa)(SeS_2 film grown on a glass/Mo substrate by the two-stage method. Three peaks related to $CuInSe_2$ are identified at 176 cm'1, 212 cm^{-1} and 226 cm'1.

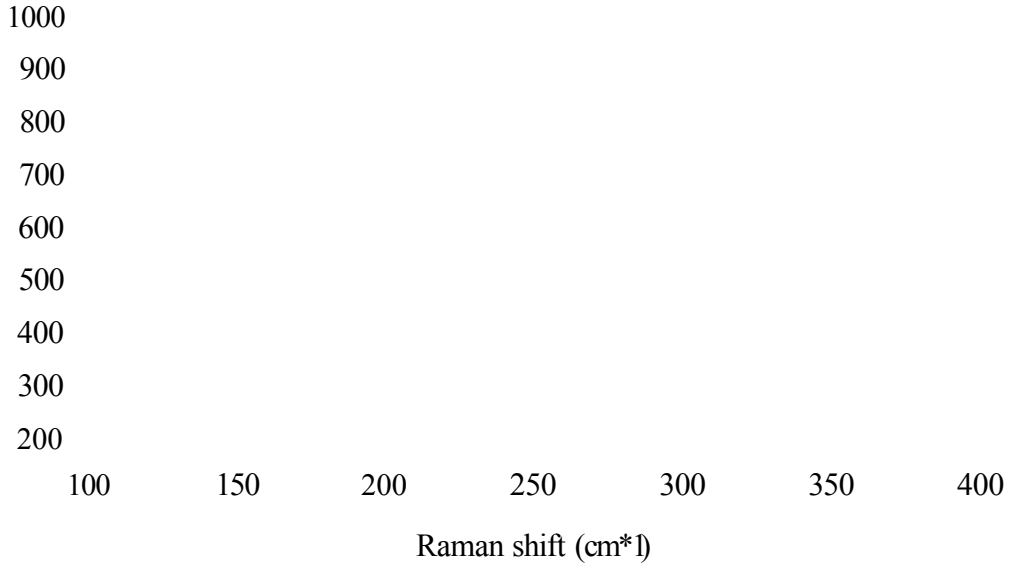

Figure 5.2: Raman spectrum of Cu(InGa)(SeS_2 grown on glass/Mo substrate by the two-stage method.

The peak at 176 cm^{-1} corresponds to the A1 mode resulting from the motion of the Se atom with Cu and In atoms remaining at rest and the peaks at 212 cm^{-1} and 226 cm^{-1} are due to the B2 and E modes, which correspond to the combined motion of all the atoms [3]. A shoulder on the A_1 mode peak of $CuInSe_2$ at about 150 cm^{-1} is assigned to the A_1 mode of Cufr^Ses [4]. The peak at 291 cm^{-1} is attributed to the A1 mode of $CuInS_2$ [5]. It is unexpected to observe a peak at 261 cm'1, which is associated with a Cu-Se mode by Lippold et al. [6], as it was shown in Section 2.3.2.4 that Cu-Se phases were detrimental to $CuInSe_2$-based solar cells. The spectrum of Cu(InGa)(SeS_2 shows also the presence of two additional peaks at higher frequencies centred at about 340 and 360 cm'1. They

may correspond to two of the strongest vibrational modes of $CuIn_5Sg$, as reported by Alvarez-Garcia et al. [7], which would point out the presence of this secondary phase on the surface of the deposited layer. It is interesting to note the simultaneous presence of both Cu-rich and In-rich phases, as already reported by Guillen and Herrero [8]. The shoulder at about 305 cm^{-1} on the A1 peak of $CuInS_2$ could be related to the presence of $CuInS_2$ with a symmetry different from the chalcopyrite, such as the CuAu or sphalerite structure [9]. An In-rich configuration not yet identified could also be responsible for the appearance of this peak.

5.3 Morphological analysis

5.3.1 SEM analysis

SEM was performed to study the surface morphology of $Cu(InGa)(SeS)_2$ layers grown by the two-stage method. Samples were mounted on a metal stub using silver conducting paint. Silver conducting paint was also used to form a conducting path between the semiconducting layers and the metal stub. This prevented excessive charging of the samples. A spot size setting between 2 and 5 and an accelerating voltage of 20 kV were found to produce good micrographs.

(a) (b)

Figure 5.3: SEM micrographs of a $Cu(InGa)(SeS)_2$ film grown on a glass/Mo substrate by the two-stage method for magnifications (a) x 3000 and (b) x 8000.

Figures 5.3 shows the surface morphology of $Cu(InGa)(SeS)_2$ grown on glass/Mo. The films appear dense with a good mechanical adhesion to the molybdenum substrate. The compactness of the CIGSS film is crucial, as it will prevent the diffusion of atoms during

the growth of the window material layer for the production of Cu(InGa)(SeS)$_2$-solar cells. SEM of the layer also shows crack-free surface with irregular-shaped grains, although their boundaries are not clearly observed. Note that some voids in the high-magnified image (Figure 5.3 (b)) are observed.

5.3.2 AFM analysis

The surface morphology of the films was also examined by AFM using the contact mode and a low frequency of 0.5 Hz. Figures 5.4 shows the 2-dimensional and 3-dimensional images of a Cu(InGa)(SeS)$_2$ film on $_{10}$ x $_{10}$ pm$_2$ and 2.5 x 2.5 pm$_2$ scan areas.

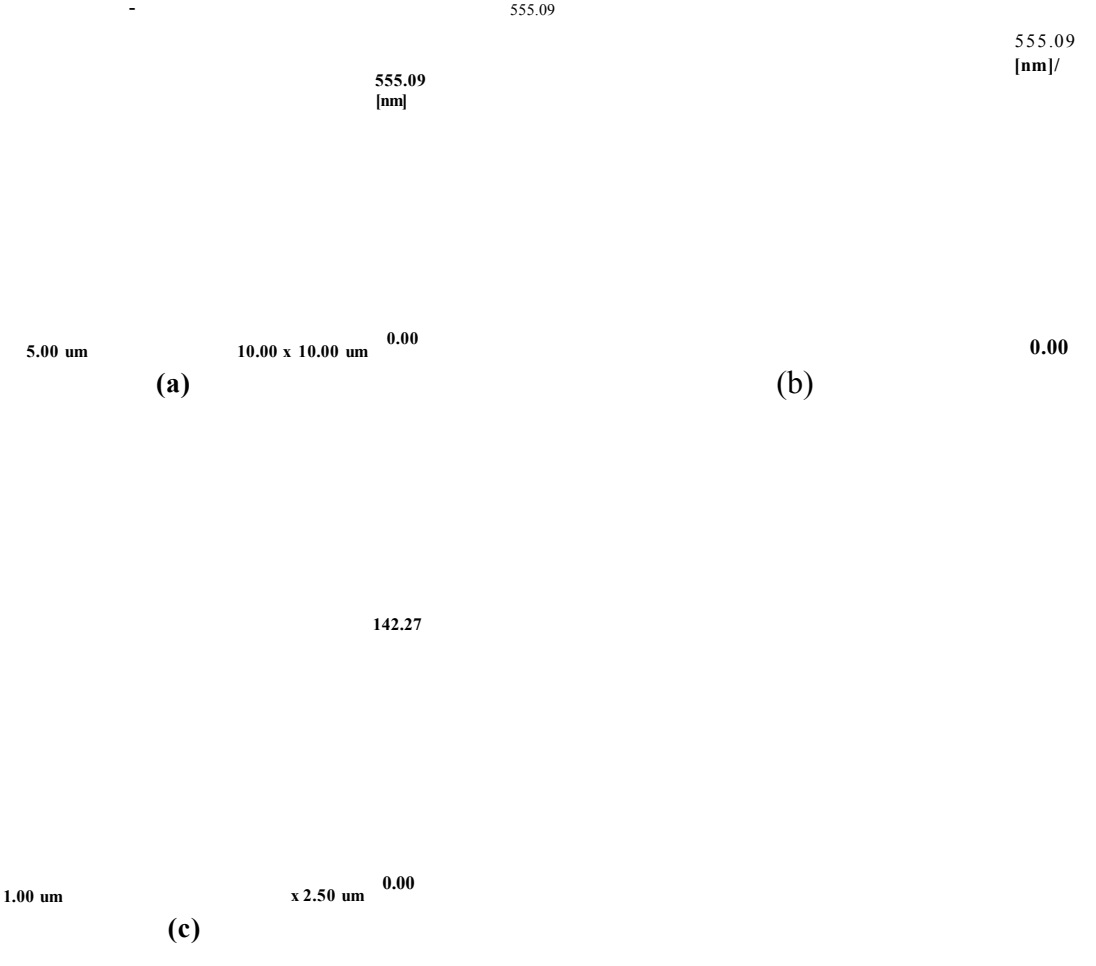

Figure 5.4: **AFM pictures of a Cu(InGa)(SeS)2 film grown on a glass/Mo by the two-stage method: (a) plane view (low magnification), (b) 3-D view (low magnification), (c) plane view (high magnification) and (d) 3-D view (high magnification).**

It can be seen that the layers are formed of long grains orientated along the same direction. High resolution 3-D AFM of the film surface shown in Figure 5.4 (d) reveals a compact surface morphology, as already observed by SEM. It can also be seen that the grains are electrically well connected to each other with a size up to 2 μm. The surface roughness calculated using a root mean square (rms) value function is 126.6 nm on a 10 x 10 μm^2 scan area and 21.5 nm on a 2.5 x 2.5 μm^2 scan area. The large difference between the surface roughnesses calculated for high and low magnifications shows the non-uniformity of the layers grown by the two-stage method. Note that rough surfaces are generally observed for films grown using sputtering techniques.

5.4 Compositional analysis

5.4.1 Bulk analysis

Bulk compositional analysis was performed on CIGSS films grown by the two-stage method using the two techniques of x-ray fluorescence (XRF) and inductively coupled plasma mass spectrometry (ICPMS). It is noted that the two techniques do not give exactly the same results. For the ICPMS analysis, a $Cu(InGa)(SeS)_2$ layer was dissolved in nitric acid.

Table 5.1 shows the atomic percentages of copper, indium, gallium, selenium and sulphur present in the material layers calculated from XRF measurements. The concentration of indium is lower than expected. For comparison, XRF performed on bulk crystals of $CuInSe_2$ grown by the vertical Bridgman technique revealed that these samples were also indium deficient, although their compositions were expected to be very close to stoichiometry. This indicates that the absolute values given by these measurements should be treated with care due to the different sensitivity of the elements involved in the analysis. For instance, radiations emanating from the x-ray tube may not be energetic enough to remove K level electrons from the indium atom, as it has a higher atomic number (Z=49). One other important point to consider is the samples under investigation. The Bridgman grown bulk $CuInSe_2$ sample generates x-rays within the body of the materials enabling accurate analysis of results, but the analysis of thin $Cu(InGa)(SeS)_2$ layers in the order of 1-2 μm and grown on glass/Mo substrates introduces more complications and deviations from the correct atomic composition

values. Therefore, the XRF measurements will only be taken as a guide in development process of electrodeposited $CuInSe_2$ layers and ICPMS will be performed to assess more accurately the composition of the films.

	Atomic composition ratio				
Growth technique	**[Cu] (%)**	**[In] (%)**	**[Ga] (%)**	**[Se] (%)**	**S (%)**
Two-stage method	19.7	7.6	6.0	46.9	19.8
Melt grown bulk CIS sample	25.0	15.0	0	60.0	0

Table 5.1: Atomic composition ratio of $Cu(InGa)(SeS)_2$ grown on glass/Mo substrate by the two-stage method as calculated from XRF measurements. A benchmark $CuInSe_2$ sample grown by vertical Bridgman technique was used for comparison.

In Table 5.2 are compared the atomic percentages of copper, indium, gallium and selenium present in the material layers calculated from XRF and ICPMS measurements. First, one can observe an increase in the In-ratio at the expense of the Cu- and Se-ratios from XRF to ICPMS measurements. This confirms that XRF is a less sensitive technique to indium than copper and selenium. One can deduce from the ICPMS results that the [Cu]/([In]+[Ga]) ratio is inferior to the unity, which is desired for high efficiency CIGSS-based solar cells, as Cu-Se phases have been observed on the surface of Cu-rich films [10]. Nevertheless, a Cu-Se phase is still observed by Raman spectroscopy, as reported in Section 5.2.2. On the other hand, it is more understandable to observe peaks related to $CuIn_3Se_5$ and $CuIn_5S_8$ phases in the Raman spectrum (See Section 5.2.2), as it is reported that these phases can segregate on the surface of In-rich films [7, 10].
It is important to remember that the $Cu_{2-x}Se$ phase covering the surface of Cu-rich $CuInSe_2$ films is highly conductive since it is a degenerated p-type material and therefore not suitable for photovoltaic solar cell devices [10].

	Atomic composition ratio			
Characterisation technique	**[Cu] (%)**	**[In] (%)**	**[Ga] (%)**	**[Se] (%)**
ICPMS	19.1	17.3	7.1	56.5
XRF	24.5	9.5	7.5	58.5

Table 5.2: Atomic composition ratio of a $Cu(InGa)(SeS)_2$ film grown on a glass/Mo substrate by the two-stage method as calculated from XRF and ICPMS measurements without considering the sulphur content in the film.

5.4.2 Surface analysis

XPS was carried out in order to examine the surface composition of the deposited films, which would be expected to vary from the bulk composition. XPS analysis was performed on a VG ESCALAB II using Mg K_α (1253.6 eV) radiation. The hemispherical energy analyser was calibrated with standard Ag and Au samples prior to use. Since the material layers are grown on glass/Mo substrates, a conducting path was achieved by connecting the CIS layer to the metal holder with Ag conducting paste. However, there was some charging and the spectra presented here have been charge corrected by using the C 1s peak (binding energy 284.8 eV). Survey scans were performed with a pass energy of 50 eV and the high resolution scans for the peaks of interest were performed with a pass energy of 10 eV. In this configuration, the instrument has a peak width of about 1.0 eV and a peak position within ± 0.1 eV. Analysis was performed at a pressure of about $1x10^{-9}$ mbar. A suitable background was subtracted before any curve fitting. The curve fitting routine used in this reported work consists of a convolution of a Lorentzian function and a Gaussian function.

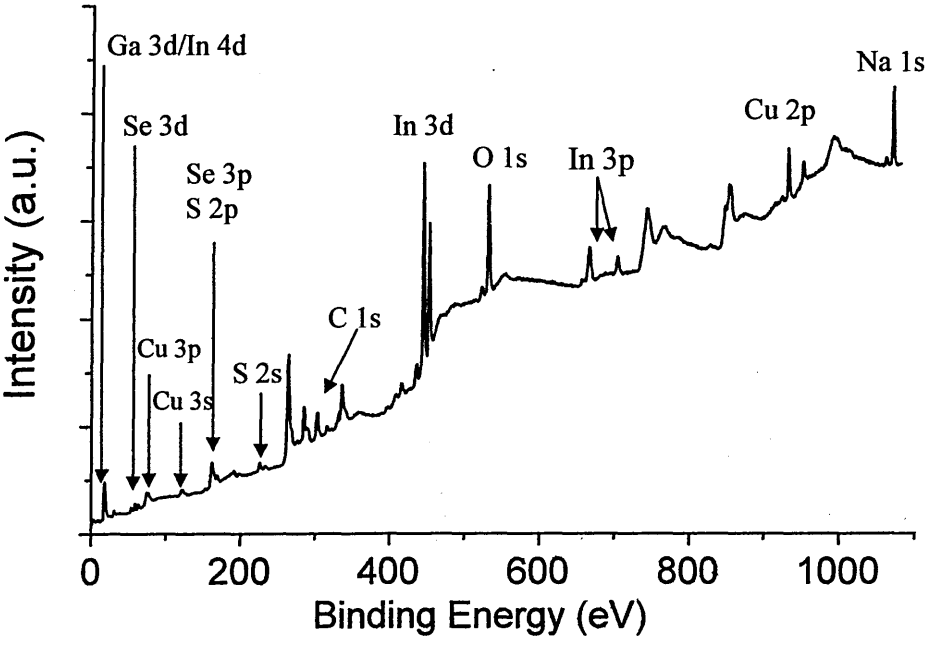

Figure 5.5: XPS survey spectrum of a $Cu(InGa)(SeS)_2$ film grown on a glass/Mo substrate by the two-stage method.

Figure 5.5 shows the XPS survey spectrum of a Cu(InGa)(SeS)$_2$ film grown on a glass/Mo substrate by the two-stage method. One can first observe the presence of copper, indium, selenium and sulphur, as expected. Note that gallium could not be clearly identified. Its most intense lines are at 18.5 eV (Ga 3d), which is very close to the binding energy of the In 4d line and at 1117 eV and 1144 eV (Ga $2p_{3/2}$ and Ga $2p_{1/2}$, respectively), which are outside the detection region of the instrument. The Auger lines are also overlapped by those of other elements, including Na.

The measured ratios of 1.27 for Cu/In and 1.91 for Se/(Cu+In) are both slightly higher than 1.10 and 1.55 respectively as calculated for the bulk. This observation does not support the segregation of Cu-poor phases, such as Cu(InGa)$_3$Se$_5$ or Cu(InGa)$_5$Se$_8$, on the surface of CIGSS films grown by the two-stage method. It is a surprising result regarding the bulk composition of the films and the findings of Nelson et al., who reported the formation Cu(InGa)$_3$Se$_5$ or Cu(InGa)$_5$Se$_8$ on the surface of Cu(InGa)Se$_2$ films grown by physical vapour deposition [11]. On the contrary, Cu-Se phases seem more likely to form on the surface of CIGSS films grown by two-stage method, as the content of indium appears to be lower close to the surface. Raman analysis supports this argument, as a Cu-Se peak was identified on the Raman spectra of CIGSS films.

Two peaks related to carbon and oxygen are also detected and come from the contamination and oxidation of the surface. Note especially the high content of oxygen (67.0 %) when compared with those of copper (7.1 %), indium (5.6 %) and selenium (24.2 %). High oxidation of the surface is related to the long storage period of the samples.

A strong line at about 1072 eV was also detected and attributed to the Na 1s core level. All other peaks are related to Auger emissions.

Atomic composition ratio			
[Cu] (%)	[In] (%)	[Se] (%)	[O] (%)
7.1	5.6	24.2	67.0

Table 5.3: Atomic composition ratio of Cu, In, Se and O on the surface of CIGSS films grown by the two-stage method as calculated from XPS measurements.

The high resolution XPS spectra of the Cu 2p, In 3d and Se 3d core levels of the Cu(InGa)(SeS)$_2$ film are shown in Figure 5.6. One can deduce from these spectra that several phases are present on the surface of the film. Copper seems to be mainly in the

form of Cu_2O, as the Cu 2p peak is closer to the line of Cu_2O than the one of pure copper and a small satellite peak characteristic of Cu_2O seems to emerge at 942 eV. Note, however, that the binding energies of Cu 2p in a Cu-Se matrix (932.4 eV for CuSe and 932.3eV for Cu_2Se) and in CuInSe2 phase (931.9 eV) are very close to the binding energy of Cu 2p in Cu_2O (932.5 eV) [12]. Therefore, what is identified as Cu_2O could well be a mixture of phases, such as $CuInSe_2$, Cu_2O and Cu-Se. It is also hard to confirm that indium is present on the surface of the film in an oxide form, as its peak is located in-between the two lines of pure indium and h^C^. This could suggest that indium is present in both In_{203} and CIGSS phases. The presence of both Se and $SeC_{>2}$ is brought to light by two distinctive peaks at 54 eV and 58.5 eV. Note also the peak at about 63 eV, which is identified as Na 2s. It is not surprising to find Na on the surface of the CIGSS films, as it has been widely observed that it diffused from the soda lime glass, traditionally used as a substrate in photovoltaic devices, through the surface of the films [11, 13]. The presence of Na has also been found to improve the performance of CIS-based solar cells, as already discussed in Section 2.3.2.7.

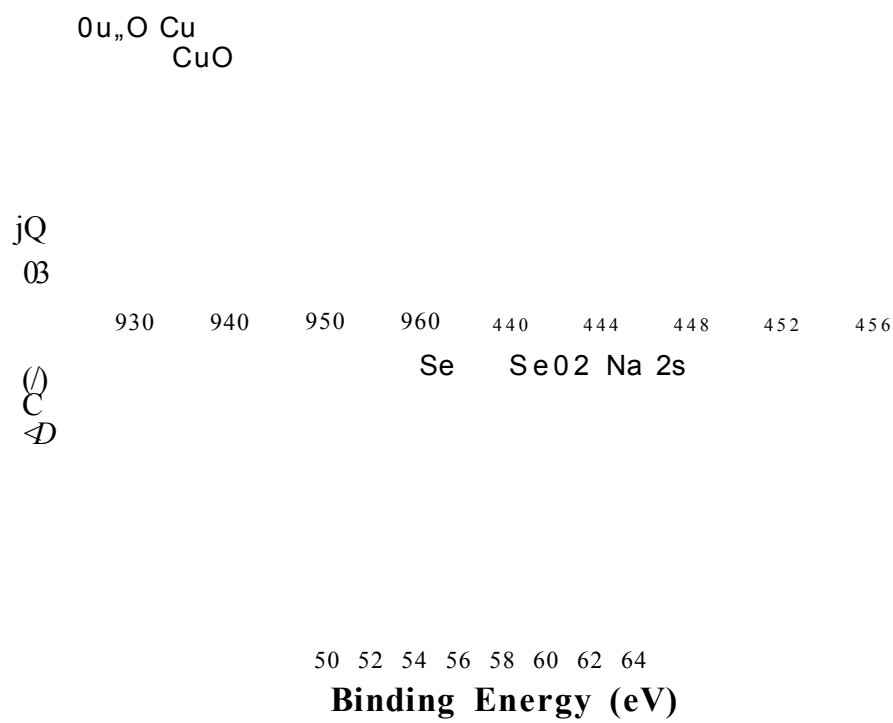

Figure 5.6: **High resolution XPS spectra of the Cu 2p, In 3d, Ga 3d and Se 3d core levels of a Cu(InGa)(SeS)2 film grown on a glass/Mo substrate by the two-stage method.**

5.4.3 Depth profile analysis

As can be seen in the GDOES profile presented in Figure 5.7, CIGSS grown by the two-stage method shows a non-uniform distribution of all the elements within the film, which is to be expected, as the technique of growth involves several steps. In addition, CIGSS grown on Mo is a complex system, which involves 4 metallic elements (Cu, In, Ga and Mo) and 2 non-metallic elements (Se and S). Therefore, different alloys can form with the diffusion in either direction of all these elements due to thermodynamical effects. This can especially happen during the growth, as the two-stage method involves high temperature annealing processes. Thus, it is observed that the CIGSS films contain more copper and gallium near the molybdenum substrate most likely due to the growth of the CuGa precursor layer during the two-stage method.

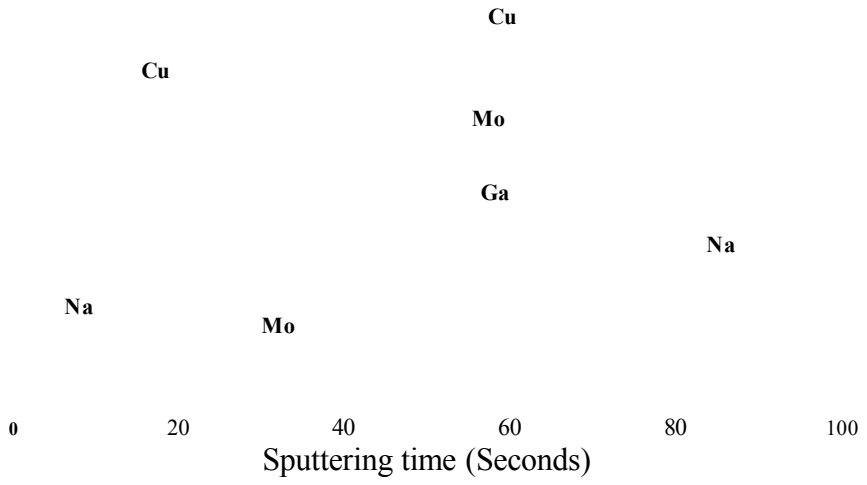

Figure 5.7: GDOES profile of a Cu(InGa)(SeS)2 film grown on a glass/Mo substrate by the two-stage method.

Several humps are also observed probably related to each step of the growth process (deposition of the Cu-Ga alloy and In layers by sputtering, selenisation and sulfidation), which might have led to the formation of well-defined sub-layers within the CIGSS film. It is interesting to note that the surface of the CIGSS samples contains mainly sulphur. However, the sulphur content sharply drops with the samples starting to be sputtered, which suggests that, during the sulfidation process, sulphur covers the $CuInGaSe_2$ top layers but hardly diffuses within the bulk of the material already formed. Selenium and

indium concentrations increase gradually through the surface until reaching the sulphur layer where they drop as do the copper and gallium concentrations. Note that Cu, Ga, Se and S have diffused throughout the molybdenum contact. Overlapping of the Mo signal with Cu, Ga, Se and S can also arise from the roughness of the molybdenum layer. As often reported [13], one can see that sodium has diffused from the soda lime glass substrate through the surface of the films.

5.5 Electrical analysis

Photoelectrochemical measurements were performed to determine the conductivity type of the $Cu(InGa)(SeS)_2$ layers. The electrolyte used for PEC measurements was a 0.1 M KCl aqueous solution. As can be seen in Table 5.4, $Cu(InGa)(SeS)_2$ films show a positive photovoltage demonstrating the p-type character of the material. However, the signal is low when compared with those measured for the window materials (see Chapter 4). This could be due to the photons being absorbed near the film surface in either a dead layer (an absorbing layer with a high recombination rate) or in an n-type layer so that they are not completely transformed into photocurrent. This assumption is supported by the work of Vedel et al. on the photoelectrochemical properties of electrodeposited $CuInSe_2$ [14].

Material	V_{dark} (mV)	V_{light} (mV)	V_{photo} (mV)	Conductivity type
p-Si	-360	-320	+40	p-type
n-Si	-390	-530	-140	n-type
CIGSS	-200	-185	+15	p-type

Table 5.4: Photovoltage produced at the liquid/$Cu(InGa)(SeS)_2$ junction during white light illumination. P- and n-type silicon was used for comparison.

5.6 Summary and conclusions

In this section, $Cu(InGa)(SeS)_2$, films grown by the two-stage method were characterised in order to investigate their structural, morphological, compositional and electrical properties.

XRD shows that CIGSS films are polycrystalline and brings to light the peaks related to the diffraction by the atomic planes (101), (112), (211), (220) or (204), (312) or (116),

(316) or (332) and (424) or (228) of the chalcopyrite structure. The films are preferentially oriented along the <112> axis perpendicular to the substrate.

Raman measurements show the presence of various phases, such as $CuInSe_2$, $CuIn_3Se_5$, $CuInS_2$, $CuIn_5S_8$ and Cu-Se. These phases could not be properly identified by XRD because their XRD patterns are very similar. Another reason could be that XRD is not sensitive enough to detect them due to their amorphous nature.

From SEM and AFM analysis, the films appear dense with a good mechanical adhesion to the molybdenum substrate and show crack-free surfaces with irregular-shaped grains electrically well connected to each other with a size up to 2 μm.

Analysis of the bulk composition shows that XRF results have to be considered with extreme care, as it seems that the In content is underestimated. ICPMS seems to be more reliable and gives an atomic composition ratio Cu:In:Ga:Se = 19.1:17.3:7.1:56.5. The drawbacks of this technique are that it is a destructive technique and the concentration of sulphur cannot be estimated.

From XPS and GDOES analysis, one can see that the distribution of all the elements within the CIGSS films is not uniform. Note also the presence of sodium and native oxides, including Cu_2O, In_2O_3 and SeO_2, on the surface of the films.

Testing of electrical conductivity shows that the films are p-type, although the signal is low, which could be related to the presence of a dead layer or a buried junction near the surface of the films.

5.7 References

[1] Kushiya K., Kuriyagawa S., Kase T., Tachiyuki M., Sugiyama I., Satoh Y., Satoh M., Takeshita H., 25th Photovoltaic Specialists Conference, Washington D.C. (1996) 989.

[2] Kushiya K., Tachiyuki M., Nagoya Y., Fujimaki A., Sang B., Okumura D., Satoh M., Yamase O., Solar Energy Materials and Solar Cells, 67 (2001) 11.

[3] Rincon C., Ramirez F. J., Journal of Applied Physics, 72 (9) (1992) 4321.

[4] Rincon C., Wasim S. M., Marin G., Delgado J. M., Huntzinger J. R., Zwick A., Galibert J., Applied Physics Letters, 73 (4) (1998) 441.

[5] Bacewicz R., Gebicki W., Filipowicz J., Journal of Physics-Condensed Matter, 6 (1994) L777.

[6] Lippold G., Eifler A., Yakushev M. V., Tomlinson R. D., Klenk R., Schock H. W., Grill W., Proceeding of 11th International Conference on Ternary and Multinary Compounds, Institute of Physics Conference Series, 152 (1998) 697.

[7] Álvarez-Garcia J., Marcos-Ruzafa J., Pérez-Rodríguez A., Romano-Rodríguez A., Morante J. R., Scheer R., Thin Solid Films, 361-362 (2000) 208.

[8] Guillen C., Herrero J., Journal of Electrochemical Society, 141 (1) (1994) 225.

[9] Alvarez-García J., Pérez-Rodríguez A., Romano-Rodríguez A., Jawhari T., Morante J. R., Scheer R., Calvet W., Thin Solid Films, 387 (2001) 216.

[10] Schmid D., Ruckh M., Grunwald F., Schock H. W., Journal of Applied Physics, 73 (6) (1993) 2902.

[11] Nelson A. J., Gabor A. M., Contreras M. A., Mason A., Asoka-Kumar P., Lynn K. G., Solar Energy Materials and Solar Cells, 41/42 (1996) 315.

[12] Domashevskaya E. P., Gorbachev V. V., Terekhov V. A., Kashkarov V. M., Panfilova E. V., Shchukarev A. V., Journal of Electron Spectroscopy and Related Phenomena, 114-116 (2001) 901

[13] Ruckh M., Schmid D., Kaiser M., Schäffler R., Walter T., Schock H. W., Solar Energy Materials and Solar Cells, 41/42 (1996) 335.

[14] Vedel J., Thouin L., Lincot D., Journal of Electrochemical Society, 143 (7) (1996) 2173.

Chapter 6: Electrodeposition, characterisation and development of $CuInSe_2$

6.1 Introduction

This section presents the electrodeposition of $CuInSe_2$ and clarifies the influence of the growth parameters on the deposited material layers. The differences between $Cu(InGa)(SeS)_2$ grown by the two-stage method (see Chapter 5) and $CuInSe_2$ grown by electrodeposition will also be examined. The experimental details for the electrodeposition of $CuInSe_2$ will first be given and the results of voltammetry measurements will be used for the determination of the deposition voltage. Then, one will study the structural properties of the electrodeposited CIS materials using x-ray diffraction (XRD) and Raman spectroscopy. The influence of the electrolyte composition will be discussed as well as the deposition voltage and the annealing process. The morphology will then be examined by scanning electron microscopy (SEM) and atomic force microscopy (AFM). The bulk elemental analysis was performed using both x-ray fluorescence (XRF) and inductively coupled plasma mass spectroscopy (ICPMS), as it was shown that XRF did not give the exact composition of the CIS samples. X-ray photoelectron spectroscopy (XPS) and glow discharge optical emission spectroscopy (GDOES) techniques were used for surface analysis and depth profiling respectively. Finally, the conductivity type of the CIS materials will be determined by photoelectrochemical measurements. The main results will be summarised at the end of the chapter.

6.2 Experimental details

The electrodeposition of CIS was carried out using a classical three-electrode potentiostatic system, as described in section 2.4.1.1 using a Gillac ACM instrument, an Ag/AgCl reference electrode, a carbon counter electrode and TCO coated glass substrates as working electrodes. Both ITO and FTO were used as the TCO in this project. The former was preferred to FTO for XRD analysis, as FTO peaks overlap CIS peaks and the latter was used for composition analysis, as ITO contains indium, which enters the composition of $CuInSe_2$ films. The substrates were cleaned thoroughly by refluxing in dichloromethane and washing in acetone followed by distilled water prior to deposition. Aqueous solution for depositing Cu-In-Se layers contained $CuSO_4$, $In_2(SO_4)_3$ and H_2SeO_3. To simplify the discussions involving the composition of the electrolyte, one will consider the reactive species ratio instead of their separate concentrations. Thus, a ratio 1:1:1 will be equivalent to a solution containing 0.2 mM of $CuSO_4$, 0.2 mM of $In_2(SO_4)_3$ and 0.2 mM of H_2SeO_3 and a ratio 2:4:4 will be equivalent to a solution containing 0.4 mM of $CuSO_4$, 0.8 mM of $In_2(SO_4)_3$ and 0.8 mM of H_2SeO_3. In an attempt to deposit $Cu(InGa)Se_2$, $Ga_2(SO_4)_3$ was also added to the electrolyte. The pH was found to be between 2.5 to 2.9 with no added acid to the electrolyte. The temperature of deposition was maintained at 60°C because it was observed that films grown at this temperature were more crystalline than those grown at room temperature. The deposition time was between 40 and 100 minutes. A slow stirring was found to improve the quality of the films. The samples were annealed at elevated temperatures above 200°C in air or nitrogen atmosphere for (15-30) minutes to improve their bulk as well as electrical properties.

6.3 Voltammetry

Figure 6.1 shows the current-voltage characteristics (voltammogram) obtained during the growth of $CuInSe_2$ from an electrolyte containing $CuSO_4$, $In_2(SO_4)_3$ and H_2SeO_3 in the ratio 1:4:4. The voltage scan was between 0 and -1.5 V and the sweep rate was 8 mV/s. As can be seen in Figure 6.1, a plateau current is reached at about -0.2 V related to the co-deposition starting point of Cu, In and Se. A rapid increase in the current density is observed after -0.9 V, which could be related to the deposition of metallic indium or/and hydrogen evolution at the cathode. It will be shown that the composition of the films

varies with the deposition potential. More negative voltages will favour the deposition of indium, which has the lowest electrode potential of the three elements entering the composition of $CuInSe_2$. Electrodeposition was carried out under potentiostatic condition of deposition voltage varying from -0.4 V to -0.9 V.

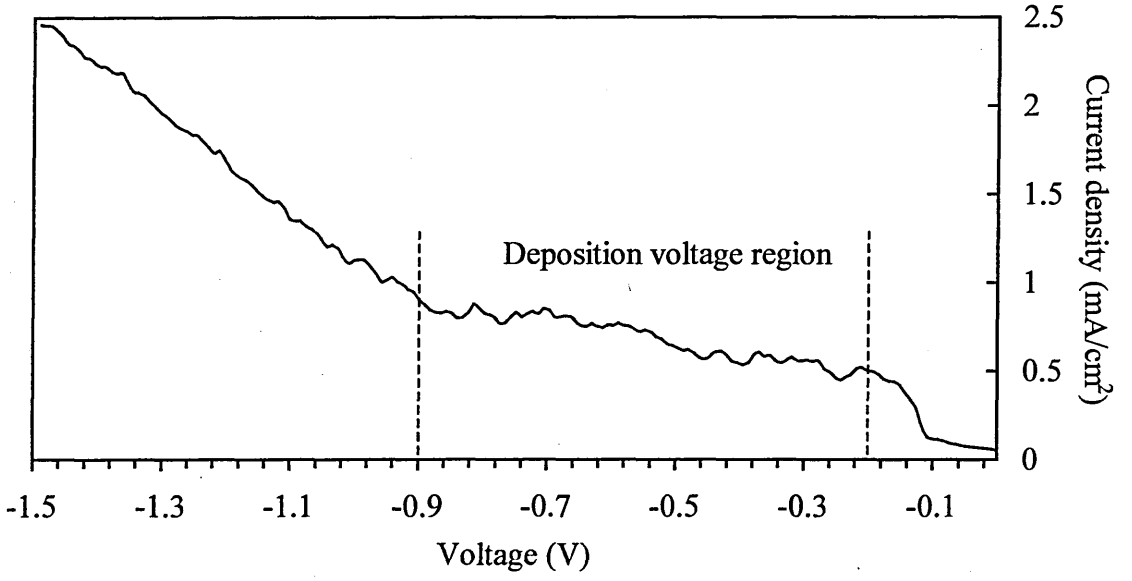

Figure 6.1: Typical voltammogram obtained for an electrodeposition bath containing $CuSO_4$, $In_2(SO_4)_3$ and H_2SeO_3 in the ratio 1:4:4.

6.4 Structural analysis

6.4.1 XRD analysis

XRD studies were carried out in order to identify the composition, crystallinity and phases of the deposited thin films. Since there are three elements in the bath, there are many possibilities to obtain different phases in electrodeposition of $CuInSe_2$. Figure 6.2 shows the influence of the electrolyte composition on the XRD spectra of $CuInSe_2$ layers electrodeposited on glass/ITO. Whatever the composition of the solution, $CuInSe_2$ diffraction peaks associated with the chalcopyrite phase are identified at 2θ angles 26.8°, 44.5° and 52.7°. Note that the peaks identified as $CuInSe_2$ could also be related to $Cu_{2-x}Se$ compounds within the experimental error. As can be seen in Figure 6.2 (a), Cu_2Se peaks clearly appear for low concentrations of $In_2(SO_4)_3$ and H_2SeO_3 in the electrolyte. Similarly, an additional phase of pure selenium is observed in the CIS film grown from an electrolyte containing high concentrations of H_2SeO_3 (see Figure 6.2 (b)).

As shown in Figure 6.2 (c), only the $CuInSe_2$ phase is observed for layers grown from solutions containing $CuSO_4$, $In_2(SO_4)_3$ and H_2SeO_3 in the ratio 1:7.7:1.6. This spectrum is dominated by five peaks corresponding to the diffraction by the atomic planes (112), (220) or (204), (312) or (116), (400) or (008) and (316) or (332) of the chalcopyrite structure. The material also shows a preferential growth with (112) orientation, as generally observed for the films prepared by electrodeposition [1] or the two-stage method (see Section 5.2.1.). Considering the most intense and sharpest peak related to the (112) plane orientation, a grain size of 38.8 nm is estimated using the Scherrer equation given in Section 3.2.1. All other peaks observed arise from the ITO substrate layer.

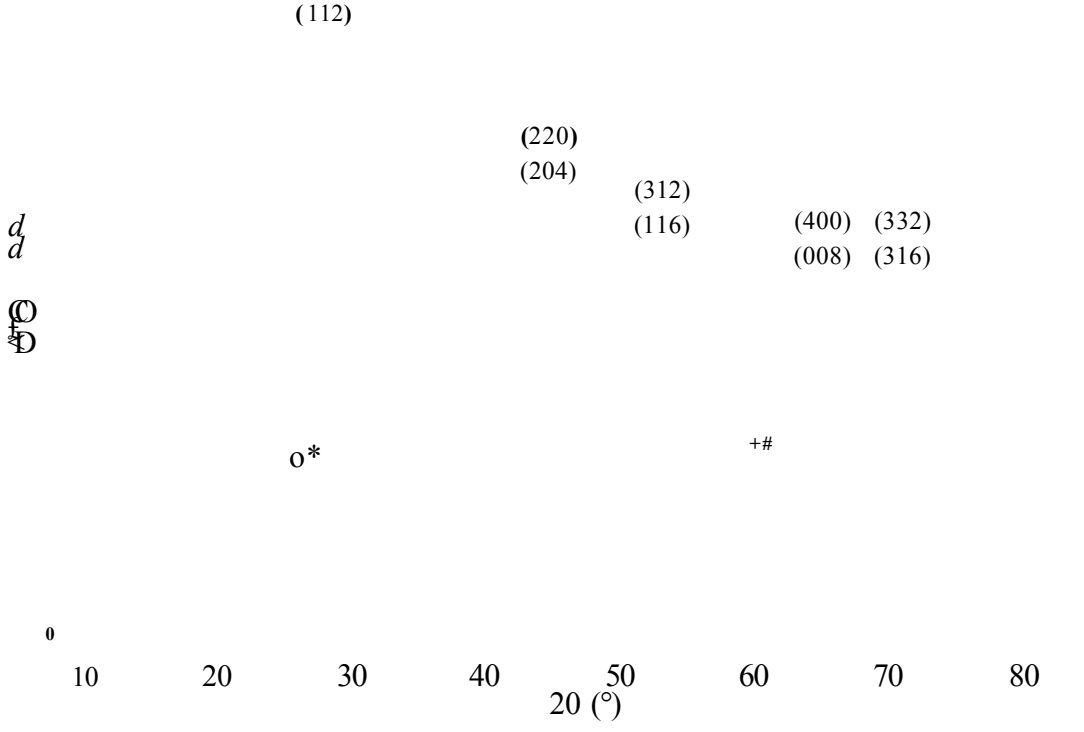

Figure 6.2: XRD spectra of electrodeposited $CuInSe_2$ on glass/ITO substrates prepared at -0.5 V vs Ag/AgCl reference electrode in aqueous solutions containing $CuSO_4$, $In_2(SO_4)_3$ and H_2SeO_3 in the ratio (a) 2.5:4.8:2, (b) 1:7.7:8 and (c) 1:7.7:1.6. The samples were annealed in nitrogen atmosphere at 350°C for 30 minutes.

Figure 6.3 shows the XRD patterns obtained for $CuInSe_2$ electrodeposited on glass/ITO substrates at -0.7 V vs Ag/AgCl reference electrode in aqueous solutions containing $CuSO_4$, $In_2(SO_4)_3$, $Ga_2(SO_4)_3$ and H_2SeO_3 in the ratio 1:4:4:4 before and after annealing. One can first notice that there is no noticeable shift towards higher angles of the XRD

peaks due to the addition of gallium (see Section 2.3.2.6), which means that the content of gallium within the film is negligible. Almost no gallium has been electrodeposited, as it has a very large negative electrode potential ($E^{\circ}_{Ga^{3+}/Ga}$ = -0.73 V vs Ag\AgCl reference electrode) when compared to those of copper ($E^{\circ}_{Cu^{2+}/Cu}$ = 0.135 V vs AgVAgCl reference electrode), indium ($E^{\circ}_{In^{3+}/In}$ = -0.545 V vs Ag\AgCl reference electrode) and selenium ($E^{\circ}_{HSeO_2^+/Se}$ = 0.535 vs Ag\AgCl reference electrode). In addition, $Ga_2(SO_4)_3$ does not dissolve easily in water. One can also observe in Figure 6.3 an improvement in the sharpness and intensity of the $CuInSe_2$ peaks after annealing, which brings to light an improved crystallinity. The estimated crystallite size has increased from 10.4 nm to 42.7 nm after heat treatment. The shoulder on the (112) $CuInSe_2$ peak in the XRD spectrum of the as-deposited sample (Figure 6.3 (a)) has been attributed to an In_2Se_3 secondary phase [2]. This shoulder has disappeared after annealing in nitrogen at 350°C for 30 minutes, which suggests that In_2Se_3 reacts with $CuInSe_2$ during the annealing treatment to form monophasic indium-rich $CuInSe_2$ or an ordered vacancy compound (OVC) of $CuInSe_2$, such as $CuIn_2Se_{3.5}$ or $CuIn_3Se_5$ [2]. One can also assume that Cu_2Se and In_2Se_3 do not completely react to form $CuInSe_2$ during eletrodeposition, the reaction being finished during the heat treatment [1].

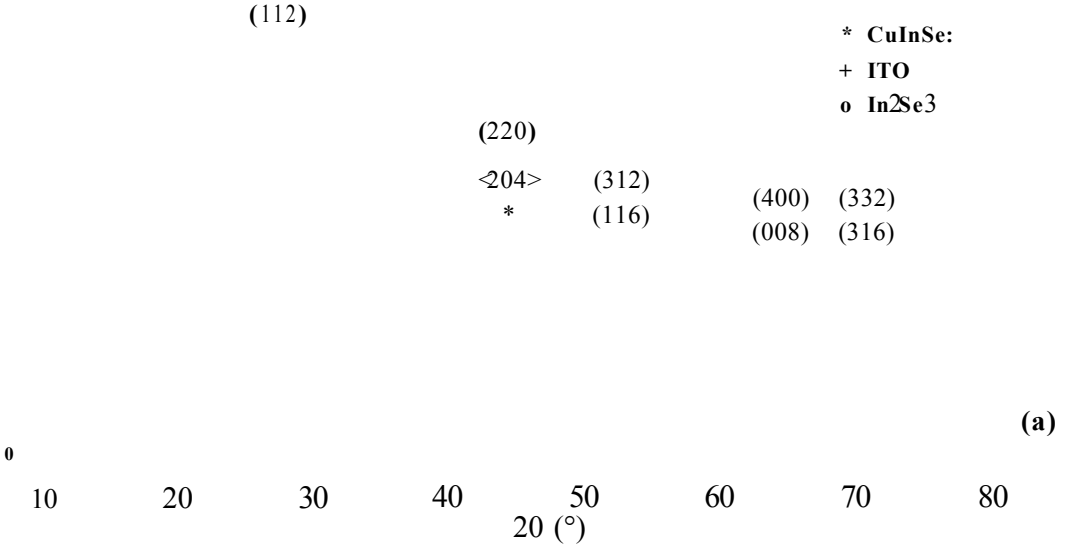

Figure 6.3: **XRD spectra of CuInSe2 electrodeposited on glass/ITO substrates at -0.7 V vs Ag/AgCl reference electrode in an aqueous solution containing CuS04, In2(S04)3, Ga2(S04)3 and H2Se03 in the ratio 1:4:4:4 (a) before and (b) after annealing in nitrogen atmosphere at 350°C for 30 minutes.**

Figure 6.4 shows the XRD patterns obtained for $CuInSe_2$ electrodeposited on glass/ITO substrates at -0.8 V in aqueous solutions containing $CUSO_4$, $In_2(S_{04})_3$, $Ga_2(S_{04})_3$ and H_2Se_{03} in the ratio 1:4:4:4 before and after annealing. One can still observe the improvement in the sharpness and intensity of the diffraction peaks due to the annealing process. However, the peak intensities of the samples grown at -0.8 V are considerably lower than those of $CuInSe_2$ films prepared at -0.7 V. The estimated crystallite size is 7.9 nm for the as-deposited samples and 10.4 nm for the annealed samples. The lower crystallinity of the samples grown at more negative voltages suggests that they contain more indium, as it is generally reported that In-rich $CuInSe_2$ is less crystalline than Cu-rich $CuInSe_2$ [1, 3]. It is noteworthy that the shoulder on the (112) $CuInSe_2$ peak has not disappeared after annealing indicating an excess of In_2Se_3.

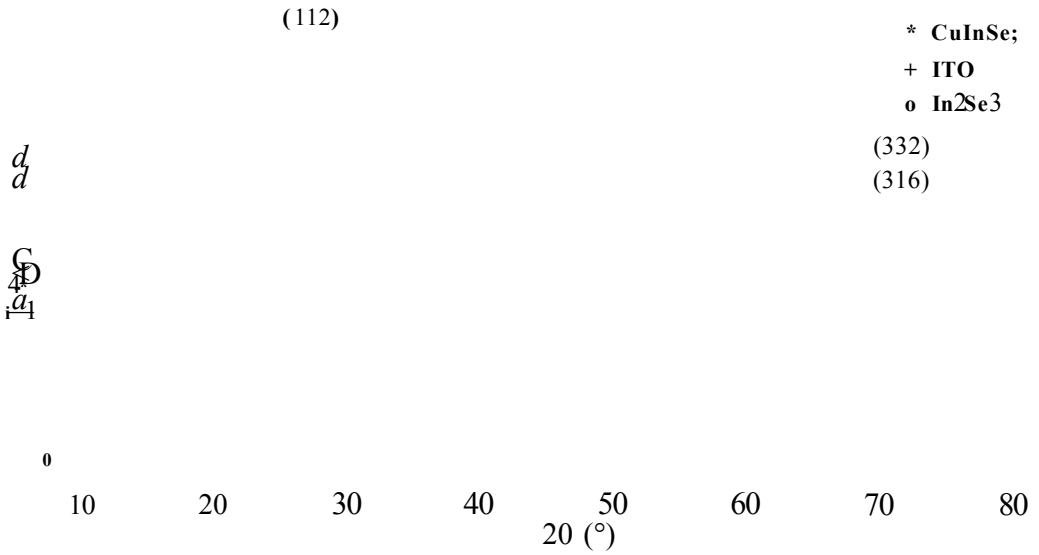

Figure 6.4: XRD spectra of $CuInSe_2$ electrodeposited on glass/ITO substrates at -0.8 V vs Ag/AgCl reference electrode in an aqueous solution containing $CuS04$, $In_2(S04)3$, $Ga_2(S0_4)_3$ and H_2Se0_3 in the ratio 1:4:4:4 (a) before and (b) after annealing in nitrogen atmosphere at 350°C for 30 minutes.

It is difficult to confirm the phases present within the material layers only from the XRD analysis because the peaks of different compounds, such as $CuInSe_2$, $Cu_{2-x}Se$ or $Cuki_2Se_{3.5}$, can overlap, as it has been already discussed. For further investigations of these phases, Raman experiments were carried out and the results are discussed in Section 6.4.2.

6.4.2 Raman analysis

Raman experiments were performed in order to understand the influence of the deposition voltage on the electrodeposition of $CuInSe_2$ thin fdms. Figure 6.5 shows the Raman spectra of electrodeposited $CuInSe_2$ on glass/FTO substrates prepared at various deposition voltages in aqueous solutions containing Q_1SO_4, $In_2(S_{04})_3$, $Ga_2(S_{04})_3$ and H_2Se_{03} in the ratio 1:4:4:4. The three peaks related to $CuInSe_2$ observed for $Cu(InGa)(SeS)_2$ grown by the two-stage method (see Section 5.2.2) are also detected at 176 cm'1, 212 cm^{-1} and 228 cm'1. As already mentioned, the peak at 176 cm^{-1} corresponds to the A1 mode resulting from the motion of the Se atom with Cu and In atoms remaining at rest and the peaks at 212 cm^{-1} and 228 cm^{-1} are due to the B2 and E modes, which correspond to the combined motion of all the atoms [4].

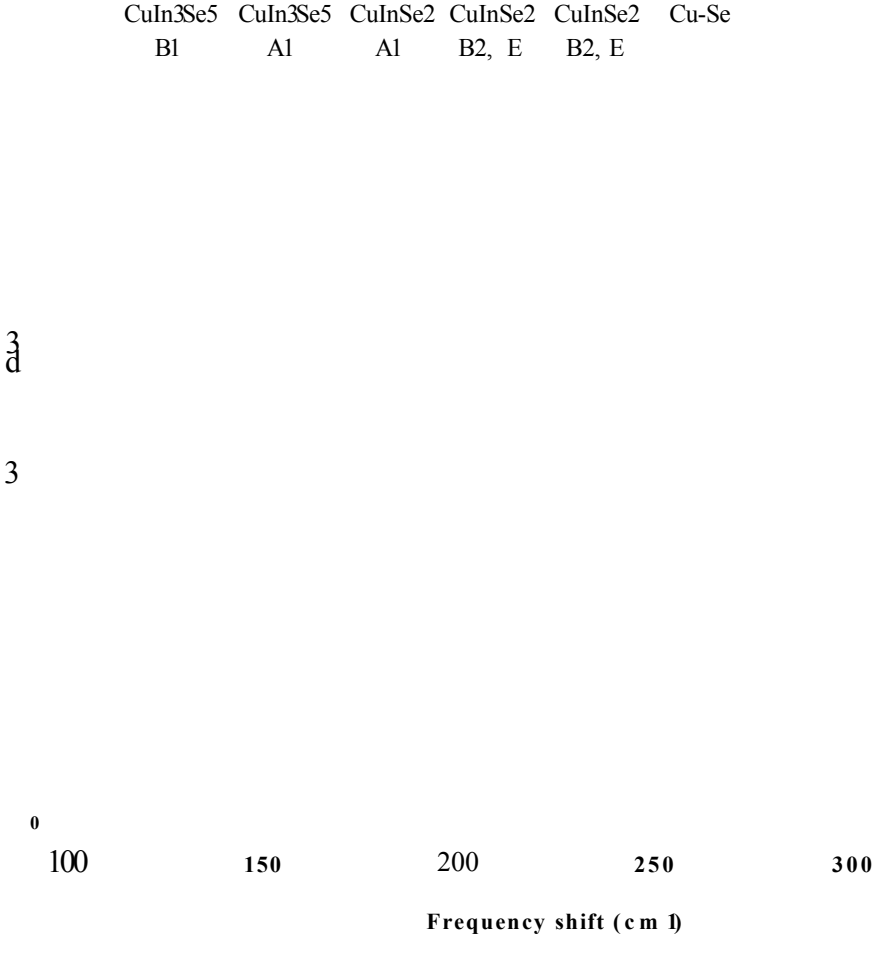

Figure 6.5: **Raman spectra of electrodeposited $CuInSe_2$ on glass/FTO substrates prepared at various deposition voltages in aqueous solutions containing $CuSO_4$, $In_2(SO_4)_3$, $Ga_2(SO_4)_3$ and H_2SeO_3 in the ratio 1:4:4:4.**

Whatever the deposition voltage used to grow the films, a shoulder on the A1 mode peak of $CuInSe_2$ at 152 cm^{-1} is observed. As for $Cu(InGa)(SeS)_2$ grown by the two-stage method, this peak has been attributed to the A1 mode of the ordered vacancy compound $CuIn_3Se_5$. The small and broad peak at about 132 cm^{-1} is believed to be the B1 mode of $CuIn_3Se_5$ [5]. It is surprising to observe this phase in all the samples, as it is believed to appear only in In-rich $CuInSe_2$ materials. One can also see in Figure 6.5 that the peak at 260 cm^{-1} related to Cu-Se, according to Lippold et al. [6], and observed for $Cu(InGa)(SeS)_2$ grown by the two-stage method, completely disappears for the layers grown at potentials more negative than -0.7 V. This observation can explain why the shoulder on the (112) XRD peak of the $CuInSe_2$ films grown at -0.8 V does not disappear after annealing, as In_2Se_3 cannot further react with Cu-Se to form $CuInSe_2$. It is noteworthy that the Cu-Se phase reappears in the Raman spectra of films grown at very low deposition voltages (-1 V). At these voltages, the deposition is very fast and hydrogen evolution is important, which results in the production of powdery films not well adhesive to the substrate, as will be shown by SEM. These layers are not suitable for device fabrication and could possibly contain a mixture of different alloys, including Cu-Se.

6.5 Morphological analysis

6.5.1 SEM analysis

SEM was performed to study the surface morphology of the $CuInSe_2$ layers grown by the technique of electrodeposition. Samples were mounted on metal stubs using silver conducting paste. Silver paste was also used to form a conducting path between the semiconducting layers and the metal stub. This prevented excessive charging of the samples. A spot size setting between 2 and 5 and an accelerating voltage of 20 kV were found to produce good micrographs.

Figures 6.6 (a) and (b) show the surface morphology of a CIS layer grown on a glass/ITO substrate at -0.5 V versus Ag/AgCl reference electrode in an aqueous solution containing $CuSO_4$, $In_2(SO_4)_3$ and H_2SeO_3 in the ratio 1:7.7:1.6. This layer shows a crack-free surface with long and narrow grains. The XRD pattern obtained for this material layer showed sharp and intense peaks indicating the presence of a polycrystalline CIS phase but Raman analysis also demonstrated the presence of a secondary Cu-Se phase.

Figures 6.6 (c) and (d) show the surface morphology of a CIS film incorporating more indium and selenium in the material. There is a clear difference in the surface morphology of these materials, which contain small spherical grains uniformly distributed on the surface. SEM studies therefore help to distinguish between Cu-rich CIS layers containing Cu-Se secondary phases and more stoichiometric $CuInSe_2$ ternary compounds. These observations are in agreement with the SEM results reported by Bhattacharya et al. for Cu-Se and Cu-In-Se phases [7].

(c) **(d)**

Figure 6.6: SEM micrographs of electrodeposited $CuInSe_2$ films on glass/ITO substrates prepared in aqueous solutions containing $CuSO_4$, $In_2(SO_4)_3$ and H_2SeO_3 in the ratio: (a) 1:7.7:1.6 (at -0.5 V vs Ag/AgCl electrode) for magnications x 3000 and (b) x 6000; (c) 1:4:4 (at -0.8 V vs Ag/AgCl electrode) for magnications x 3000 and (d) x 8000.

In Figure 6.7 are displayed the SEM micrographs of $CuInSe_2$ films grown on glass/FTO in an aqueous solution containing $CuSO_4$, $In_2(SO_4)_3$, $Ga_2(SO_4)_3$ and FESeOs in the ratio 1:4:4:4. Note that there is no major difference between the morphology of the layers grown at -0.8 V with $Ga_2(SO_4)_3$ into the bath (Figure 6.7 (c)) and without $Ga_2(SO_4)_3$ into the bath (Figure 6.6 (c)), which confirms that Ga hardly electrodeposits. Figures 6.7 (a)

and (b) show the influence of the annealing step process on as-deposited $CuInSe_2$. One can thus observe that the particle size has increased from about 0.6 to 1.1 μm after annealing the layer in nitrogen atmosphere at 350°C for 30 minutes. However, it is worth mentioning that this increase in the grain size is not always discernable, especially for the films grown at voltages below -0.7 V. The increase in the grain size could therefore be related to the formation of larger grains of $CuInSe_2$ from the reaction between Cu-Se and In-Se secondary phases. Films deposited at high negative voltages do not show an increase in the grain size related to the heat treatment, as Cu-Se is not present anymore in the material (see Raman results in Section 6.4.2).

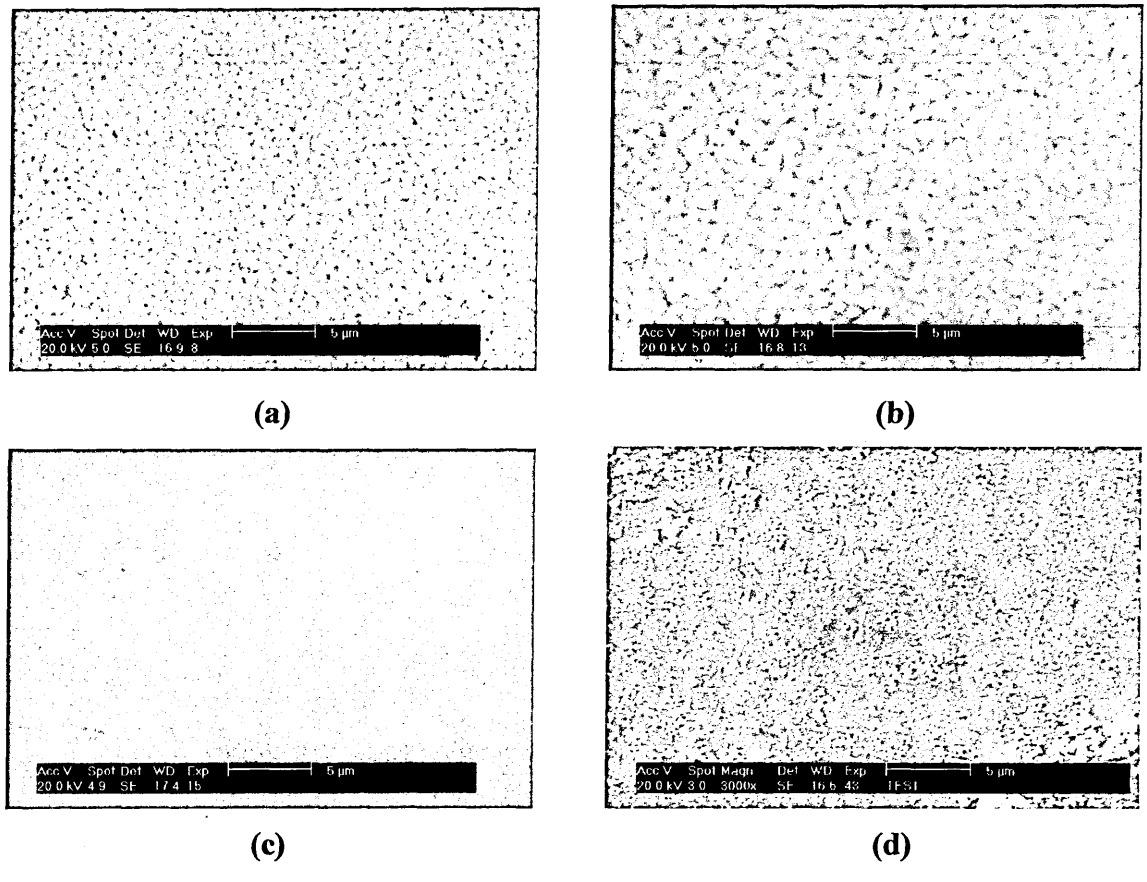

Figure 6.7: SEM micrographs of electrodeposited $CuInSe_2$ films on glass/FTO substrates grown in aqueous solutions containing $CuSO_4$, $In_2(SO_4)_3$, $Ga_2(SO_4)_3$ and H_2SeO_3 in the ratio 1:4:4:4 at -0.6 V (a) before and (b) after annealing in nitrogen atmosphere at 350°C for 30 minutes, (c) -0.8 V and (d) -1 V.

Note the large difference between the grain size estimated from XRD and the one obtained from SEM. The crystal size calculated using the Scherrer equation is more than 20 times smaller than the one estimated from the SEM micrographs. This is probably

because the particles in the films seen in the SEM pictures are not real crystallites, as detected by XRD, but consist of groups of small crystals. As already discussed, the difference can also come from the broadening of the diffractometer and the micro-strain, which increase the width of the XRD peaks and therefore lead to an underestimation of the grain size. It is interesting to compare the SEM micrographs of films grown at different deposition voltages. One can remark a decrease in the particle size of the films grown at -0.8 V (Figure 6.7 (c)) when compared to those grown at -0.6 V (Figure 6.7 (a)). This is in agreement with the XRD observation that films grown at more negative deposition voltages are less crystalline. The films deposited at -1 V were neither well adhesive to the substrate nor uniform, as shown in Figure 6.7 (d), which can be due to a strong hydrogen evolution at the cathode or/and a too-fast deposition process or/and the co-deposition of different phases, such as pure indium in addition to $CuInSe_2$.

6.5.2 AFM analysis

The surface morphology of the electrodeposited films was also examined by AFM using the contact mode and a very low frequency of 0.5 Hz.

The polycrystalline nature of the samples can be seen from the large number of $CuInSe_2$ grains in the field of view (Figure 6.8 (a)). In order to make high-efficiency $CuInSe_2$-based solar cells, it is crucial to grow compact $CuInSe_2$ films, which prevents the diffusion of metal from the back contact during evaporation through the semiconducting layers. This can be achieved by electrodeposition, as illustrated in Figure 6.8, representing the 2-D and 3-D images on different scan areas of a $CuInSe_2$ film electrodeposited on glass/ITO. The layers are uniform and formed of platelets orientated along the same direction with an average size of approximately 1 μm. Note the difference between the long grains observed by AFM and those more spherical observed by SEM (see Figure 6.6 (d)). This dissimilarity has not yet been fully understood. It can also be seen from the high-resolution 3-D view image (Figure 6.8 (d)) that the surface of the film is smooth and the grains are electrically well connected to each other. The surface roughness calculated using a root mean square (rms) value function is 9.3 nm on a 2.5 x 2.5 μm^2 scan area. Note that the $CuInSe_2$ films grown by electrodeposition are less rough than the $Cu(InGa)(SeS)_2$ layers grown by the two-stage method, as expected.

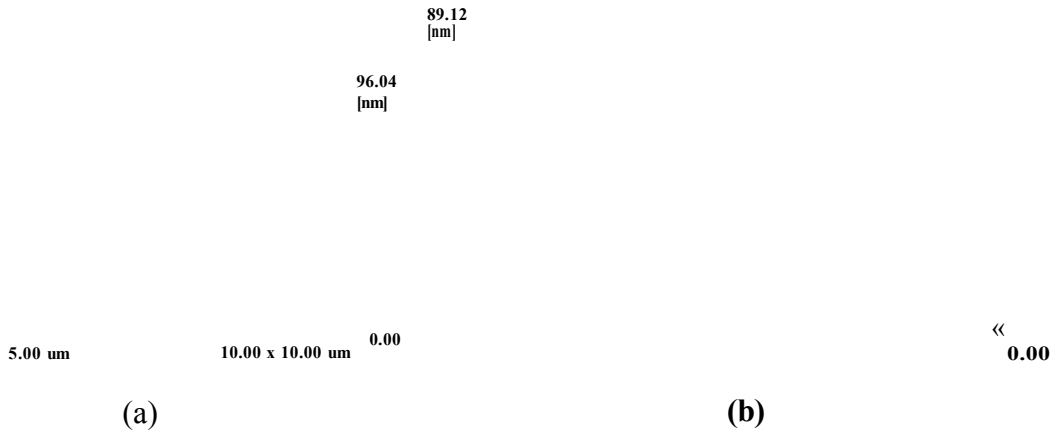

Figure 6.8 : AFM pictures of a $CuInSe_2$ film on a glass/ITO substrate electrodeposited at -0.8 V vs Ag/AgCl reference electrode in an aqueous solution containing $CuSO_4$, $In_2(SO_4)_3$, $Ga_2(SO_4)_3$ and H_2SeO_3 in the ratio 1:4:4:4: (a) plane view (low magnification), (b) 3-D view (low magnification), (c) plane view (high magnification) and (d) 3-D view (high magnification).

In Figure 6.9 are displayed the AFM images of a $CuInSe_2$ film electrodeposited on a glass/ITO substrate at -0.8 V vs Ag/AgCl electrode in an aqueous solution containing $CuSO_4$, $In_2(SO_4)_3$, $Ga_2(SO_4)_3$ and H_2SeO_3 in the ratio 1:4:4:4 after annealing in nitrogen at 350°C for 30 minutes. One can notice an increase in the grain size due to the annealing process, as already observed by SEM. As can be seen in the 3-D imaging, the prominent spikes correspond to the small dots seen in Figures 6.9 (a) and (c). These spikes do not seem to come from the annealing step, as they were sometime observed in non-annealed samples.

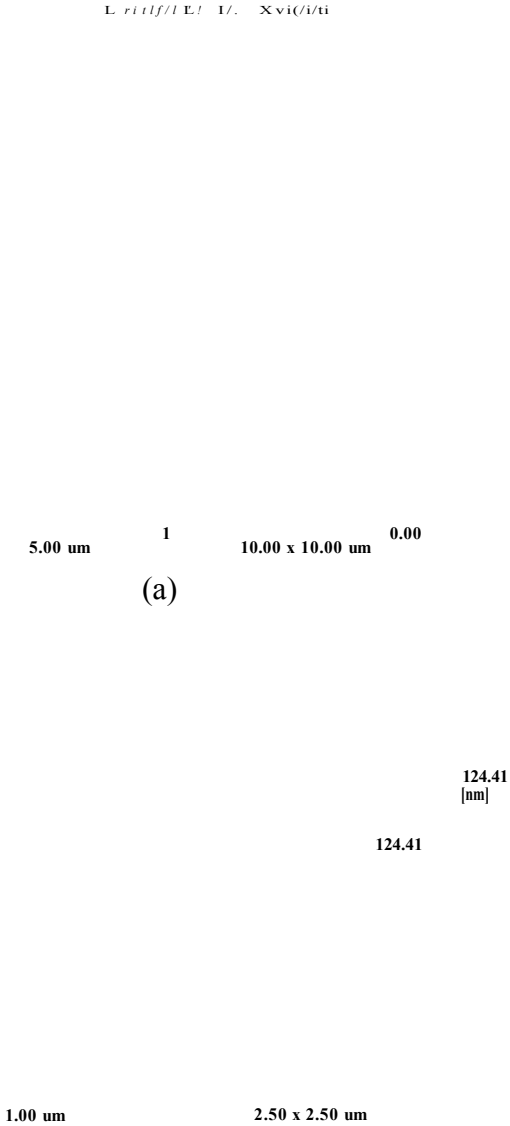

Figure 6.9: AFM pictures of a $CuInSe_2$ film on a glass/ITO substrate electrodeposited at -0.8 V vs Ag/AgCl reference electrode in an aqueous solution containing $CuSO_4$, $In_2(SO_4)_3$, $Ga_2(SO_4)_3$ and H_2SeO_3 in the ratio 1:4:4:4 after annealing in nitrogen at 350 °C for 30 minutes: (a) plane view (low magnification), (b) 3-D view (low magnification), (c) plane view (high magnification) and (d) 3-D view (high magnification).

6.6 Compositional analysis

6.6.1 Bulk analysis

The bulk compositional analysis of the electrodeposited CIS films was performed using the two techniques of x-ray fluorescence (XRF) and inductively coupled plasma mass spectrometry (ICPMS). As already discussed in Section 5.4.1, the two techniques do not give exactly the same results.

Table 6.1 shows the percentage ratio of copper, indium and selenium atoms of various material layers electrodeposited from electrolytes with different compositions. It can be

seen that the electrolyte composition influences the atomic concentrations of copper, indium and selenium present in the material layers. The main conclusions are that the decrease of the $CuSO_4$:H_2SeO_3 ratio in the electrolyte leads to enriched-Se films, as expected. Note that the indium content remains low, which indicates the possible formation of copper selenide phases, such as Cu_2Se, in addition to $CuInSe_2$. From XRF measurements, it can also be seen that annealing of Se-rich $CuInSe_2$ films give rise to a loss of selenium, as generally observed [8].

For comparison, XRF results obtained on bulk crystals of $CuInSe_2$ grown by the vertical Bridgman technique are also shown in the table. It is revealed that these samples were also indium deficient, although their compositions were expected to be very close to stoichiometry. This indicates that the absolute values given by these measurements should be treated with extreme care due to the different sensitivity of the elements involved in the analysis, as already discussed in Section 5.4.1.

$CuSO_4$:$In_2(SO_4)_3$:H_2SeO_3 ratio in the electrolyte	Post annealing condition	Atomic composition of CIS material		
		[Cu] (%)	[In] (%)	[Se] (%)
1:7.7:1.6	As deposited	49.1	6.3	44.6
1:80:6.5	As deposited	22.6	7.6	69.8
1:100:8	As deposited	15.2	6.5	78.3
1:100:8	Annealed in nitrogen at 350°C for 30 min.	21.9	8.5	69.6
Melt grown bulk CIS sample		25.0	15.0	60.0

Table 6.1: XRF results of various electrodeposited $CuInSe_2$ layers grown at -0.5 V vs Ag/AgCl reference electrode on glass/FTO substrates from electrolytes with different compositions. A benchmark CIS sample grown by the vertical Bridgman technique was used for comparison.

XRF experiments were also performed in order to understand the influence of the deposition voltage on the composition of $CuInSe_2$ thin films. Figure 6.11 shows the percentage composition of copper, indium, gallium and selenium atoms of various material layers electrodeposited on glass/FTO substrates at different deposition voltages in an aqueous solution containing $CuSO_4$, $In_2(SO_4)_3$, $Ga_2(SO_4)_3$ and H_2SeO_3 in the ratio 1:4:4:4. One can see that the deposition voltage also controls the atomic concentrations of copper, indium, gallium and selenium present in the material layers. Cu and Se contents in the film gradually decrease while the In concentration increases with reducing the deposition voltage from -0.6 V to -1 V. This result is expected, as the electrode potential of indium ($E^0_{In^{3+}/In}$ = -0.545 V vs Ag\AgCl reference electrode) is

more negative than those of copper $E^{\circ}_{Cu^{2+}/Cu}$ = 0.135 V vs Ag\AgCl reference electrode) and selenium ($E^{\circ}_{H_2Se/Se}$ = 0.535 vs Ag\AgCl reference electrode). The increase of the indium content at the expense of copper when the films are deposited at -0.5 V has not yet been fully understood. Note that the gallium content remains very low whatever the deposition voltage with a small increase for the films deposited at -1 V. This result is not surprising, as the electrode potential of gallium is very negative ($E^{\circ}_{Ga^{3+}}$ = -0.73 V vs Ag\AgCl reference electrode) when compared to those of copper, indium and selenium. In addition, $Ga_2(SO_4)_3$ does not dissolve easily in water. This observation explains why there is no shift of the $CuInSe_2$ XRD peaks towards higher angles related to the addition of gallium.

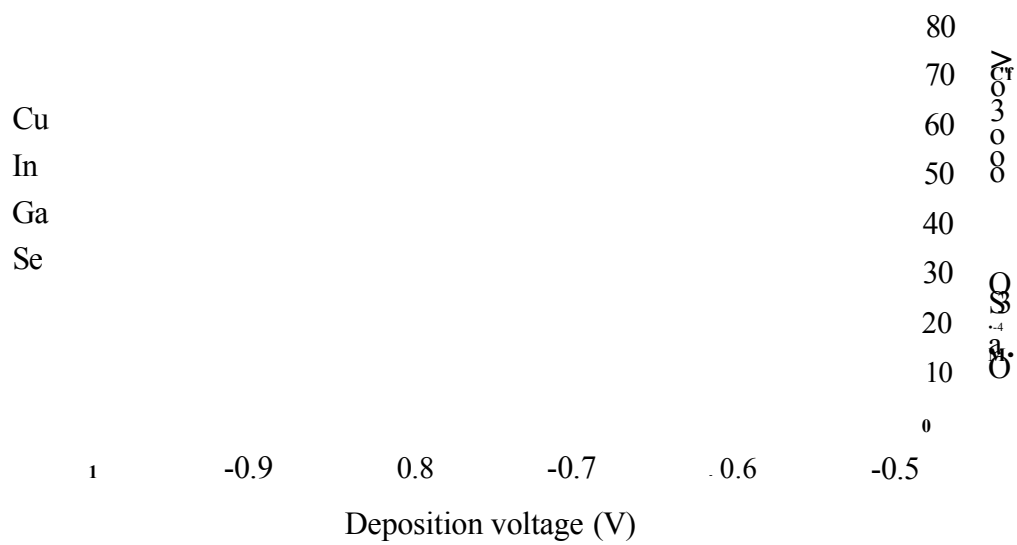

Figure 6.11: Atomic composition ratio as calculated from XRF measurements of various $CuInSe_2$ films electrodeposited on glass/FTO at different deposition voltages (vs Ag/AgCl reference electrode) in an aqueous solution containing $CuSO_4$, $In_2(SO_4)_3$, $Ga_2(SO_4)_3$ and H_2SeO_3 in the ratio 1:4:4:4.

ICPMS measurements were performed in order to check the validity of the XRF measurements, as it was demonstrated in Section 5.4.1 that XRF might not give the exact composition of the films. For this purpose, $CuInSe_2$ layers were dissolved in nitric acid. A blank sample was run in-between each measurement to prevent the contamination from one measurement to the next one.

It can be seen in Figure 6.12 the influence of the deposition voltage on the composition of deposited CIS films using the same samples studied by XRF. Similar results are obtained, although the atomic percentage of copper, indium and selenium are different. Thus, one can observe an increase in the In-ratio at the expense of the Cu- and Se-ratios. It seems that near stoichiometric $CuInSe_2$ films can be grown at deposition voltages around -0.7 V.

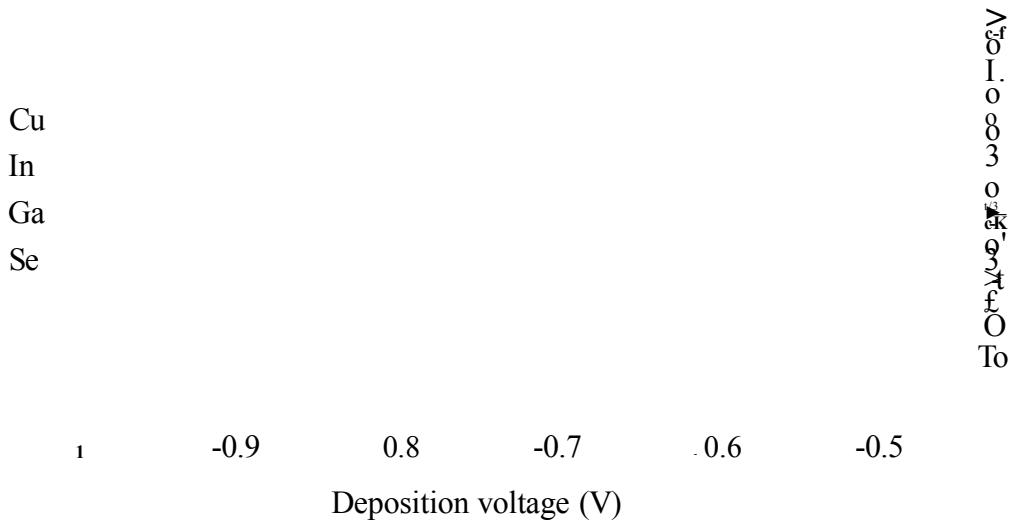

Figure 6.12: Atomic composition ratio as calculated from ICPMS measurements of various $CuInSe_2$ films electrodeposited on glass/FTO at different deposition voltages (vs Ag/AgCl reference electrode) in an aqueous solution containing $CuSO_4$, $In_2(SO_4)_3$, $Ga_2(SO_4)_3$ and H_2SeO_3 in the ratio 1:4:4:4.

6.6.2 Surface analysis

XPS was carried out in order to examine the surface (~30 A) composition of the deposited films, which would be expected to vary from the bulk composition due to the segregation of various phases, as already discussed in Section 2.3.2.2. XPS analysis was performed on a VG ESCALAB II using Mg K« (1253.6 eV) radiation. Since the material layers are grown on glass/FTO substrates, silver paste was used to form a conducting path between the semiconducting layers and the metal stub. One has to refer to Section 5.4.2 reporting the XPS results of CIGSS grown by the two-stage method for more experimental details.

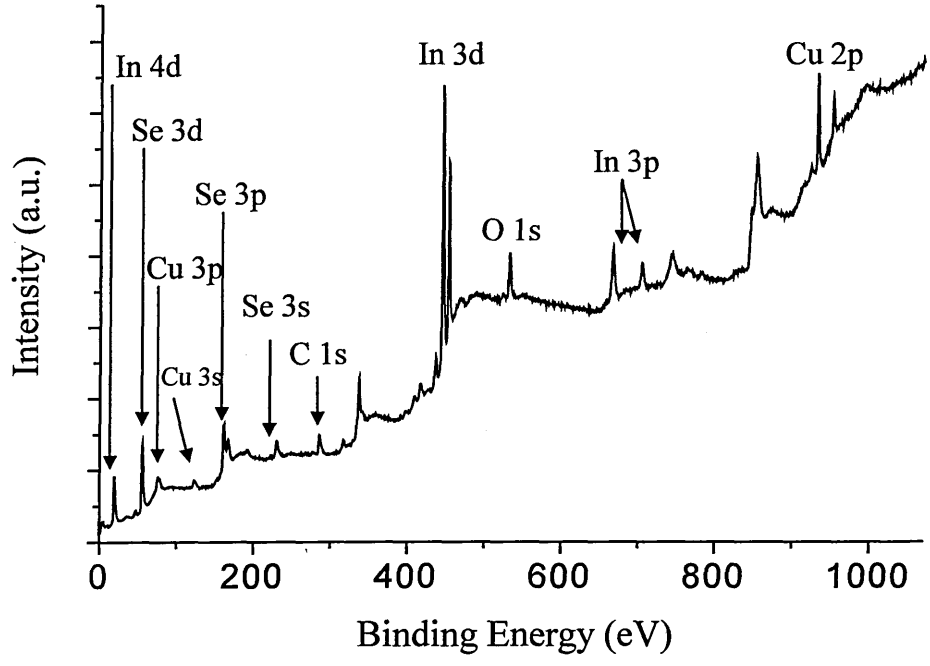

Figure 6.13: XPS survey spectrum of $CuInSe_2$ grown on glass/FTO substrate by electrodeposition at -0.8 V vs Ag/AgCl reference electrode in an aqueous solution containing $CuSO_4$, $In_2(SO_4)_3$, $Ga_2(SO_4)_3$ and H_2SeO_3 in the ratio 1:4:4:4 after annealing in nitrogen atmosphere at 350°C for 30 minutes.

Figure 6.13 shows the XPS survey spectrum of $CuInSe_2$ grown by electrodeposition. One can first observe the presence of copper, indium and selenium, as expected. Gallium could not clearly be identified for similar reasons to those given in Section 5.4.2. Nevertheless, considering the very low content of gallium in the bulk material (see ICPMS results in Section 6.6.1), it is believed that this element is not present or not very abundant on the surface of the electrodeposited films.

Note also the low content of copper (9.5 %) when compared to those of indium (32.2 %) and selenium (31.1 %). This could be due to the formation of In-rich phases, such as $CuIn_3Se_5$ or $CuIn_5Se_8$ generally observed on the surface of Cu-depleted CIS materials [9]. Raman analysis supports this argument, as $CuIn_3Se_5$ was identified. Another explanation could be that copper does not easily form oxides so that it hardly diffuses through the surface to oxidise. On the other hand, indium easily forms In_2O_3, as its standard molar enthalpy of formation is very low ($\Delta_f H^0$ = -925.8 kJ.mol^{-1} [10]). Table 6.4 reports the standard molar enthalphies of formation of possible native oxides present on the surface of the CIS films.

Two peaks related to carbon and oxygen are detected and come from the contamination and oxidation of the surface. All other peaks are related to Auger emissions. Note that the strong line at about 1072 observed in the XPS spectrum of CIGSS grown by the two-stage method and attributed to the Na 1s core level does not appear here. This suggests that there is no diffusion of sodium from the soda lime glass to the surface of the film during the growth of $CuInSe_2$ by electrodeposition or even during the heat treatment at 350°C. This is probably due to the fact that the temperatures involved in the development of CIS films by electrodeposition are relatively low when compared to those involved in the growth of CIGSS by the two-stage method (temperatures above 500°C).

Atomic composition ratio			
[Cu] (%)	[In] (%)	[Se] (%)	[O] (%)
9.5	32.2	31.0	18.4

Table 6.3: Atomic composition ratio as calculated from XPS measurements of Cu, In, Se and O on the surface of a $CuInSe_2$ film grown on glass/FTO by electrodeposition at -0.8 V vs Ag/AgCl reference electrode in an aqueous solution containing $CuSO_4$, $In_2(SO_4)_3$, $Ga_2(SO_4)_3$ and H_2SeO_3 in the ratio 1:4:4:4 after annealing in nitrogen atmosphere at 350°C for 30 minutes.

	CuO	Cu_2O	In_2O_3	Ga_2O	Ga_2O_3	SeO_2
$\Delta_f H^0$ (kJ.mol^{-1})	-157.3	-168.6	-925.8	-356.0	-1089.1	-225.3

Table 6.4: Standard molar enthalphies of formation at 298 K of possible native oxides present on the surface of the CIS films [10, 11].

In Figure 6.14 are displayed the high-resolution XPS spectra of the Cu 2p, In 3d and Se 3d core levels of $CuInSe_2$. The binding energy of a particular core level peak is dependent on the chemical and electrical environment encountered by the emitting atom. If a change in the environment of the emitting atom occurs, the binding energy of the core level emission peak will also change with the difference in energy being described as a shift. This can explain the shift towards higher energy (~1 eV) observed for the Cu 2p, In 3d and Se 3d core level peaks. One cause of this shift could be the band bending, which results from the presence of surface states. This is an electronic effect and occurs due to the transfer of charges at the surface, as described in Section 2.2.3. The band bending occurs within a region known as the depletion region. This depletion region is usually much larger than the sampling depth of the photoemission and hence all the detected core level electrons are subjected to the band bending with a subsequent shift in

the core level peaks. Another obvious explanation to this shift is that the atoms are not isolated but embedded in a CIS matrix, which can change their core level peak position. The fact that the XPS peaks are shifted towards higher energies when compared to those of CIGSS grown by the two-stage method could be explained by the presence of CuInsSes, as it has been shown that the binding energies in $CuIn_3Se_5$ are higher than those in $CuInSe_2$ [12]. The broadening of the peaks observed for the Cu 2p, In 3d and Se 3 d core levels of $CuInSe_2$ is partly due to the spin orbit splitting related to the coupling of the orbital and spin angular momenta of the electrons but also to the instrumental broadening.

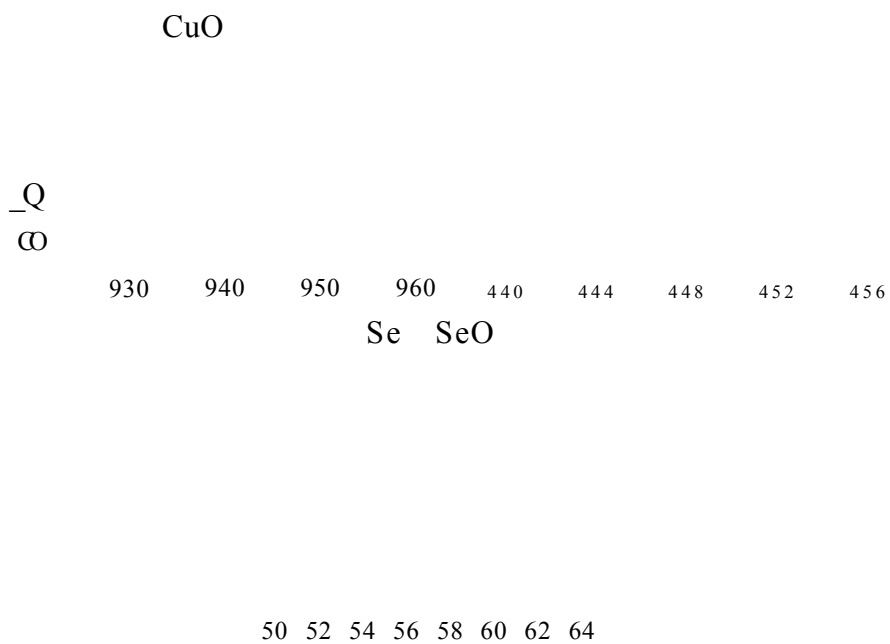

Figure 6.14: High resolution XPS spectra of the Cu 2p, In 3d and Se 3d core levels of $CuInSe_2$ grown on glass/FTO by electrodeposition at -0.8 V vs Ag/AgCl reference electrode in an aqueous solution containing $CuSO_4$, $In_2(SO_4)_3$, $Ga_2(SO_4)_3$ and H_2SeO_3 in the ratio 1:4:4:4 after annealing in nitrogen atmosphere at 350°C for 30 minutes.

From these spectra, one can see that copper and selenium do not seem to have formed oxides on the surface of the electrodeposited films, contrary to CIGSS layers grown by the two-stage method. The lower oxidation of the electrodeposited film surface is mainly related to the shorter storage period. Note, however, that indium seems to be mainly in the form of fti_{203}, as the In 3d peak is closer to the fti_{203} line than the In line. The

preferential formation of In_2C_3 could be due to its very low standard molar enthalpy of formation ($\Delta_f H° = -925.8$ kJ.mol'1). One has, however, to keep in mind that the presence of In embedded in a $CuIn_3Se_5$ matrix could also be responsible for the shift of the In 3d peak towards higher energy. Therefore the presence of $CuIn_3Se_5$ cannot be omitted, especially since this phase has also been observed in the Raman spectra of electrodeposited films.

6.6.3 Depth Profile analysis

GDOES profiling experiments were performed on electrodeposited $CuInSe_2$ films and Figure 6.15 shows a typical depth profile obtained for an annealed sample.

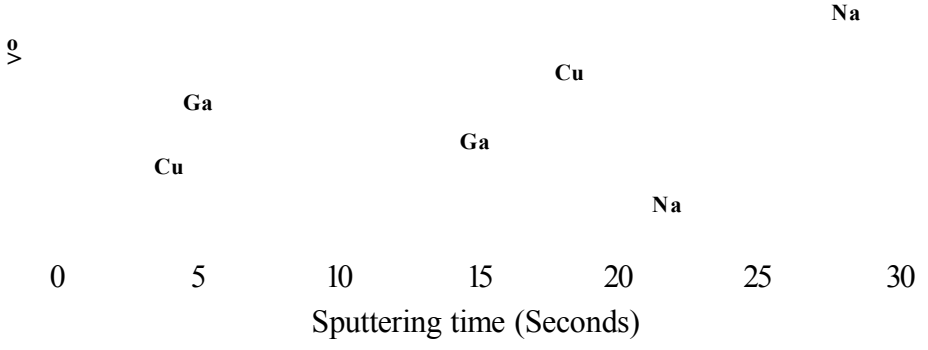

Figure 6.15: GDOES profile of a $CuInSe_2$ film grown on a glass/FTO substrate by electrodeposition at -0.8 V vs Ag/AgCl reference electrode in an aqueous solution containing $CuSO_4$, $In_2(SO_4)_3$, $Ga_2(SO_4)_3$ and H_2SeO_3 in the ratio 1:4:4:4. The sample has been annealed in nitrogen at 350°C for 30 minutes.

It can be seen that the electrodeposited film has a non-uniform distribution for all the elements throughout the thickness of the layer, as also observed for CIGSS layers grown by the two-stage method. However, the GDOES depth profile of the electrodeposited CIS film reveals that selenium is distributed more uniformly than copper and indium. More indium and copper is present at the FTO side and it is noteworthy that some is also observed within the transparent conducting oxide. This could be due to the diffusion or/and to a preferential sputtering of the elements involved in the analysis. Overlapping

of the Sn signal with the Cu, In, Ga and Se signals can also arise due to the FTO surface roughness. Note that similar observations have been made on the GDOES depth profile of CIGSS films grown on glass/Mo substrates by the two-stage method (See Section 5.4). It is interesting to notice that gallium is detected in the electrodeposited layer, although the signal remains very low and noisy. It is finally worth mentioning that contrary to GIGSS grown by the two-stage method, no sodium has diffused from the glass substrate through the surface of the film. This is mainly due to the fact that the two-stage method involves higher temperatures than the technique of electrodeposition.

6.7 Optical analysis

The optical measurements of $CuInSe_2$ thin films were performed on a Nicolet model MAGNA-IR 860 FTIR spectrometer. Figure 6.16 (a) shows the optical absorption curves of an annealed $CuInSe_2$ film grown on a glass/ITO substrate by electrodeposition at -0.8 V voltage vs Ag/AgCl reference electrode in an aqueous solutions containing $CuSO_4$, $In_2(SO_4)_3$, $Ga_2(SO_4)_3$ and H_2SeO_3 in the ratio 1:4:4:4. One can see a sharp change in the absorbance, which occurs at wavelengths lower than 1400 nm. This is representative of the optical properties of semiconductors and suggests the existence of a band gap energy. To determine the band gap energy of the electrodeposited film, $(Absorbance.Energy)^2$ versus the energy of the incident photons was plotted and the curve is displayed in Figure 6.16 (b). No clear linear region is observed, contrary to what is expected for a direct energy gap semiconducting material. The interceptions of the slopes of the curve at its two extremities with the x-axis give band gap values of 1 eV and 1.25 eV. The accepted band gap of $CuInSe_2$ is reported to be 1.04 eV [13] and the above observation shows the existence of a band gap region covering 1.00-1.25 eV. The electrodeposited material may therefore consist of a mixture of phases, such as $CuInSe_2$ and $CuIn_3Se_5$, as the band gap of $CuIn_3Se_5$ present in In-rich $CuInSe_2$ is reported to be higher (1.3eV) [9]. Optical transitions above the band gap have also been observed by Tuttle et al. [14] and Guillén et al. [8] and were attributed to a spin-orbit valence band splitting. The value of the spin-orbit valence band splitting, Δ_{so} = 0.22-0.24 eV, given by Tuttle et al. [14] seems reasonable. It is noteworthy that the phenomenon of excessive sub-band-gap absorption related to the presence of the p-type degenerated secondary phase $Cu_{2-x}Se$ at grain boundaries and surfaces [14], is not observed, which suggests that this phase is not

present or not abundant within the electrodeposited films. It is worth mentioning that the reflections and scatterings of the light are not taken into account and could therefore affect the optical absorption measurements. It is, however, interesting to point out that if electrodeposited CIS materials contained several phases with different band gap energies, it could improve the absorption of photons and therefore enhance the short circuit current of electrodeposited $CuInSe_2$-based solar cells.

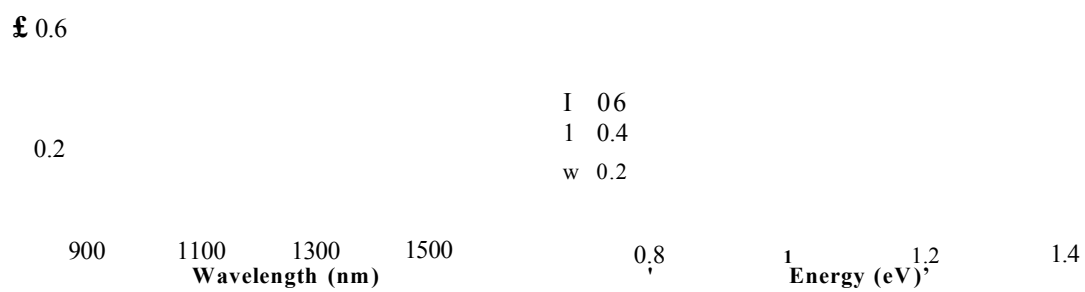

Figure 6.16: Optical absorption curves of an annealed $CuInSe_2$ film grown on a glass/ITO substrate by electrodeposition at -0.8 V voltage vs Ag/AgCl reference electrode in an aqueous solution containing $CuSO_4$, $In_2(SO_4)_3$, $Ga_2(SO_4)_3$ and H_2SeO_3 in the ratio 1:4:4:4: (a) plot of the absorbance versus the wavelength of the incident photons and (b) plot of $(Absorbance.Energy)^2$ versus the energy of the incident photons.

6.8 Electrical analysis

Photoelectrochemical measurements were performed to determine the conductivity type of electrodeposited $CuInSe_2$ layers. The electrolyte used for PEC measurements was a 0.1 M KCl aqueous solution. Table 6.5 shows the photovoltages observed for $CuInSe_2$ films electrodeposited on glass/FTO substrates at different deposition voltage vs Ag/AgCl reference electrode in aqueous solutions with $CUSO_4$, $In_2(SO_4)_3$, $Ga_2(SO_4)_3$ and H_2SeO_3 in the ratio 1:4:4:4. Note that the signals are very low when compared to those measured for the window materials (see Chapter 4), as also observed for the $Cu(InGa)(SeS)_2$ grown by the two-stage method. As already discussed in Section 5.5, this could be due to the photons being absorbed near the film surface in a dead layer (an absorbing layer with a high recombination rate) so that they are not completely transformed into photocurrent. This assumption is supported by the work of Vedel et al.

on the photoelectrochemical properties of electrodeposited $CuInSe_2$ [1]. The low signals could also account for the existence of an opposing potential barrier within the layer to the junction formed at the semiconductor/electrolyte interface.

E_{dep} (V)	Post deposition treatment	V_{dark} (mV)	V_{light} (mV)	V_{photo} (mV)	Conductio n type
-0.5	As deposited	-201.8	-198.6	+3.2	p-type
	Annealed in air at 200°C for 15 minutes	-189	-174	+15	p-type
	Annealed in N_2 at 350°C for 30 minutes	-167.5	-167.5	0	unknown
-0.6	As deposited	-192	-191.7	+0.3	p-type
	Annealed in air at 200°C for 15 minutes	-171	-166.5	+4.5	p-type
	Annealed in N_2 at 350°C for 30 minutes	-190.6	-190.6	0	unknown
-0.7	As deposited	-228.6	-227.4	+1.2	p-type
	Annealed in air at 200°C for 15 minutes	-283	-274	+9	p-type
	Annealed in N_2 at 350°C for 30 minutes	-285	-281.7	+3.3	p-type
-0.8	As deposited	-210	-210	0	unknown
	Annealed in air at 200°C for 15 minutes	-283.7	-278.5	+5.2	p-type
	Annealed in N_2 at 350°C for 30 minutes	-337.7	-337.4	+0.3	p-type
-0.9	As deposited	-239	-238	+1	p-type
	Annealed in air at 200°C for 15 minutes	-385	-365	+20	p-type
	Annealed in N_2 at 350°C for 30 minutes	-313	-321	-8	n-type
	Annealed in N_2 at 350°C for 30 minutes	-276	-274	+2	p-type

Table 6.5: Photovoltage produced at different liquid/CIS junctions during white light illumination. $CuInSe_2$ layers were electrodeposited on glass/FTO at different deposition voltages vs Ag/AgCl reference electrode in aqueous solutions containing $CuSO_4$, $In_2(SO_4)_3$, $Ga_2(SO_4)_3$ and H_2SeO_3 in the ratio 1:4:4:4.

One can observe from these results that the photovoltage is generally positive, whatever the deposition voltage and the heat treatment, demonstrating the p-type character of the electrodeposited materials. However, it can be seen that some films grown at low deposition voltages (-0.9 V) show n-type conductivity after annealing in nitrogen atmosphere at 350°C for 30 minutes. This result could mean that $CuInSe_2$ starts to be converted from p-type to n-type when deposited at large negative voltages, as expected. One can also observe that annealing the samples in air at 200°C for 15 minutes enhances the p-type conductivity, as it is often reported [15]. Sometime no photovoltage was observed, which is likely to be related to bad deposition of the film or to the deterioration of the films through the annealing process. It is worth mentioning that the PEC results have to be taken with extreme care, as the measured voltages were not very stable, probably because of the slow decomposition of the films in the electrolyte.

6.9 Summary and conclusions

In this chapter, it was shown that $CuInSe_2$ films could successfully be grown on glass/ITO or glass/FTO using the technique of electrodeposition. An annealing step is needed to improve the structural as well as the electrical properties of the films.

The CIS films are polycrystalline and XRD analysis brings to light the peaks relative to the diffraction by the atomic planes (112), (220) or (204), (312) or (116), (400) or (008) and (316) or (332) of the chalcopyrite structure. The films are strongly oriented along the <112> axis perpendicular to the substrate, as also observed for CIGSS grown by the two-stage method. The composition of the electrodeposition bath and the deposition voltage are found to influence strongly the structure of the films. The formation of additional phases, such as Cu-Se and $CuIn_3Se_5$, is also reported. Note that the addition of $Ga_2(SO_4)_3$ into the bath does not lead to significant deposition of gallium into the films.

The surface of near-stoichiometric CIS films appear dense with a good mechanical adhesion to the conducting oxide substrates and show crack-free surfaces with spherical grains electrically well connected to each other with a size up to 1 μm. All the electrodeposited $CuInSe_2$ films have a rms roughness measured by scanning over a 10 x 10 μm^2 scan area of less than 50 nm, which is lower than the one calculated for CIGSS grown by the two-stage method (126.6 nm). Hermann et al. have also observed such a difference between electrodeposited films and sputtered films [16]. Smoother films can show reduced light trapping at the surface but they are, nevertheless, advantegeous in that the number of interface states between the absorber layer and the metal contact in the device is lowered.

The distribution of Cu, In and Se is not uniform within the CIS films and a high content of indium is found on the surface, which is attributed to the segregation of In-rich phases, such as $CuIn_3Se_5$. Another possible reason for this high concentration of In on the surface of the films is the preferential formation of In_2O_3, as its heat of formation is lower than those of selenium oxides and copper oxides.

Testing of electrical conductivity shows that the films are generally p-type, although the signals are very low, which could be related to the presence of a dead layer near the surface of the films or to the existence of an opposing potential barrier within the layer to the junction formed at the semiconductor/electrolyte interface.

6.10 References

[1] Vedel J., Thouin L., Lincot D., Journal of Electrochemical Society, 143 (7) (1996) 2173.

[2] Kampmann A., Cowache P., Lincot D., Vedel J., Journal of Electrochemical Society, 146 (1) (1999) 150.

[3] Klenk R., Walter T., Schock H. W., Cahen D., Advanced Materials, 5 (2) (1993), 114.

[4] Rincon C., Ramirez F. J., Journal of Applied Physics, 72 (9) (1992) 4321.

[5] Rincon C., Wasim S. M., Marin G., Delgado J. M., Huntzinger J. R., Zwick A., Galibert J., Applied Physics Letters, 73 (4) (1998) 441.

[6] Lippold G., Eifler A., Yakushev M. V., Tomlinson R. D., Klenk R., Schock H. W., Grill W., Proceedings of 11th International Conference on Ternary and Multinary Compounds, Institute of Physics Conference Series, 152 (1998) 697.

[7] Bhattacharya R. N., Fernandez A. M., Contreras M. A., Keane J., Tennant A. L., Ramanathan K., Tuttle J. R., Noufi R. N., Hermann A. M., Journal of Electrochemical Society, 143 (3) (1996) 854.

[8] Guillén C., Herrero J., Solar Energy Materials and Solar Cells, 43 (1996) 47

[9] Schmid D., Ruckh M., Grunwald F., Schock H. W., Journal of Applied Physics, 73 (6) (1993) 2902.

[10] Lide D. R., Handbook of Chemistry and Physics, 79th edition, CRC (1998-1999).

[11] Kaye G. W. C., Laby T. H., Tables of Physical and Chemical Constants, 16th Edition, Longman (1995).

[12] Kwon S. H., Ahn B. T., Kim S. K., Yoon K. H., Song J., Thin Solid Films, 323 (1998) 265

[13] Moller H.J., Progress in Materials Science, 35 (1991) 205.

[14] Tuttle J. R., Albin D., Matson R. J., Noufi R., Journal of Applied Physics, 66 (9) (1989) 4408.

[15] Kushiya K., Hakuma H., Sano H., Yamada A., Konagai M., Solar Energy Materials and Solar Cells, 35 (1994) 223.

[16] Hermann A. M., Mansour M., Badri V., Pinkhasov B., Gonzales C., Fickett F., Calixto M. E., Sebastian P. J., Marshall C. H., Gillespie T. J., Thin Solid Films, 361-362 (2000) 74.

Chapter 7: Development of electrodeposited $CuInSe_2$-based solar cells

7.1 Introduction

This chapter deals with the development of electrodeposited $CuInSe_2$-based solar cells. The conditions of electrodeposition used to grow the layers suitable for making high efficiency photovoltaic devices will first be given. Then, one will study the etching procedure of CIS layers, as this information is very important for the development of electronic devices. The variations of the surface stoichiometry of chemically etched CIS films using various etchants were examined by XPS. To obtain information on the electrical and photovoltaic properties of completed $CuInSe_2$-based solar cells, current-voltage (I-V) measurements were performed. The preliminary results on metal-semiconductor junctions as well as heterojunctions based on electrodeposited $CuInSe_2$ will be reported and discussed in Section 7.4. C-V measurements on a glass/ITO/$CuInSe_2$/Au structure were also carried out and the results will be discussed in Section 7.5. Finally, a summary of the main results will be given.

7.2 Experimental details

The experimental details concerning the electrodeposition of $CuInSe_2$ have been described in Chapter 6. The conditions selected for the production of $CuInSe_2$-based solar cells are as follows: the deposition voltage was either -0.7 V or -0.8 V vs Ag/AgCl reference electrode, the electrolyte was an aqueous solution containing $CuSO_4$, $In_2(SO_4)_3$, $Ga_2(SO_4)_3$ and H_2SeO_3 in the ratio 1:4:4:4, the deposition time was 40 minutes and the temperature during the growth was maintained at 60°C, the as-deposited films were finally annealed in nitrogen atmosphere at 350°C for 30 minutes.

A typical current versus time graph showing the homogeneity of the growth is presented in Figure 7.1. One can observe that the current density is quite steady between 0.8 mA/cm and 0.9 mA/cm . The regular decrease of the current density during the growth is mainly related to the increase in resistivity of the substrate due to the deposition of the film. It results also from the decrease of the concentrations of the reactive species in the electrolyte. When considering a current density of 0.85 mA/cm , the theoretical thickness of the films can be estimated to 0.95 pm by using Equation (2.14). For this calculation, the values of the molecular weight (336.29 g/mol1) and the density (5.77 g/cm^{3}) of intrinsic $CuInSe_2$ were used [1]. The number of electrons transferred was taken as 13, according to the total electrode reaction (see Section 2.4.1).

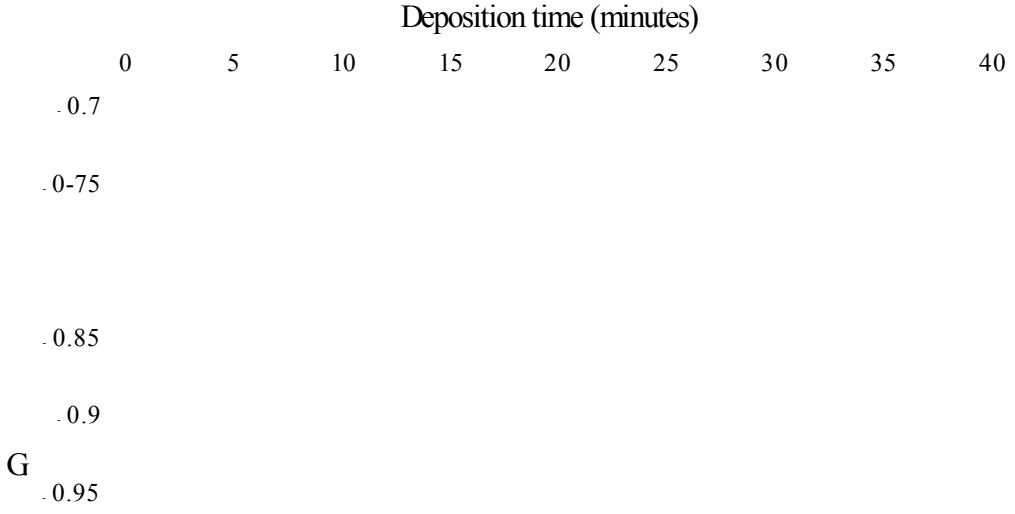

Figure 7.1: Typical current versus time curve of CuInSe2 electrodeposited at -0.8 V vs Ag/AgCl reference electrode in aqueous solutions containing CuS04, In2(S04)3, Ga2(S04)3 and H2Se03 in the ratio 1:4:4:4.

One has to refer to Chapter 4 for the experimental details concerning the electrodeposition of CdS and ZnSe. Note, however, that prior to the growth of CIS on CdS or ZnSe, the window material layers were heat treated and chemically etched in a solution containing 0.5 g of NaOH and 0.5 g of $Na_2S_2O_3$ diluted in 100 ml of water.

7.3 Effect of chemical etching on $CuInSe_2$ films

Wet chemical etching is used in device processing in order to clean the surfaces from contaminants (like oxides), to modify the surface composition of the films and to passivate their surface states. In this section, the effects of various chemical etchants on the composition of $CuInSe_2$ surfaces were investigated. A $CuInSe_2$ film was electrodeposited on a 6 x 2 cm^2 glass/FTO substrate at -0.8 V vs Ag/AgCl reference electrode in an aqueous solutions containing $CuSO_4$, $In_2(SO_4)_3$, $Ga_2(SO_4)_3$ and H_2SeO_3 in the ratio 1:4:4:4. The sample was then annealed in nitrogen atmosphere at 350°C for 30 minutes. Six different specimens (approximately 1 x 1 cm^2) were cut from this sample and chemically etched in various commonly used etchants. The details on the chemical etchant solutions are given in Table 7.1.

The chemically etched specimens were immediately transferred to the Microlab after etching to minimise further oxidation and the changes in the composition and chemical environment of the surface were examined using XPS. One specimen was left untreated for comparison. One has to refer to Section 6.6.2 for the details concerning the XPS results on this specimen.

Etchant	Etchant composition	Etching time
H_2SO_4 & $K_2Cr_2O_7$	1 g of $K_2Cr_2O_7$ in 10 ml of H_2SO_4 (95-98%) + 490 ml of water	20 seconds
HCl & HNO_3	10 ml of HCl (37%) + 10 ml of HNO_3 (70%) + 80 ml of water.	1 minute
NH_4OH	NH_4OH (35%)	50 minutes
NaOH & H_2O_2	1 g of NaOH in 1 ml of H_2O_2 (30%) + 40 ml of water	1 minute
H_2SO_4 & $K_2Cr_2O_7$ followed by NaOH & $Na_2S_2O_3$	H_2SO_4 & $K_2Cr_2O_7$ etchant followed by NaOH & $Na_2S_2O_3$ etch (0.5 g of NaOH + 0.5 g of $Na_2S_2O_3$ in 100 ml of water)	20 seconds + 2 minutes

Table. 7.1: Details of the chemical etchants used for $CuInSe_2$ surfaces.

XPS measurements on each sample were performed on a VG ESCALAB II using Mg K_α (1253.6 eV) radiation. As the material layer was grown on glass/FTO substrates, a conducting path was provided by connecting the CIGS layer to the metal holder using Ag conducting paste. One has to refer to Section 5.4.2 reporting the XPS results of CIGSS grown by two-stage method for more experimental details.

7.3.1 Etching of $CuInSe_2$ in H_2SO_4 & $K_2Cr_2O_7$

Figure 7.2 shows the XPS survey spectrum of $CuInSe_2$ grown on glass/FTO after etching treatment in H_2SO_4 & $K_2Cr_2O_7$. Contrary to the observations made by Yakushev et al. who used the Rutherford backscattering technique to study the effect of H_2SO_4 & $K_2Cr_2O_7$ etching treatment on $CuInSe_2$ crystals [2], the stoichiometry of electrodeposited CIS surface studied by XPS changes drastically. Thus, one can notice that copper and indium peaks have drastically decreased when compared to those observed for as-deposited samples (Figure 6.13). On the other hand, peaks arising from Se 3d and Se 3p have increased. This result is not surprising, as H_2SO_4 & $K_2Cr_2O_7$ is a very strong oxidising etchant. Cu(I) and Se(-II) could therefore be oxidised and, as a result of the chemical bonds being broken, Cu^{2+} and In^{3+} could be removed from the solid surface into the acidic solution. It is noteworthy that H_2SO_4 & $K_2Cr_2O_7$ does not seem to be appropriate for removing oxides covering the surface of the films, as O 1s peak has increased after etching.

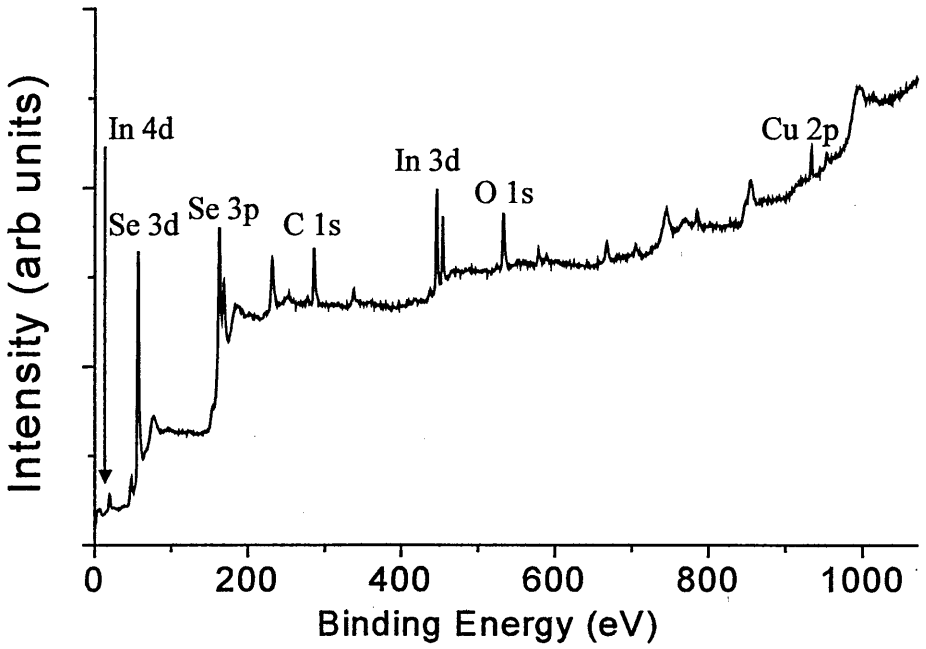

Figure 7.2: XPS survey spectrum of $CuInSe_2$ grown on glass/FTO after etching treatment in H_2SO_4 & $K_2Cr_2O_7$.

As can be seen in Figure 7.3 showing the high-resolution XPS spectra of Cu 2p, In 3d, and Se 3d core levels, there is no noticeable shift of the In 3d and Se 3d peaks, which

suggests that the chemical nature of these elements remains the same. Note a small shift of Cu 2p peak towards the CuO line, which could suggest the formation of CuO, but the absence of the shake up peak characteristic of this oxide at about 940 eV does not support this argument.

The strong removal of the metallic elements from the CIS surface during the H_2SO_4 & $K_2Cr_2O_7$ etching process suggests that this etchant has to be used in combination with another etchant so that the surface composition can be made closer to stoichiometry. Note that the use of a more dilute solution would be preferential to reduce the Cu and In removal from the CIS surfaces.

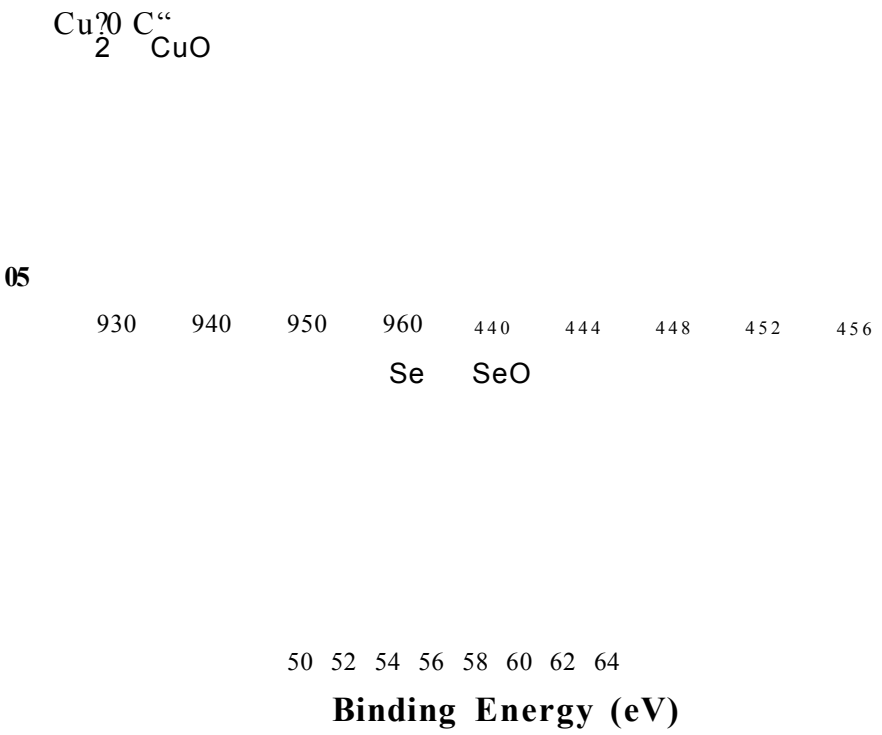

Figure 7.3: **High-resolution XPS spectra of Cu 2p, In 3d, and Se 3d core levels of CuInSe2 grown on glass/FTO after etching treatment in H2S 0 4 & K2Cr20 7.**

7.3.2 Etching of $CuInSe_2$ in HCl & HNO_3

Figure 7.4 shows the XPS survey spectrum of $CuInSe_2$ grown on glass/FTO after etching treatment in HCl & HNO_3. The main observation on this spectrum is the decrease of Cu 2p, In 3d and In 4d peaks probably due to the oxidation of Cu(I) and Se(-II), which is responsible for the removal of Cu and In ions from the film surface into the aqueous solution. The Cu:In ratio was calculated and it is found to increase from 0.29 before wet

chemical treatment to 0.39 after etching in HCl & HNO_3, which means that indium has been removed preferentially. This suggests that the removal of In_2O_3 and $CuIn_3Se_5$ phases may have been favoured. It is noteworthy that the O 1s peak has significantly decreased, which indicates that HCl & HNO_3 is a powerful etchant for removing native oxides from the surface of CIS films.

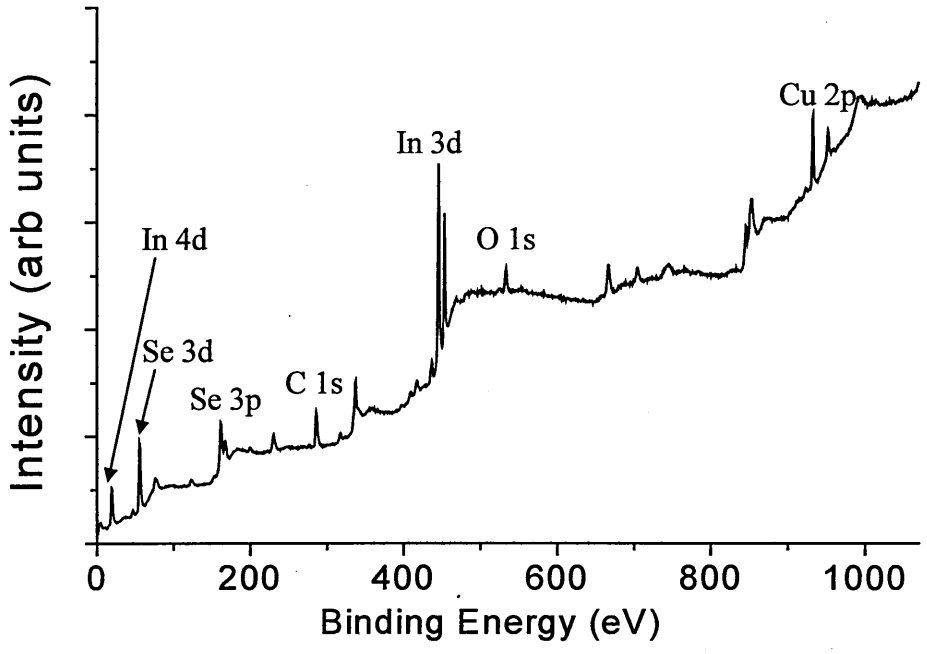

Figure 7.4: XPS survey spectrum of $CuInSe_2$ grown on glass/FTO after etching treatment in HCl & HNO_3.

High-resolution XPS spectra of Cu 2p, In 3d, and Se 3d core levels are displayed in Figure 7.5. One can see that the peak of selenium has broadened, which means that Se atoms have different chemical environments. Selenium could possibly stand on the surface of the film as elemental Se and Se embedded in a Cu-In-Se matrix. The formation of elemental selenium could be related to Se(-II) from $CuIn_3Se_5$ phase being oxidised into Se(0), which precipitates at the surface. Note that the shift of the Cu 2p peak towards the CuO line reported for the specimen etched in H_2SO_4 & $K_2Cr_2O_7$ solution is no longer observed.

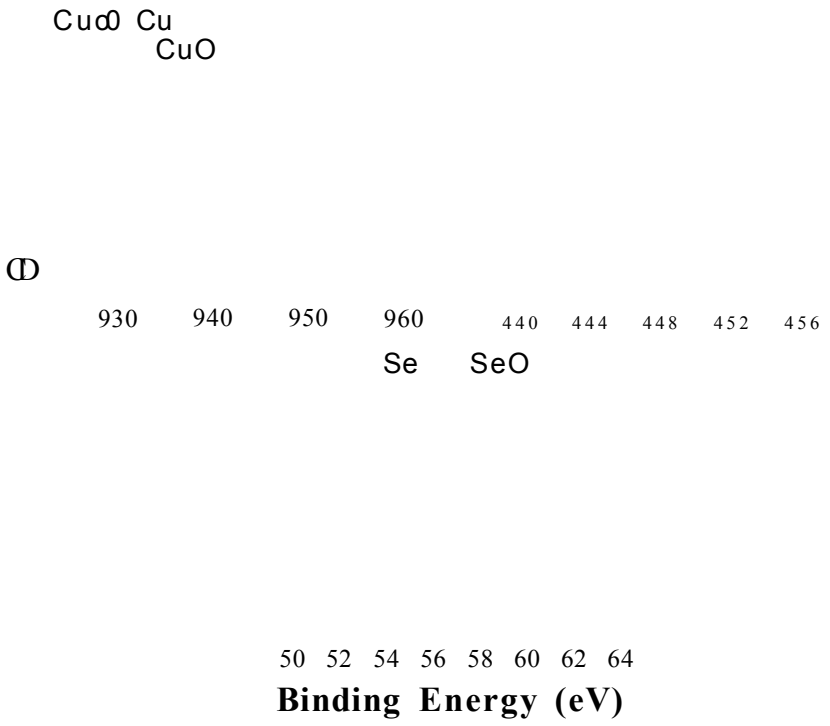

Figure 7.5: High-resolution XPS spectra of Cu 2p, In 3d and Se 3d core levels of $CuInSe_2$ grown on glass/FTO after etching treatment in HCI & HN03.

7.3.3 Etching of $CuInSe_2$ in NH_4OH

Figure 7.6 shows the XPS survey spectrum of $CuInSe_2$ grown on glass/FTO after etching treatment in NH_4OH. First, one can notice an increase of Se 3d and Se 4d peaks and a decrease of In 3d, In 4d and Cu 2p peaks. A preferential removal of indium compared to copper is also found, as the Cu:In ratio has increased from 0.29 to 0.58 after NH_4OH treatment. These observations suggest that the CuI^Ses top layer is oxidised leaving elemental selenium on the surface. Note that this etchant seems to be very suitable for removal of oxides, as a strong reduction of oxygen is observed.

High-resolution XPS spectra of Cu 2p, In 3d, and Se 3d core levels are displayed in Figure 7.7. No noticeable shift is observed for Cu 2p and In 3d peaks, which suggests that the chemical nature of these elements remains the same. Note that the broadening of Se 3d peak is observed once more, which means that Se atoms have different chemical environments and confirms the existence of elemental selenium on the surface of the films.

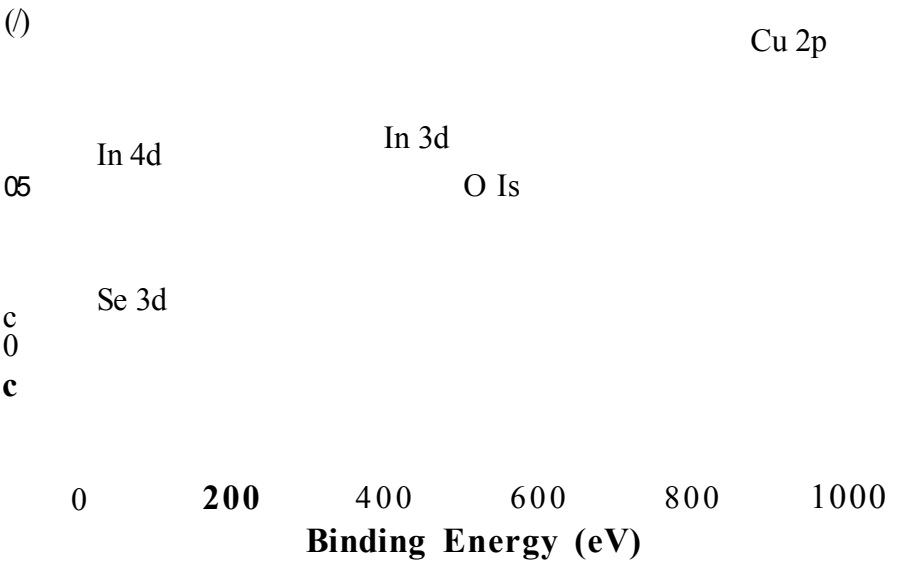

Figure 7.6: XPS survey spectrum of $CuInSe_2$ grown on glass/FTO after etching treatment in NH_4OH.

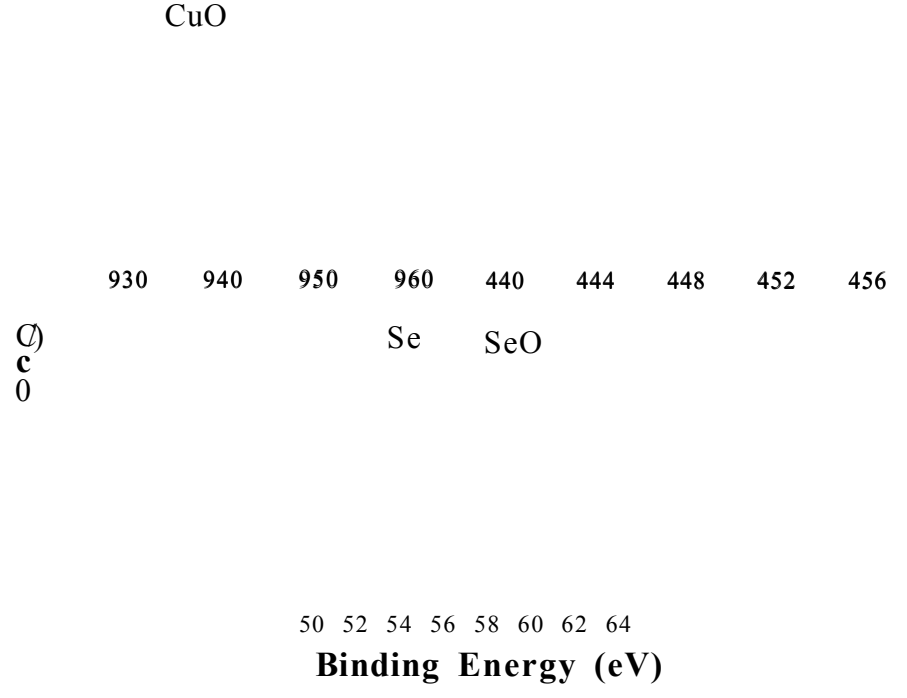

Figure 7.7: High-resolution XPS spectra of Cu 2p, In 3d and Se 3d core levels of $CuInSe_2$ grown on glass/FTO after etching treatment in NH_4OH.

The use of NH_4OH etchant seems to be suitable for etching of In-rich films, as it removes preferentially indium and is also very effective for cleaning the surface removing most of the native oxides. However, elemental selenium appears to remain on the surface of the films. Another appropriate etchant could be used after etching in NH_4OH to remove this selenium layer.

7.3.4 Etching of $CuInSe_2$ in NaOH & H_2O_2

Figure 7.8 shows the XPS survey spectrum of $CuInSe_2$ grown on glass/FTO after etching treatment in NaOH & H_2O_2. A strong reduction of the selenium concentration is brought to light with Se 3d and Se 4d peaks having nearly disappeared. On the other hand, O 1s peak has significantly increased. One explanation could be that selenium is oxidised by H_2O_2 into SeO_2, which further reacts with hydroxide ions to form selenium hydroxide dissolving in the solution.

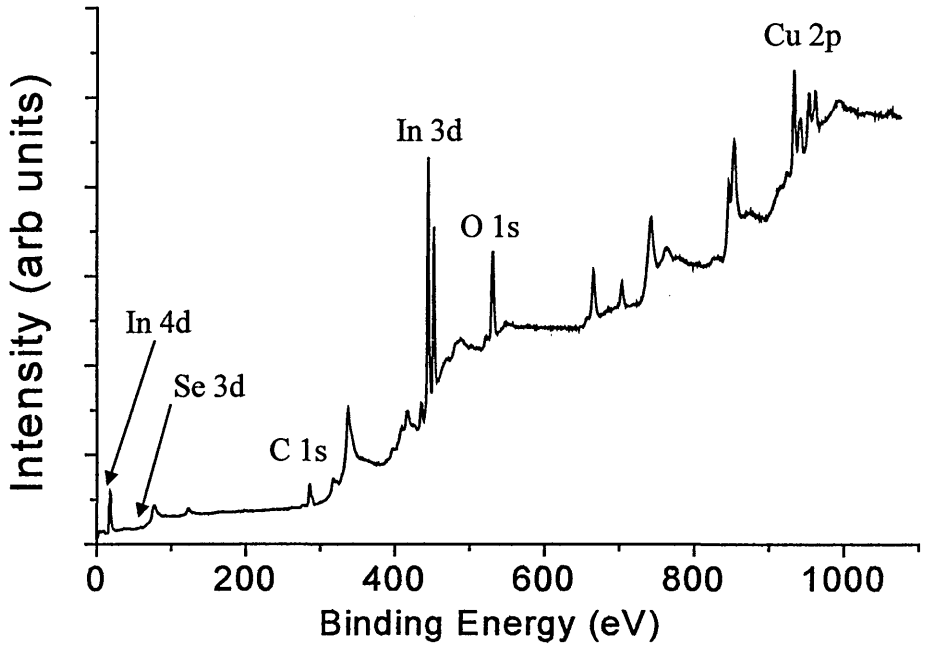

Figure 7.8: XPS survey spectrum of $CuInSe_2$ grown on glass/FTO after etching treatment in NaOH & H_2O_2.

High-resolution XPS spectra of Cu 2p, In 3d, and Se 3d core levels are displayed in Figure 7.9. Several changes in the chemical nature of these elements have occurred after etching treatment in NaOH & H_2O_2. Cu 2p peak has broadened, which suggests that Cu

atoms have different chemical environments including CuO and elemental copper. The presence of CuO is confirmed by the characteristic shake up peak at about 940 eV. Note also the shift of In 3d peak towards the In 3d line, which suggests that indium stands mainly as elemental indium on the surface of the CIS film. Traces of selenium in the form of elemental selenium and SeO_2 can still be observed. SeO_2 may come from the oxidation of Se(-II) in the CIS matrix, which has not completely reacted with OH' to form selenium hydroxide. The low signal relative to Se is more likely to come from Se embedded in a CIS matrix quite deep in the film.

As NaOH & H_2O_2 solution reacts strongly with Se, it does not seem to be suitable for CIS etching treatment. However, it could be used for removing elemental selenium layers formed during the etching procedure involving HCl & HNO_3 or NH_4OH.

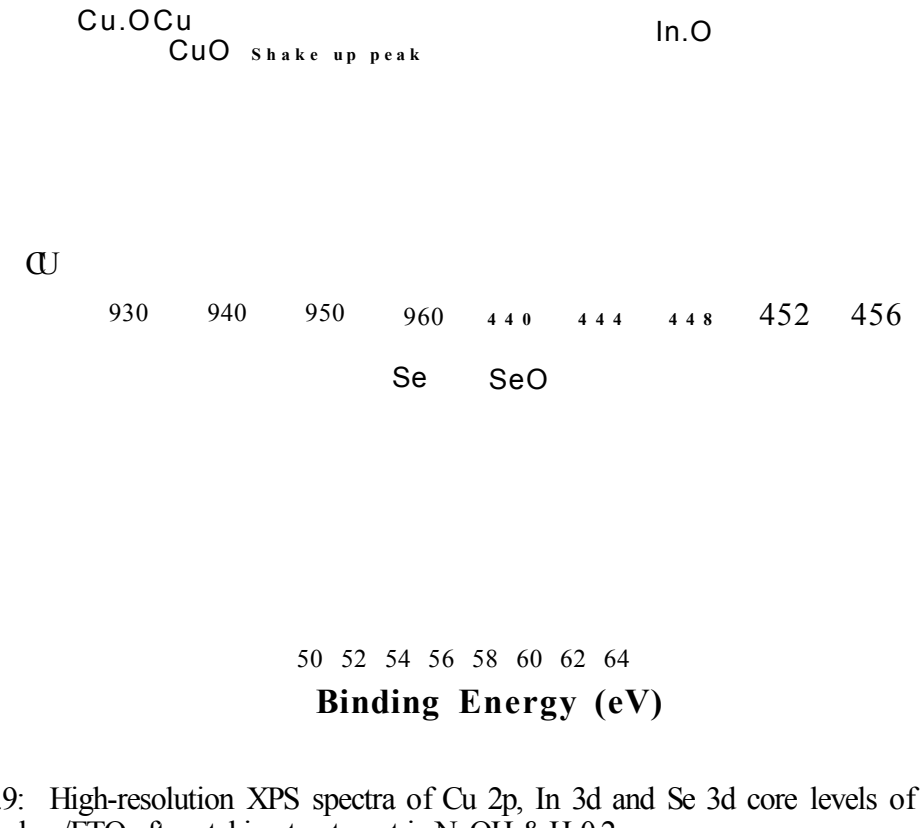

Figure 7.9: High-resolution XPS spectra of Cu 2p, In 3d and Se 3d core levels of $CuInSe_2$ grown on glass/FTO after etching treatment in NaOH & H_2O_2.

7.3.5 Etching of CuInSe2 in H2SO4 & K2Cr2O7 followed by NaOH & Na2S2O3

Figure 7.10 shows the XPS survey spectrum of $CuInSe_2$ grown on glass/FTO after etching treatment in H_2SO_4 & $K_2Cr_2O_7$ followed by NaOH & $Na_2S_2O_3$. When compared to the XPS survey spectrum of $CuInSe_2$ surface etched in H_2SO_4 & $K_2Cr_2O_7$, one can see

that the selenium peak has decreased significantly due probably to the oxidation of Se by $Na_2S_2O_3$ into SeO_2, which further reacts with hydroxide ions to form selenium hydroxide dissolving in the solution.

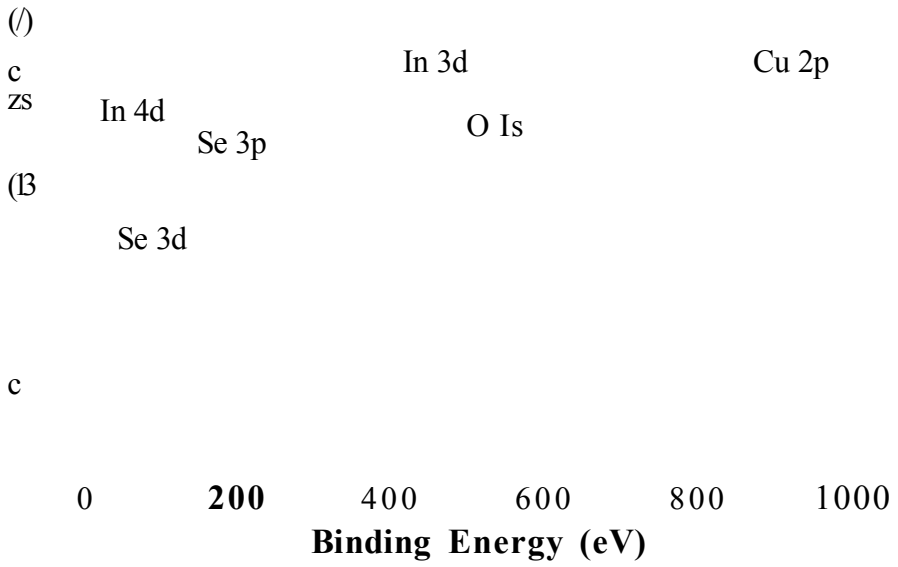

Figure 7.10: XPS survey spectrum of CuInSe2 grown on glass/FTO after etching treatment in H2S04 & K2Cr207 followed by NaOH & Na2S203.

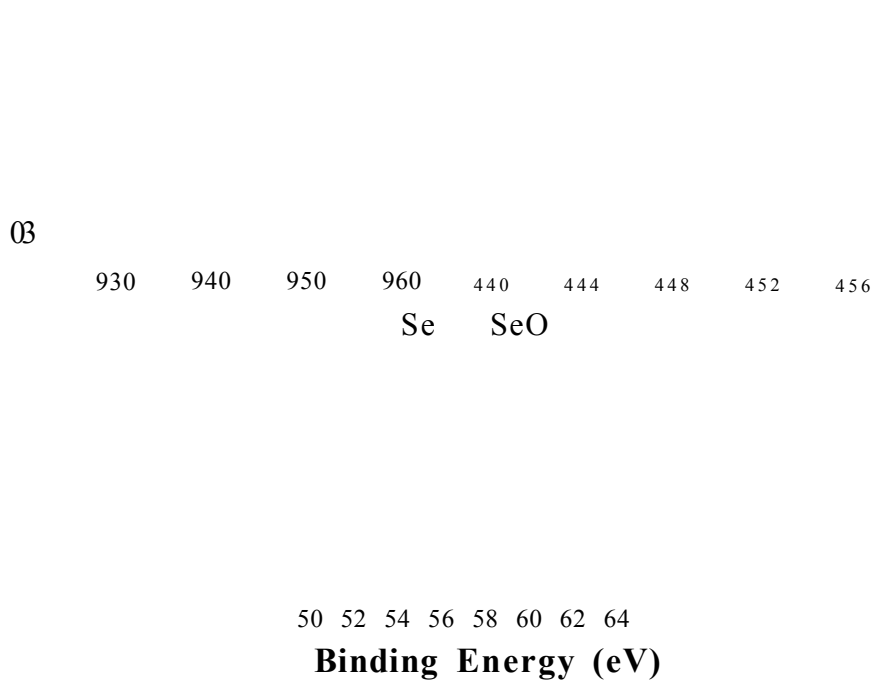

Figure 7.11: High-resolution XPS spectra of Cu 2p, In 3d and Se 3d core levels of CuInSe2 grown on glass/FTO after etching treatment in H2S04 & K2Cr207 followed by NaOH & Na2S203.

High-resolution XPS spectra of Cu 2p, In 3d, and Se 3d core levels are displayed in Figure 7.11. These spectra are very similar to those of CIS films after etching in H_2SO_4 & $K_2Cr_2O_7$. The main difference is that the shift of the Cu 2p peak towards the CuO line reported after etching in H_2SO_4 & $K_2Cr_2O_7$ is no longer seen.

7.3.6 Concluding remarks

The surface composition of CIS films grown by electrodeposition is very sensitive to wet chemical treatment. Se-rich and Se-depleted surfaces can be produced depending on the nature of the selected etchant. Etching treatment in H_2SO_4 & $K_2Cr_2O_7$, HCl & HNO_3 or NH_4OH gives rise to metal-depleted surface whereas Se-depleted surface can be obtained from NaOH & H_2O_2 and NaOH & $Na_2S_2O_3$ etching treatment. Table 7.2 shows the influence of the different etchants used in this study on the atomic composition ratio of copper, indium, selenium and oxygen present on the surface of $CuInSe_2$ films. Note that the most efficient etchants for removing native oxides are HCl & HNO_3 and NH_4OH. These two etchants are therefore likely to give the best results concerning the device performance, although they generally leave elemental selenium on the surface of the films. NaOH & H_2O_2 or NaOH & $Na_2S_2O_3$ could be used, as a complementary etchant to HCl & HNO_3 and NH_4OH to remove the Se layer.

Etchant	Atomic composition ratio			
	[Cu] (%)	[In] (%)	[Se] (%)	[O] (%)
As-grown	9.5	32.2	31.0	18.4
H_2SO_4 & $K_2Cr_2O_7$	1.7	6.3	69.7	20.3
HCl & HNO_3	9.8	25.1	47.5	13.0
NH_4OH	7.6	13.0	66.0	10.5
NaOH & H_2O_2	19.2	22.8	0.3	41.3
H_2SO_4 & $K_2Cr_2O_7$ followed by NaOH & $Na_2S_2O_3$	2.4	11.8	64.2	18.4

Table 7.2: Atomic composition ratio calculated from XPS measurements of Cu, In, Se and O on the surface of $CuInSe_2$ films after treatment in various etchants.

7.4 Current-voltage (I-V) analysis

Current-voltage measurements were performed to evaluate the efficiency of solar cells based on $CuInSe_2$ grown by electrodeposition using the conditions derived from Chapter 6 and described in Section 7.2. Prior to evaporation of the metal on CIS films, the

surface of the samples was washed in millipore water and then etched for 20 seconds in a highly diluted $K_2Cr_2O_7$ & H_2SO_4 solution containing 1 g of $K_2Cr_2O_7$ and 10 ml of H_2SO_4 (95-98%) followed by a NaOH & $Na_2S_2O_3$ etch containing 0.5 g of NaOH and 0.5 g of $Na_2S_2O_3$ diluted in 100 ml of water for 2 minutes. The metal contact formation has already been explained in Section 2.5.3.

7.4.1 I-V characteristics of glass/TCO/$CuInSe_2$/metal devices

Both gold and indium metals were used for electrical characterisation of metal/CIS interface. As CIS materials grown by electrodeposition at -0.7 V or -0.8 V are reported to be p-type (see Section 6.8), high work function metals, such as Au, should give rise to ohmic contacts whereas one should observe a rectifying behaviour for low work function metals, such as In. However, I-V characterisation revealed that both metals produced generally ohmic contacts when depositing on CIS layers. This surprising result concerning the In contact could be explained by the diffusion of indium from the metal contact throughout the $CuInSe_2$ material, which is converted into n-type and, as a result, produces non-rectifying junctions. This observation could also arise due to the presence of a heavily doped semiconducting material.

In Figure 7.12, the J-V characteristics of an atypical glass/ITO/$CuInSe_2$/Au device under dark conditions are displayed. It is evident from the difference in the slope of the J-V curve in reverse and forward biases that the CIS/metal junction is rectifying. Rarely observed, this rectification could be related to the Fermi level pinning resulting from the presence of surface or interface states, which causes band bending within a depletion region in the absorber film. This behaviour could also be explained by the short distance diffusion of indium from the ITO layer through the CIS film, most probably during the annealing process. N-type conversion of a thin layer close to the substrate could lead to the formation of an n-p junction within the CIS film and could be responsible for the rectification. Note that the rectification has not been observed for CIS films grown on glass/FTO substrates, which supports the In-diffusion argument.

The voltage breakdown of the diode is very low (about -0.5 V). The series resistance and shunt resistance were estimated from the slope of the J-V curve in the high forward direction and reverse direction, respectively. One can see that the series resistance (4.6 Ω/cm^2) is quite high and the shunt resistance is very low (54.5 Ω/cm^2), which suggests

that the leakage current is very important. It was not possible to estimate the ideality factor and the barrier height, as no straight line part could be clearly defined in the semi-log curve (see Figure 7.13). In addition, the estimation of the barrier height caused by either Fermi level pinning or formation of an n-p junction within the CIS film would not be correct due to an non-ideal behaviour of the I-V characteristics.

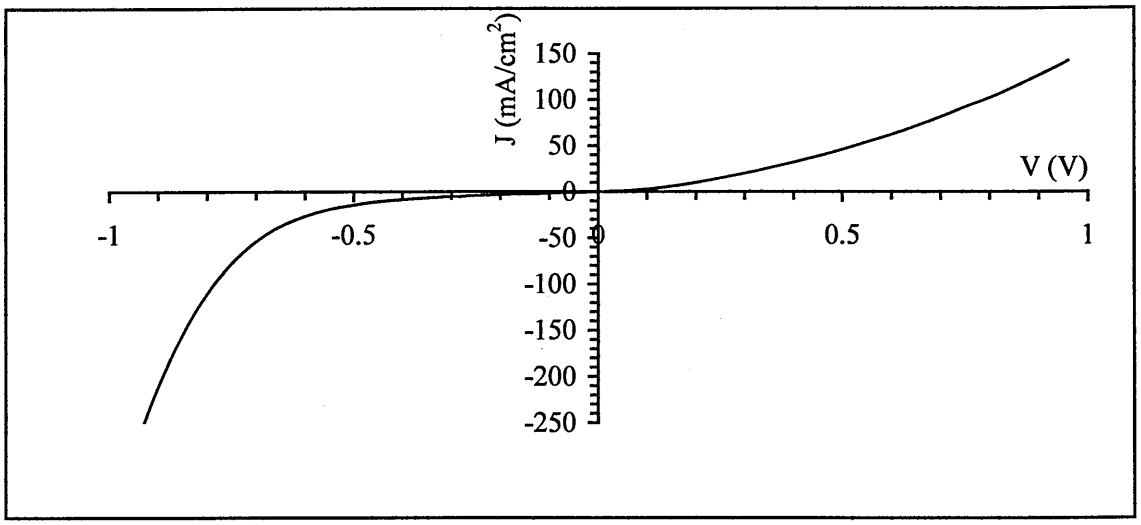

Figure 7.12: Linear J-V characteristics of glass/ITO/$CuInSe_2$/Au diode under dark conditions.

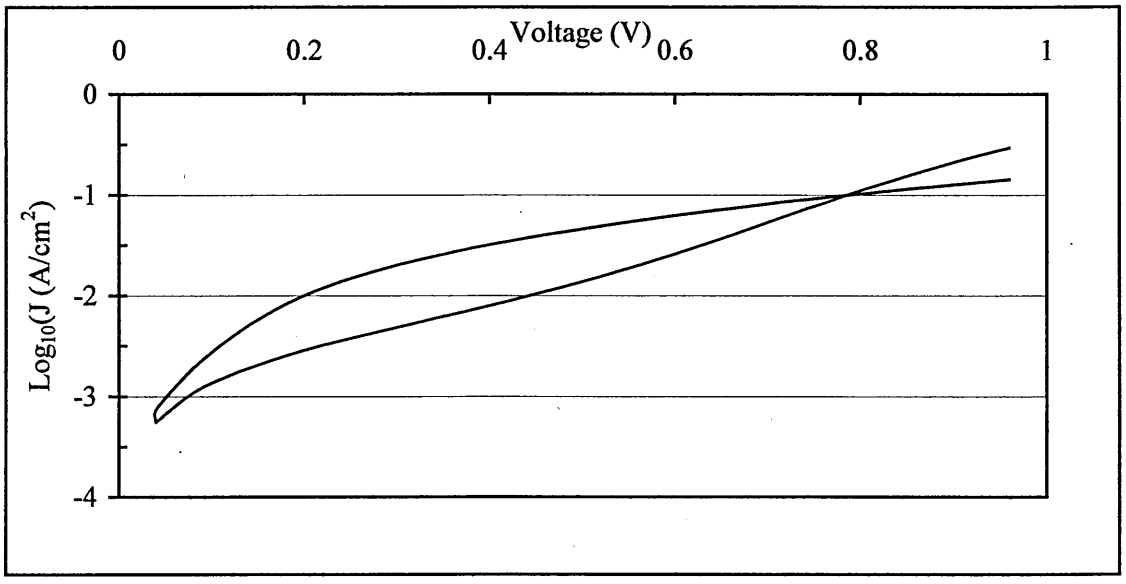

Figure 7.13: Semi-log J-V characteristics of glass/ITO/$CuInSe_2$/Au diode under dark conditions.

The current-voltage characterisation of the glass/ITO/$CuInSe_2$/Au diodes was carried out under illumination of 100 mW/cm^2 and the result concerning the best device to date is displayed in Figure 7.14. One can see that the diode is photovoltaic active. The three parameters generally used to assess the device performance were therefore evaluated. It is found that the open circuit voltage and the fill factor are relatively low with values of 0.15 V and 32 %, respectively. However, very high short circuit current of 60.7 mA/cm^2 is observed. It is not surprising to observe low open circuit voltage, as the barrier height of metal/semiconductor junctions are generally lower than the built-in potential of p-n junctions. If one supposes that the rectification is related to the n-p junction formed within the CIS film, the V_{OC} value could be explained by the low built-in potential of the junction due to the small band gap of $CuInSe_2$ (1.04 V). Note that heavily doped materials give rise to devices with low V_{OC}. The high series resistance and the very low shunt resistance of these device are also responsible for the low V_{OC} and FF.

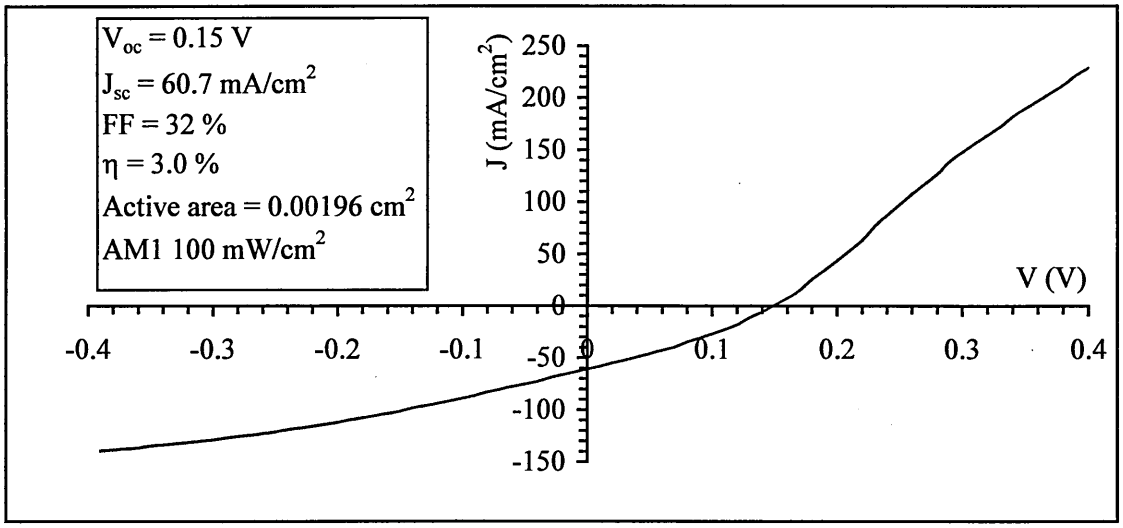

Figure 7.14: Linear J-V characteristics of glass/ITO/$CuInSe_2$/Au diode under illumination.

It is noteworthy that similar rectifying properties have also been observed with some indium contacts, although the polarity was inverted. The inversion of the polarity suggests that, in this case, a p-n junction is responsible for the rectification, as a result of the n-type conversion of a thin layer close to the CIS surface. The diffusion of indium from the metal contact could cause such a type conversion. Another obvious explanation is the formation of a normal Schottky junction between the p-type CIS film and the low work function metal.

As the doping by indium, diffusing from the metal contact or the substrate, depends on the defect chemistry in the CIS crystal, it is not surprising that these results are not reproducible.

Although the performances of these diodes remain low, with a maximum conversion efficiency of 3 %, these results were encouraging before the development of $CdS/CuInSe_2$ or $ZnSe/CuInSe_2$ solar cells. The insertion of a wide band gap window material layer between the substrate and the CIS layer should give rise to an increase of V_{OC} and the conversion efficiency should therefore be enhanced.

7.4.2 I-V characteristics of glass/ITO/ZnSe/$CuInSe_2$/Au devices

Current-voltage characterisation was carried out on glass/FTO/ZnSe/$CuInSe_2$/Au devices. The results for the best solar cell fabricated to date are reported here.

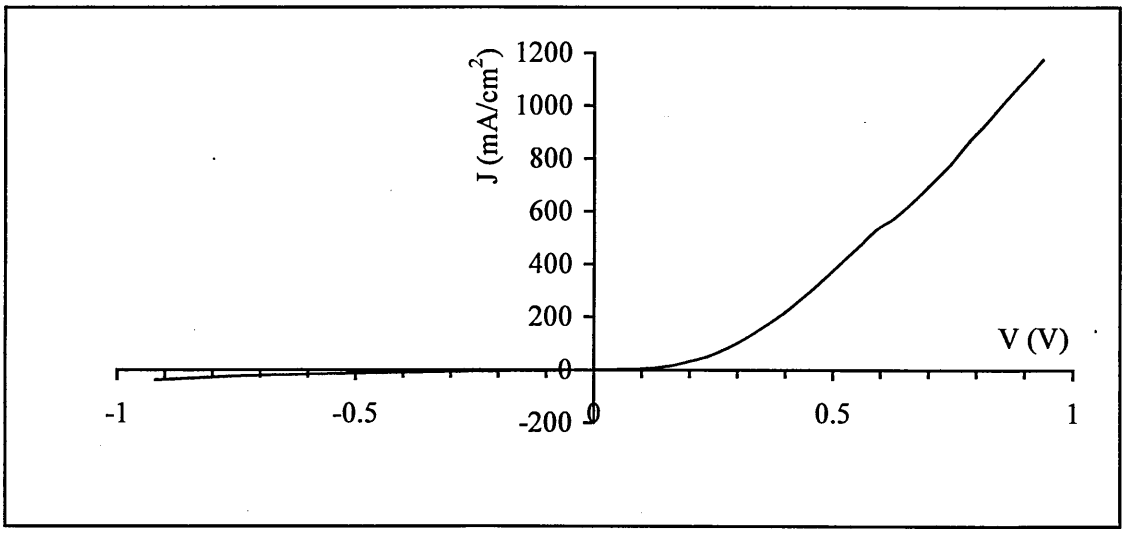

Figure 7.15: Linear J-V characteristics of glass/ITO/ZnSe/$CuInSe_2$/Au diode under dark conditions.

The series resistance and shunt resistance were extracted from the linear J-V characteristics measured under dark conditions (see Figure 7.15). It can be seen that the series resistance has reduced when compared to the metal/semiconductor junction and was evaluated to be 0.49 Ω/cm^2. This low series resistance is indicative of the good quality of the bulk material. The shunt resistance derived from the slope of the J-V curve in the reverse direction remains low (48.2 Ω/cm^2), which suggests that the leakage

current is still large. It is worth mentioning that no voltage breakdown is observed between 0 V and -1 V.

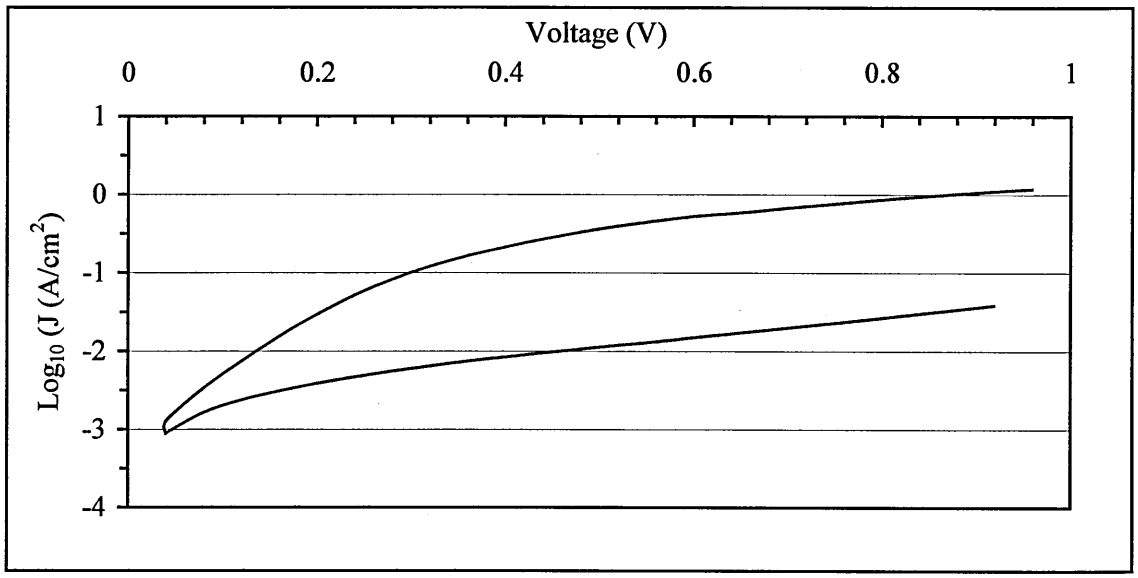

Figure 7.16: Semi-log J-V characteristics of glass/ITO/ZnSe/$CuInSe_2$/Au diode under dark conditions.

The ideality factor, n, was deduced from the $gradient = q/(2.303nkT)$ of the semi-log J-V curve displayed in Figure 7.16. A value of 2.1 was obtained, which shows that the current in the diode is dominated by recombination and generation processes.

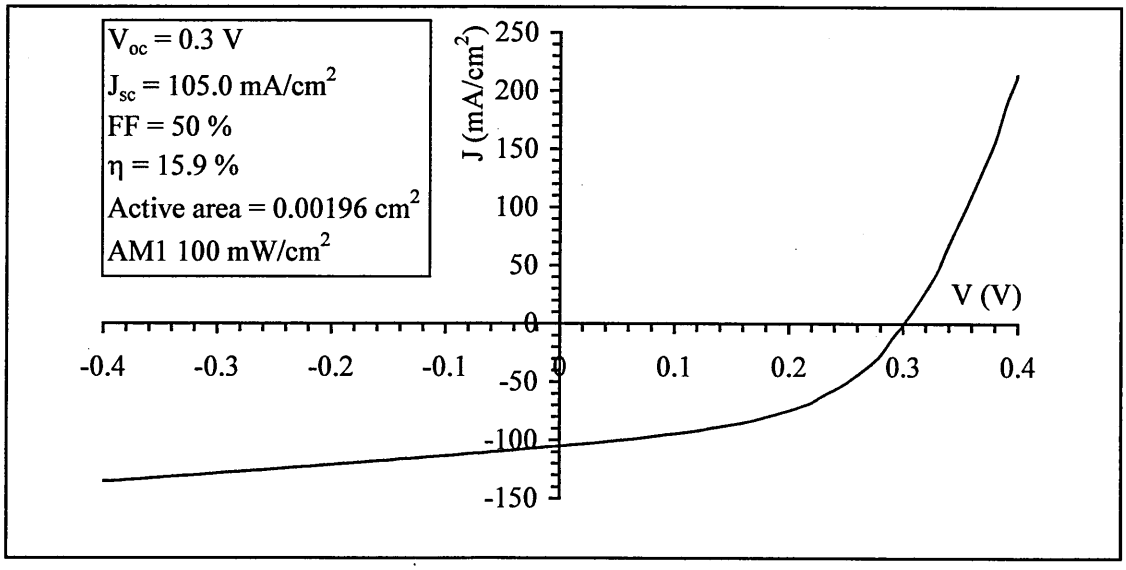

Figure 7.17: Linear J-V characteristics of glass/ITO/ZnSe/$CuInSe_2$/Au solar cell under illumination.

From the current-voltage characteristics of the device under illumination of 100 mW/cm displayed in Figure 7.17, one can see that this diode is photovoltaic active. It is noteworthy that the series resistance has slightly decreased with illuminating the device to a value of 0.41 Q/cm2. The three parameters generally used to assess the device performance were evaluated. It is found that the open circuit voltage and the fill factor have increased when compared to ZnSe-free cells but remain relatively low with values of 0.3 V and 50 %, respectively. The relatively small band gap of $CuInSe_2$ (1.04 eV) is responsible for the low open circuit voltage generally observed in solar cells made of this material [3]. Short circuit current has also drastically increased to a record value of 105.0 mA/cm2. Addition of more gallium into the electrodeposited $CuInSe_2$ material could be a method for improving the device performance. As a matter of fact, as indium is replaced by gallium, the band gap of the chalcopyrite compound is raised to a maximum value of 1.68 eV, which is the band gap of $CuGaSe_2$ [4]. The increase in the band gap of $Cu(InGa)Se_2$ alloy films will enhance the built-in potential of the device, and therefore improve the open circuit voltage. It can also provide a better match to the solar spectrum.

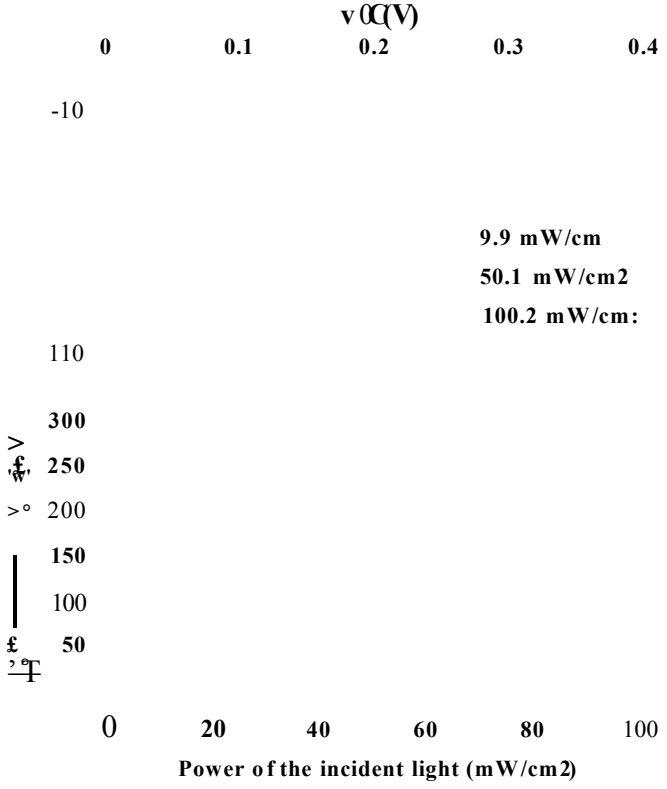

Figure 7.18: **Influence of the power of the incident light on the short circuit current and the open circuit voltage of a glass/FTO/ZnSe/Cu!nSe2/Au solar cell.**

The influence of the power of the incident light on the parameters of the device has also been investigated. One can see in Figure 7.18 that it affects considerably the device parameters. It is found that the short circuit current is proportional to the illumination intensity. On the other hand, the open circuit voltage increases sharply for low intensities and then saturates at higher intensities, as expected for normal solar cells.

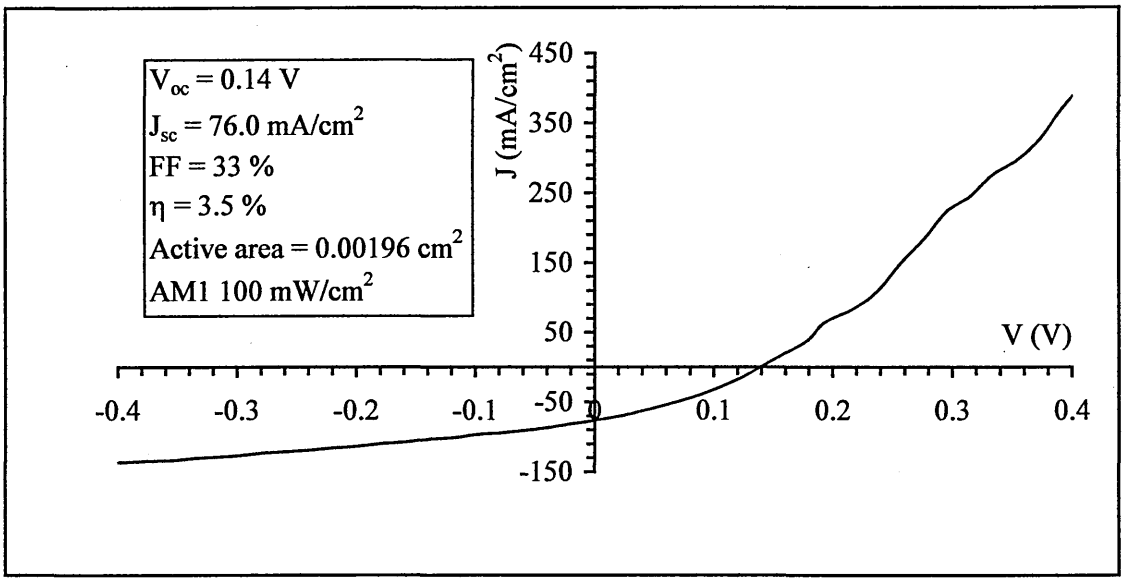

Figure 7.19: J-V characteristics of glass/FTO/ZnSe/$CuInSe_2$/Au solar cell under illumination showing the degradation of the device related to aging effect after 10-month storage under normal laboratory conditions.

Figure 7.19 displays the J-V characteristics of the glass/FTO/ZnSe/$CuInSe_2$/Au solar cell under illumination after 10-month storage under normal laboratory conditions. One can see that the device efficiency has degraded with time. Thus, all three parameters, the short circuit current, the open circuit voltage and the fill factor, have dropped to 76.0 mA/cm^2, 0.14 V and 33 %, respectively. This aging effect is mainly related to the inter-diffusion of atoms from different layers, which deteriorates the built-in potential energy at the interface.

In Figure 7.20 are shown the J-V characteristics of the best glass/FTO/ZnSe/$CuInSe_2$/Au solar cell achieved so far for larger dots of 2 mm diameter under illumination. One can see that the series resistance is higher than the one of smaller devices with a value of 4.46 Ω/cm^2. This increase of the series resistance with the size of the contact is probably due to the non-uniformity of the electrodeposited material forming the device and causes

a decrease of V_{OC} (0.135 V), J_{SC} (22.8 mA/cm^2) and FF (28 %), which lowers considerably the solar cell efficiency.

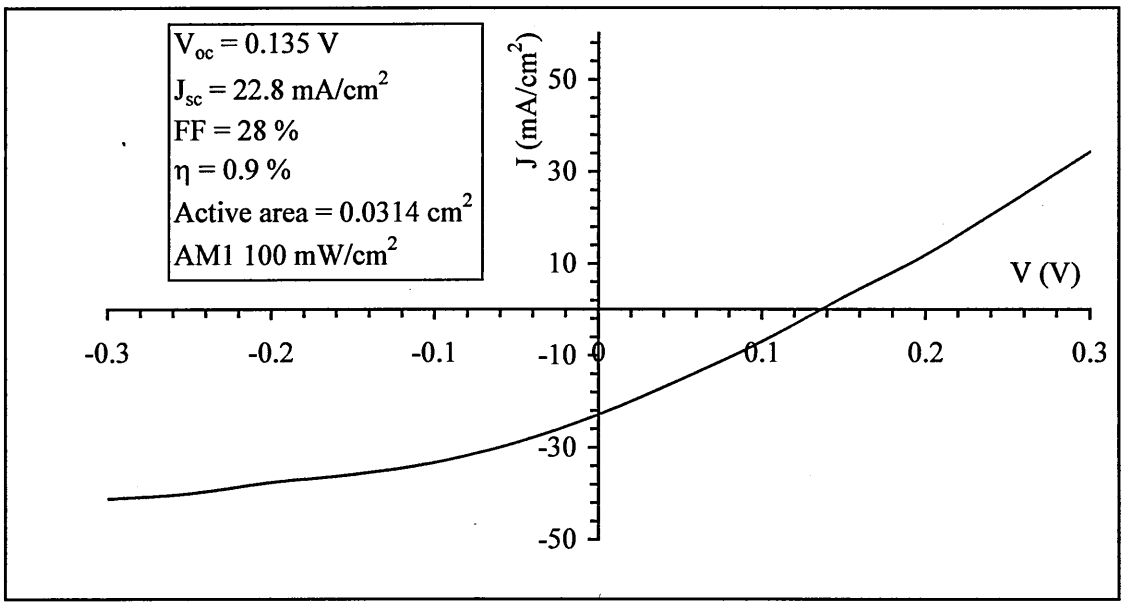

Figure 7.20: J-V characteristics of glass/FTO/ZnSe/$CuInSe_2$/Au solar cell under illumination for larger dots of 2 mm diameter.

7.4.3 I-V characteristics of glass/ITO/CdS/$CuInSe_2$/Au devices

Current-voltage characterisation was also carried out on glass/ITO/CdS/$CuInSe_2$/Au devices. The linear current-voltage characteristics under illumination for the best device achieved to date are shown in Figure 7.21.

One can first notice that the diode is photovoltaic active. However, no improvement has been observed compared to the glass/FTO/ZnSe/$CuInSe_2$/Au device. On the contrary, it was found that all the parameters used to evaluate the performance of the solar cells had slightly decreased to produce an efficiency of 10.1 %. It is noteworthy that the series resistance has slightly increased (0.48 Ω/cm^2) when compared to the series resistance of glass/FTO/ZnSe/$CuInSe_2$/Au device under illumination. The increase of the series resistance could be partly responsible for the lowering of the open circuit voltage and fill factor.

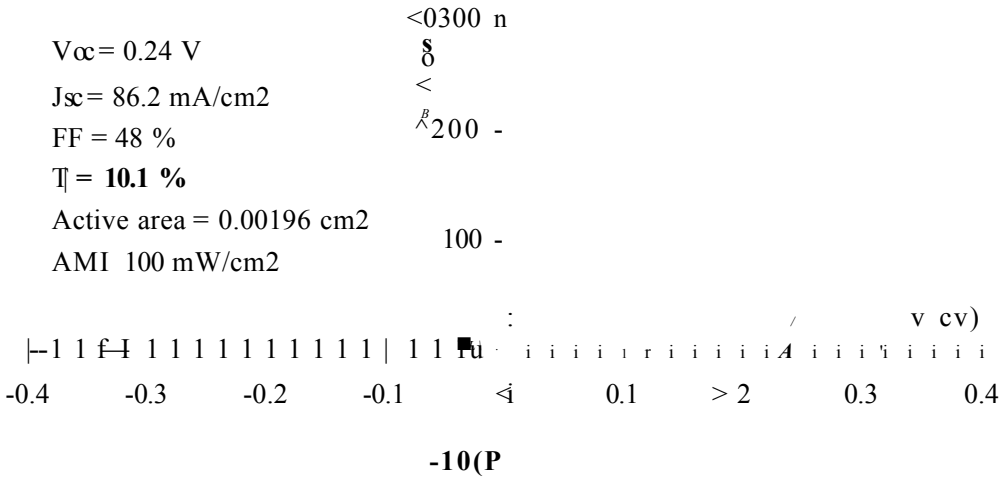

Figure 7.21: J-V characteristics of Glass/FTO/CdS/CuInSe2/Au solar cell under illumination.

7.5 Capacitance-voltage (C-V) analysis

Capacitance-voltage analysis was performed to measure the acceptor concentration, N_a, in electrodeposited $CuInSe_2$ materials and the barrier height ϕ_b resulting from the $CuInSe_2$/Au junctions.

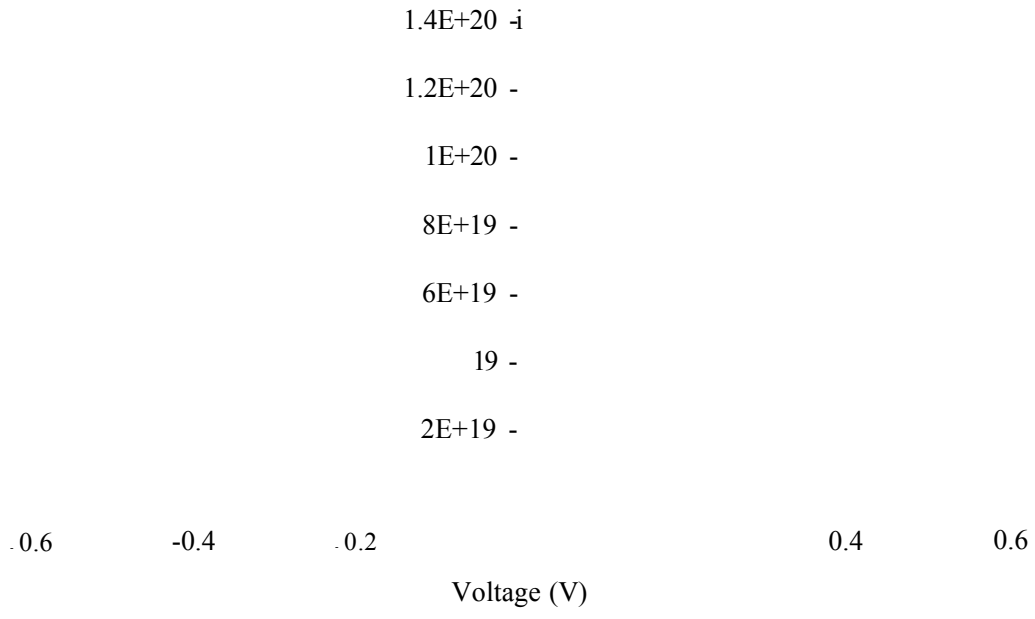

Figure 7.22: Capacitance-voltage characteristics of glass/ITO/CuInSe2/Au device.

Figure 7.22 shows the $1/C^2$ versus V plot of the best glass/ITO/$CuInSe_2$/Au rectifying diode fabricated to date. The curve is linear in the reverse bias voltage region indicating the uniformity of the free carrier concentration within the material. This result is surprising, as it is believed that the rectification comes from a buried n-p junction in the film. The non-uniform distribution of copper, indium and selenium shown by GDOES and XPS also predicted different results. The free carrier concentration and the barrier height can be deduced from the C-V characteristics using Equation (3.16), which can be rearranged to the form

$$\frac{1}{c^2} = \frac{2}{qN_a \varepsilon A^2}\left(V_b - V - \frac{kT}{q}\right)$$

The acceptor concentration N_a can, therefore, be provided from the *gradient* of the $1/C^2$ versus V plot, in the negative voltage region.

$$N_a = \frac{-2}{q \times gradient \times \varepsilon \times A^2}$$

where q is the electronic charge (q = 1.6021 x 10^{-19} C)

ε is the permittivity of $CuInSe_2$ at high frequencies (ε = 8.1 x 8.85 x 10^{-12} F/m)

A is the area of the device (A = 1.96 x 10^{-7} m^2)

gradient = -2 x 10^{20} F^{-2}/V

The built-in potential V_b can be provided from the intercept , I , of the straight line part of the $1/C^2$ versus V curve with the voltage axis:

$$V_b = I + \frac{kT}{q}$$

where k is the Boltzmann constant (k=1.38066 x 10^{-23} J/K)

T is the temperature (T=298 K)

I is the intercept (I = 0.12V).

The barrier height ϕ_b can be deduced from

$$\phi_b = V_b + \xi$$

where ξ is the voltage difference between the Fermi level and the valence band ($\xi = 0.1$ eV in this calculation).

Table 7.3 reports the acceptor concentration, N_a, the built-in potential, V_b, and the barrier height, ϕ_b, obtained from the C-V analysis.

N_a (cm^{-3})	V_b (eV)	ϕ_b (eV)
2.26×10^{18}	0.16	0.26

Table 7.3: Values of the free carrier concentration N_a, the built-in potential V_b and the barrier height ϕ_b obtained from C-V analysis.

The acceptor concentration, $N_a = 2.26 \times 10^{18}$ cm^{-3}, is representative of a heavily doped material, which can explain the small open circuit voltage of these devices. The reduction of the doping concentration to ~10^{15}-10^{16} cm^{-3} will drastically improve the device performance especially by increasing the V_{OC} value.

7.6 Summary and conclusions

The study of wet chemical etching by XPS has revealed that the surface composition of CIS films could change radically after etching.

Etchant	Remarks
H_2SO_4 & $K_2Cr_2O_7$	Depletion of Cu and In, oxide formation
HCl & HNO_3	Removal of $CuIn_3Se_5$ and native oxides, formation of elemental Se layer on the surface
NH_4OH	Removal of $CuIn_3Se_5$ and native oxides, formation of elemental Se layer on the surface
NaOH & H_2O_2	Strong reduction of Se, formation of metallic Cu and In layer, formation of CuO and SeO_2
NaOH & $Na_2S_2O_4$	Depletion of Se

Table 7.4: Summary of the effects of various etchants on electrodeposited CIS thin films.

It has also been found that each etchant reacted differently with the phases present on the surface. Table 7.3 gives a summary of the main results.

The early stage $CuInSe_2$-based solar cells showed encouraging results with efficiency up to 15.9 % for the best devices. The observed open circuit voltage, V_{OC}, short circuit current, J_{SC}, and fill factor, FF, for glass/FTO/ZnSe/$CuInSe_2$/Au devices are 0.3 V, 105.0 mA/cm^2 and 50 %, respectively.

The high solar cell efficiency seems mainly related to the quality of the CIS absorber layers, as window-free devices have also shown similar results. The low V_{OC} and FF could be increased by the addition of Ga into the electrodeposited $CuInSe_2$ films.

C-V measurements on a glass/ITO/$CuInSe_2$/Au structure were also carried out and an acceptor concentration of 2.26 x 10^{18} cm^{-3} was obtained, indicating a heavily doped material. A barrier height of 0.26 eV was also measured. Although this method of measuring barrier height is not very accurate due to the presence of defects in the depletion region, the low value of the barrier height is a strong indication of the observed heavy doping. The optimisation of the doping concentration to ~10^{15}-10^{16} cm^{-3} will produce a considerable enhanced solar cell device.

7.7 References

[1] Lide D. R., Handbook of Chemistry and Physics, 79th edition, CRC (1998-1999)

[2] Yakushev M. V., Constantinidis G., Imanieh M., Tomlinson R. D., Solid State Communications, 65 (1988) 1079

[3] Nakada T., Migita K., Niki S., Kunioka A., Japanese Journal of Applied Physics, 34 (Part 1) (No. 9A) (1995) 4715

[4] Moller H. J., Progress in Materials Science, 35 (1991) 205

Chapter 8: Conclusions and future work

8.1 Conclusions

Four main areas of work have been reported in this thesis.

First part includes the study of the substrates used to grow the semiconductor films as well as the growth and development of the window materials.
Attention was given mainly to the structural and morphological properties of the transparent conducting oxides (TCO). Both indium tin oxide (ITO) and fluorine tin oxide (FTO) substrates were used in this work because their different compositional and structural properties allowed a full characterisation of the deposited films. Both ITO and FTO films were found to be polycrystalline and showed void free surfaces with prominent spikes in nm scale.
During this project, n-type ZnSe and CdS films have successfully been grown on glass/TCO using the technique of electrodeposition. The ZnSe films were rather amorphous and the CdS films were polycrystalline. The material layers exhibited band gap values of 2.50 eV and 2.48 eV for ZnSe and CdS respectively. The study of the surface morphology revealed that the deposited layers of ZnSe and CdS were suitable for the achievement of high-efficiency heterojunction devices.

The second part contains the results of the characterisation of the benchmark $Cu(InGa)(SeS)_2$ material grown by the two-stage method at Showa Shell in Japan. The structural, morphological, compositional and electrical properties of the layers were investigated. The CIGSS films were found to be polycrystalline with the (112) preferential orientation of the chalcopyrite structure. The presence of various phases including $CuInSe_2$, $CuIn_3Se_5$, $CuInS_2$, $CuIn_5S_8$, Cu-Se and native oxides was observed.

The films appear dense and show crack-free surfaces with irregular-shaped grains electrically well connected to each other.
It has also been shown that XRF results on CIS-based materials were not reliable, as indium content is underestimated, and ICPMS should therefore be preferred for bulk analysis of Cu-In-Se materials.

In the next chapter, one has demonstrated that $CuInSe_2$ films could successfully be grown on glass/TCO by electrodeposition. The conditions of electrodeposition and post deposition treatments were found to influence strongly the structural, morphological, compositional and electrical properties of the films. Near-stoichiometric films grown by electrodeposition are polycrystalline with the (112) preferential orientation of the chalcopyrite structure.
The films appear dense with good mechanical adhesion to the substrate and show crack-free surfaces, as also observed for CIGSS grown by two-stage method. However, the surface of electrodeposited films is smoother and the grains are spherical and smaller. Cu, In and Se atoms are not uniformly distributed within the CIS films and In-rich phases, such as $CuIn_3Se_5$, cover the surface of the films. The layers are thought to be p-type but complementary experiments will have to be achieved to confirm the conductivity of the electrodeposited CIS material (see future work).

Final part of the thesis reports and discusses the results of electrodeposited $CuInSe_2$-based solar cells. A particular attention was given to the wet chemical etching procedure of the CIS layers and it was found that the surface composition could be adjusted by the use of appropriate etchants. Early stage $CuInSe_2$-based solar cells showed encouraging results with efficiencies up to 15.9 % for the best devices. The maximum values of the V_{OC}, J_{SC} and FF observed for the glass/FTO/ZnSe/$CuInSe_2$/Au devices were 0.3 V, 105.0 mA/cm^2, and 50 %, respectively. It will be discussed in the future work various routes to further improve these solar cells.

8.2 Future work

Solar cells based on $CuInSe_2$ grown by electrodeposition at Sheffield Hallam University have showed encouraging results with the best devices achieving efficiencies up to 15.9 % but a lot of work still has to be done to further develop the cells.

First, one will have to better understand the structure of the device, as the segregation of secondary phases, such as $CuIn_3Se_5$, could be responsible for the formation of p-n junctions within the CIS films. Thus, SIMS analysis could be performed in order to investigate the composition depth profile of the films and confirm the presence of secondary phases. Another interesting experiment will consist on determining the doping concentration as a function of depth using a Bio-Rad capacitance depth profiler in order to confirm the formation of p-n junctions within the films. By clarifying the structure of the devices, these experiments will help finding new ways to further improve the efficiency of the solar cell.

Deep level transient spectroscopy (DLTS) could also be used to evaluate the number of levels due to impurities or defects within the band gap of the CIS materials, as these levels usually have detrimental effects on electronic devices. In solar cell devices, they act as stepping-stones for recombination and generation processes and reduce the photo-current generated by photovoltaic activity.

At present, the efficiency of the electrodeposited CIS-based solar cells is limited by a low open circuit voltage (0.3 V). Addition of more gallium to $CuInSe_2$ could be used, as the relatively small band gap of $CuInSe_2$ (1.04 eV) is responsible for the low open circuit voltage. As indium is replaced by gallium, the band gap of the chalcopyrite compound is raised to a maximum value of 1.68 eV, which is the band gap of $CuGaSe_2$. The increased band gap of $CuIn_xGa_{1-x}Se_2$ alloy films will enhance the built-in potential in the devices, and therefore the open circuit voltage. It could also provide a better match to the solar spectrum. The substitution of $Ga_2(SO_4)_3$ by $GaCl_3$ in the electrodeposition bath could increase the deposition rate of Ga, as contrary to $Ga_2(SO_4)_3$, $GaCl_3$ easily dissolves in water and hence releases more Ga^{3+} ions. Another reason for the low open circuit voltage is the high doping concentration ($\sim 2 \times 10^{18}$ cm^{-3}) responsible for a thin depletion region and, as a result, tunnelling of free carriers through the barrier. The optimisation of the acceptor concentration to $\sim 10^{15}$-10^{16} cm^{-3} by doping or stoichiometric changes of the CIS materials will produce considerably enhanced solar cell devices.

It has been observed during this project that the samples electrodeposited from the same bath using similar conditions seemed to be different. It is not surprising, as the concentrations in the bath are very low and change with the deposition of the films. Some more experiments will therefore be needed to see how the bath age can influence the properties of the films (composition, morphology, crystallinity, electrical and optical properties) and the device performance.

During this project, attention was given to the etching procedure of CIS layers, as this information is very important in electronic device development process. Wet chemically etched surfaces using various etchants were examined using XPS in order to see the variations in the chemical nature and stoichiometry of the top layers. Regarding the results, HCl & HNO_3 seemed to give satisfactory results, as it did not change the stoichiometry of the films but removed the native oxides covering the CIS surface. This etchant could therefore be used in replacement of H_2SO_4 & $K_2Cr_2O_7$, which was employed throughout this work.

The best solar cells fabricated to date are very small devices (0.5 mm diameter) not suitable for commercialisation purposes. The development of larger devices is on early stage and one will have to improve the uniformity of the films to reproduce the performances of smaller devices. To achieve this target, one may have to use an anode of the same size of the substrate to have more uniform deposition of CIS on the total TCO plate area. The influence of the annealing process will also have to be studied more carefully. For instance, excessive heating and cooling gradients can be responsible for the failure of some devices. Annealing in air will also have to be deeply investigated, as it is reported to improve drastically the device efficiency.

List of publications

1. Development of solar cells based on $CuInSe_2$ grown by electrodeposition. I. M. Dharmadasa, T. Delsol, A. P. Samantilleke, J. Young. Patent to be submitted.

2. Electrodeposition of CdSe for applications in multi-layer thin film solar cells. I. M. Dharmadasa, A. P. Samantilleke, T. Delsol et al, final checking before submission to J. Electronics Materials November 2000.

3. All solid state, photo-electrochemical (PEC) solar cells with polyacrylonitrile (PAN) based solid polymer electrolyte and dye sensitized, nanoporous TiO_2 electrode. O. A. Ileperuma, S. Somasundaram, M. A. K. L. Dissanayake, R. Bokalawela, I. M. Dharmadasa, A. P. Samantilleke and T. Delsol. In preparation.

4. Investigation of n-type Cu_2O layers prepared by a low cost chemical method for use in photo-voltaic thin film solar cells. C. A. N. Fernando, P. H. C. de Silva, S. K. Wethasinha, I. M. Dharmadasa, T. Delsol and M. Simmonds. Submitted to "Renewable Energy", May 2001.

5. Systematic study of growth of $CuInSe_2$ using electrodeposition to develop thin film photo-voltaic devices. T. Delsol, I. M. Dharmadasa, A. P. Samantilleke, J. Young, J. K. D. S. Jayanettia and K. D. Jayasuriyab, Submitted to J. of Electronic Materials.